Title

Optical and Thermal Properties of Cool White Coatings based on Ceramic Hollow Microspheres

Author

Nie, Xiao

Publication Date

2022

UNIVERSITY OF CALIFORNIA,
IRVINE

Optical and Thermal Properties of Cool White Coatings based on Ceramic Hollow Microspheres

DISSERTATION

submitted in partial satisfaction of the requirements
for the degree of

DOCTOR OF PHILOSOPHY

in Mechanical and Aerospace Engineering

by

Xiao Nie

Dissertation Committee:
Associate Professor Jaeho Lee, Chair
Professor Jack Brouwer
Professor Yun Wang

2022

DEDICATION

To

my parents, lover, and friends

in recognition of their love and support

TABLE OF CONTENTS

LIST OF FIGURES

LIST OF TABLES

ACKNOWLEDGEMENTS

I would like to express my deepest appreciation to my committee chair, Professor Jaeho Lee for his full support and guidance during my graduate study. I learned from him how I should think and act like a professional scholar. He teaches me how to solve problems as a researcher and always encourages me to think about motivation before performing any experiments and to explore new ideas. He also encourages me to be the best PhD student and never settle for the ordinary level. He always encourages me to reach out to different groups or institutes for collaborations and attend different conferences for more experience. Without his support and guidance, this dissertation would not be possible.

I would also like to thank Professor Yun Wang and Professor Jack Brouwer for being the members on my Qualifying exam and dissertation defense committees. They provide many valuable comments and suggestions for my research. I would also like to express my appreciation to Professor Edwin A Peraza Hernandez and Professor Mohammad Javed Abdolhosseini Qomi for joining my Qualifying exam committee and their insightful comments and ideas to improve my research and myself as a researcher.

I would like to acknowledge the funding support from the National Science Foundation, the Henry Samueli School of Engineering and California Energy Commission. I cherish the time and collaborations with Dr. Youngjae Yoo at Korea Research Institute of Chemical Technology (now at Chung-Ang University) during his visit at UCI. I enjoy the valuable ideas, suggestions, and comments he gave to my research. I would like to thank Dr. Robert J. Flores at Advanced Power and Energy Program (APEP) for all the helpful suggestions and discussions during our collaborations. I also appreciate all the help and support I received from Dr. Dmitry Fishman in Laser Spectroscopy Lab at UCI and Dr. Qiyin Lin in Irvine Materials Research Institute at UCI

for their trainings and help in my research. They are always very patient with my questions and willing to share their thoughts and ideas with me.

I would like to express my thanks to my lab mates for their help and accompany. I thank Dr. Ziqi Yu and Dr. Zongqing Ren for their help and support to settle me down when I first came to Irvine. We had many great times together. I also thank Dr. Laia Ferrer Argemi, Dr. Shiva Farzinazar, and Jonathan Sullivan for the assistance, advice and comments in my research, and great times together during the group-outs. I would also like to thank Dr. Anirudh Krishna for his help in my research, and thank Hasitha Jeewana Hewakuruppu, Jiahui Cao, Charles Owens, Jungyun Lim and Jiajian Luo for their help and discussions in my research. I would also like to express my thanks to Hoyeon Park for his support, help and discussions when we work together on our projects. I will always cherish my friends at UCI for enriching my life and sharing their lovely life with me. We had many and many good times with fantastic food, video games and board games. They always give me much love and support and relax me a lot from my graduate study.

Last but not least, I will always be grateful to my girlfriend and my parents. My girlfriend always picks me up after school, keeps me up with my bad days, believes in me and makes sure the home is always tidy and clean. Her unconditional love and support shines my life brightly during my graduate study. For my parents, I owe so many thanks to them. They always believe in me, give me many helpful suggestions, encourage me to be better and share all the life with me even if we are far from each other. I dedicate this dissertation to them. I will love them forever.

VITA

Xiao Nie

2012-16	B.S. in Materials Science and Engineering, Shanghai Jiao Tong University
2016-18	M.S. in Materials Science, University of Southern California
2022	Ph.D. in Mechanical and Aerospace Engineering, University of California, Irvine

FIELD OF STUDY

Micro/nanoscale thermal transport, radiative cooling, thermal managements of buildings, hollow microspheres

PUBLICATIONS

Peer-reviewed Journals

J1. **Nie, X.**, Yoo, Y., Hewakuruppu, H., Sullivan, J., Krishna, A., & Lee, J. (2020). Cool white polymer coatings based on hollow glass microspheres for buildings. Scientific reports, 10(1), 1-10.

J2. **Nie, X.**, Yu, Z., Jackson, E., & Lee, J. (2021). Refractive index and extinction coefficient of hollow microspheres for solar reflection. Applied Physics Letters, 118(21), 211907.

J3. Krishna, A., **Nie, X.**, Warren, A. D., Llorente-Bousquets, J. E., Briscoe, A. D., & Lee, J. (2020). Infrared optical and thermal properties of microstructures in butterfly wings. Proceedings of the National Academy of Sciences, 117(3), 1566-1572.

J4. Yu, Z., **Nie, X.**, Yuksel, A., & Lee, J. (2020). Reflectivity of solid and hollow microsphere composites and the effects of uniform and varying diameters. Journal of Applied Physics, 128(5), 053103.

J5. Krishna, A., **Nie, X.**, Briscoe, A. D., & Lee, J. (2021). Air temperature drives the evolution of mid-infrared optical properties of butterfly wings. Scientific reports, 11(1), 1-10.

J6. Park, C., Park, C., **Nie, X**., Lee, J., Kim, Y. S., & Yoo, Y. (2022). Fully Organic and Flexible Biodegradable Emitter for Global Energy-Free Cooling Applications. ACS Sustainable Chemistry & Engineering.

Conference Proceedings

C1. **Nie, X.**, Krishna, A., Jeong, M., Wu, P., Yu, C., & Lee, J. (2019, May). Stretchable Selective Emitters based on Carbon Nanotube Films for Adaptive Thermal Control. In 2019 18th IEEE Intersociety Conference on Thermal and Thermomechanical Phenomena in Electronic Systems (ITherm) (pp. 204-208). IEEE.

ABSTRACT OF THE DISSERTATION

Optical and Thermal Properties of Cool White Coatings based on Ceramic Hollow Microspheres
by
Xiao Nie
Doctor of Philosophy in Mechanical and Aerospace Engineering
University of California, Irvine, 2022
Professor Jaeho Lee, Chair

Worldwide energy consumption associated with global warming, rapid urbanization, and heat island effect has surged in recent years, calling for building thermal management to provide energy savings and increase thermal comfort. Conventional air conditioning accounts for more than half of building energy, and alternative cooling technologies, including passive cooling, are needed. Development of advanced materials with engineered optical and thermal properties enables passive radiative cooling and significantly reduces the energy required to cool a surface. This doctoral research focuses on the use of ceramic hollow microspheres in radiative cooling devices and the study of their optical and thermal properties.

While solid and hollow microsphere composites have received significant attention as solar reflectors or selective emitters, the driving mechanisms and the fundamental determinants for their optical properties and material selection criteria are relatively unknown. In this dissertation, the solar reflectivity of solid and hollow microspheres with varying diameters are studied. Based on Mie theory and finite-difference time-domain (FDTD) simulations, hollow microspheres with a thinner shell are more effective in scattering the light compared to solid microspheres, leading to a higher solar reflectivity. The effects of refractive index and extinction coefficient values are

studied, and it explains how the high reflectivity of hollow microspheres is attributed to a combination of strong backscattering and limited absorption. Six ceramic materials with high refractive index and low extinction coefficient are studied using FDTD simulations and yttrium oxide (Y_2O_3) exhibits highest solar reflectivity among them.

The FDTD simulation results indicate hollow microspheres enable low-refractive-index materials such as silicon oxide (SiO_2) to achieve high solar reflectivity. SiO_2 has a low extinction coefficient in the solar region, which is beneficial for high reflectivity. In this dissertation, techno-economically viable and scalable white coatings are presented by integrating hollow glass microspheres into a polydimethylsiloxane (PDMS) binder. The main chemical composition of hollow glass microspheres in this study is SiO_2. The combination of high solar reflectivity from hollow glass microspheres and infrared emissivity of the binder material leads to a significant temperature reduction when coated on the surface of building materials. The white coating is shown to be superior to commercially available white paints and demonstrates considerable cooling energy savings on common commercial and residential building models. Although white coatings based on PDMS and hollow glass microspheres exhibit high solar reflectivity, the inherent absorption of PDMS as a binder material limits its reflectivity to the visible wavelengths and is not effective in the near-infrared wavelength region. To improve near-infrared reflection, hollow glass microspheres are integrated within potassium bromide (KBr), which inherently has a lower near-infrared absorption compared to PDMS. The use of KBr binder material and spray coating method makes the white coating more scalable and improves solar reflectivity while maintaining a high infrared emissivity. The coating can be further improved by utilizing a different hollow microsphere material. Numerical simulation results demonstrate that Y_2O_3 hollow microspheres are promising to achieve near-unity solar reflectivity with low thicknesses and are shown to

outperform hollow glass microspheres. Therefore, white coatings using Y_2O_3 hollow microspheres are prepared. The thermal analysis shows white coatings provide a surface temperature reduction up to 8°C lower than ambient air and a cooling power of 111 W/m^2, assuming a constant ambient temperature of 27°C and a solar intensity of 1000 W/m^2. The ultrahigh solar reflectivity of white coatings exceeds most of the reported values of pigment/polymer composite systems without expensive metallic reflectors. Y_2O_3 hollow microspheres provide a promising solution for cooling applications requiring near-unity solar reflectivity.

Although white coatings have been demonstrated as promising materials for radiative cooling, energy and cost savings of white coating in buildings have not been fully evaluated. In this dissertation, the energy and cost savings are analyzed for ideal white coatings, with unity solar reflectivity and infrared emissivity, and polymer coatings based on hollow glass microspheres and PDMS binder material, with a solar reflectivity of 0.92 and an infrared emissivity of 0.9, for midrise apartment models in various climate zones across the United States. Ideal white coatings and polymer coatings achieve annual cooling energy savings of 0.7-6.6 kWh/m^2 and 0.6-5.8 kWh/m^2, respectively, in various climate zones for midrise apartments. Both the positive and negative effects of white coatings are summarized including cooling energy savings, cooling peak load reduction, heating energy increase, carbon emission savings, utility cost savings, and thermal comfort benefits in buildings. Additionally, the statistical relationships between critical performance metrics and general weather and location parameters are examined using the analysis of variables (ANOVA) coupled with linear regression. The findings in this dissertation will guide the material selection for ultrahigh solar reflectivity and fabrication of future white coatings for thermal management.

Chapter 1 Introduction

1.1 Development of Radiative Cooling

1.1.1 Introduction

Global warming and climate change increases the ambient temperature and brings extreme heat events more frequently and more severely[1]. Higher ambient temperature, along with the poor design of buildings, significantly increases indoor temperatures, which has an important impact on thermal comfort, human health, energy consumption, peak electricity demand, and global economy[2]. Usually, air conditioning is used to cool indoor space and avoid overheating in the buildings. In some countries, building sectors accounts for more than one-third of total energy consumption[3] and 1.24 PWh per year is used for cooling purpose[4], which is about 3.9% of the total energy consumption[4]. Future energy consumption forecast indicates that cooling will be the dominant energy use beyond 2050, which corresponds to an average increase close to 260% compared to the current consumption[5].

Conventional air conditioning technologies are associated with severe energy, environmental, social, and economical problems. Resolving the interconnected energy, greenhouse gas emission, air quality, and human health problems will require alternative innovative cooling technologies for buildings and outdoor spaces. Cooling technologies can be classified as passive and active, and many of them are based on newly developed advanced materials exhibiting superior thermal and optical materials. Active cooling materials including thermoelectric, electrocaloric, magnetocaloric, and electrocaloric devices have attracted a very high interest while prototype heat pumps of high efficiency are already developed[6]. Passive cooling materials for buildings and outdoor spaces including infrared reflecting materials, fluorescent surfaces, thermochromic materials, and photonic and plasmonic selective emitters, seems to be the most advanced ones presenting high cooling potentials.

Passive radiative cooling is a very well-known cooling technique as it was used back to the ancient times to produce ice and cool spaces. It is based on the potential of terrestrial surfaces to dissipate heat to the cold outer space at 3K[7,8]. While the incoming solar irradiation within the wavelength region of 0.3-2.5 um heats up the surface, radiation from the object to the cold outer space through the atmosphere's transmission window[9] in the middle-infrared wavelength region of 8-13 um helps to cool the surface. Ones the radiative balance of the surface is negative, its temperature may be substantially lower than the ambient temperature if the convective gains are limited. Cool surfaces can be thus used for surface cooling in buildings.

Initially, radiative cooling materials including selective surfaces, reflective covers, and thin films were developed to present a substantial high reflectivity in the solar region and a high emissivity in the infrared region. Although during the nighttime almost all materials succeed to exhibit a significant cooling potential, their cooling capability in the daytime is almost negligible as their surface temperature fails to become lower than ambient temperature. The development of daytime sub-ambient radiative cooling is the ultimate goal since buildings require significant cooling during the peak solar intensity in the daytime.

1.1.2 Fundamentals of Radiative Cooling

A radiative cooler is considered at an area A with some certain temperature T, whose spectral and angular emissivity is ε (λ, θ). When it is exposed to steady daytime ambient environment, it is subject to both solar irradiation and atmospheric thermal radiation. Assuming the ambient temperature is T_{amb}, the net cooling power of the radiative cooler at temperature T is expressed as:

$$P_{cooling}(T) = P_{rad}(T) - P_{sun} - P_{atm}(T_{atm}) - P_{con} \tag{1.1}$$

In the right-hand side of equation (1.1), the first term $P_{rad}(T)$ is the power radiated by the radiative cooler:

$$P_{rad}(T) = A \int d\Omega cos\theta \int_0^{\infty} d\lambda I_{BB}(T,\lambda)\varepsilon(\lambda,\theta) \tag{1.2}$$

In the equation, $\int d\Omega = 2\pi \int_0^{\pi/2} d\theta sin\theta$ is the angular integral over a hemisphere and $I_{BB}(T,\lambda) = \frac{2hc^2}{\lambda^5} \cdot \frac{1}{e^{hc/(\lambda k_B T)}-1}$ is the spectral radiance of a perfect blackbody at the temperature T. Here, h is the Planck's constant, c is the speed of light and k_B is the Boltzmann constant.

The second term $P_{atm}(T_{atm})$ presents the incident solar power absorbed by the radiative cooler and the solar illumination is given by $I_{AM1.5}(\lambda)$, the AM 1.5 spectrum.

$$P_{sun} = A \int_0^{\infty} d\lambda \varepsilon(\lambda,\theta) I_{AM1.5}(\lambda) \tag{1.3}$$

The third term $P_{atm}(T_{atm})$ and the fourth term P_{con} in equation (1.1) is the incident atmospheric thermal radiation power and the power loss due to the conduction and convection, respectively:

$$P_{atm} = A \int d\Omega cos\theta \int_0^{\infty} d\lambda I_{BB}(T,\lambda)\varepsilon(\lambda,\theta)\varepsilon_{atm}(\lambda,\theta) \tag{1.4}$$

$$P_{con} = Ah_c(T_{atm} - T) \tag{1.5}$$

Here $h_c = h_{cond} + h_{conv}$ represents the sum of the non-radiative heat transfer coefficient capturing conductive and convective heating because of the contact of the radiative cooler with external surfaces and ambient air adjacent to the film.

Equation (1.1) in general relates the cooling power $P_{cooling}$ (T) of the surface, that is, the net outgoing power from the surface, as a function of its temperature T. If the net power outflow is positive when $T=T_{amb}$, which also means that it radiates more heat out to space than it gains by absorbing sunlight and atmospheric thermal radiation, the surface becomes a radiative cooling device. The power outflow $P_{cooling}$ ($T=T_{amb}$) then defines its cooling power at ambient air temperature. In the absence of net outflow, a radiative cooler's temperature should reach a steady-state temperature below ambient. The solution of equation (1.1) with $P_{cooling}$ (T) = 0 defines the steady-state temperature T_{sur}.

1.2 Radiative Cooling Materials

Ideal materials for radiative cooling should exhibit: (1) Unity reflectivity in the solar wavelength region (0.25-4 μm, with the majority of the solar power available between 0.3 and 2.5 μm); (2) Unity emissivity in the atmospheric transmission window (8-13 μm) and zero emissivity in the rest of the thermal wavelength region (4-80 μm). Past radiative cooling study focuses on natural or simply synthesized composite materials including commercially available polymers, metals, gases to form a radiative cooler whose optical properties could not be precisely controlled. Therefore, the cooling performance is not usually good enough to achieve sub-ambient cooling during daytime periods. Most of the proposed structures or systems can only demonstrate sub-ambient cooling results during the nighttime periods.

1.2.1 Conventional Radiative Cooling Materials

In 1978, Harrison and Walton[10] achieved a 2°C sub-ambient surface temperature at noon under direct sunlight by applying commercially available Titanium Oxide (TiO_2)-based white paints onto an aluminum substrate. Orel et al.[11] found that the performance of TiO_2 can be slightly improved when adding barium sulphate ($BaSO_4$) into TiO_2. Polyvinyl-fluoride (PVF)[12] was also demonstrated for radiative cooling applications due to its high absorption in the atmospheric window. SiO films on aluminum substrate[13,14] has also been studied to exhibit high emittance in the atmospheric transmission window, both computationally[13] and experimentally[14]. The optical property of silicon nitride thin films for radiative cooling were also studied by Eriksson et al.[15].

1.2.2 Daytime Radiative Cooling Technologies and Progress

Conventional radiative cooling materials failed to present a very high reflectivity in the solar wavelength region together with a high emissivity in the atmospheric transmission window. As a result, these materials cannot provide sufficient cooling performance under direct sunlight during the daytime. A successful daytime cooling requires a solar reflectivity higher than 0.9 and an infrared emissivity larger than 0.9[16]. Recent advances in the design of optical nanostructures and the significant progress in nanofabrication technologies provide great opportunity to create or modify the structure of materials in nanoscale and precisely control their optical and thermal properties. In the following, recent developments on daytime radiative cooling materials will be discussed and summarized.

1.2.2.1 Multilayer Photonic Structures

Multilayer photonic structures are composed of two main parts aiming to either increase the solar reflectivity or to enhance the infrared absorptance in the atmospheric window.

To increase the solar reflectivity in the multilayer structure, one common method is to use Aluminum (Al) or Silver (Ag)[17–19] which exhibit a high reflectivity in the solar region or use alternate layers of high and low refractive index materials. Sometimes an Al or Ag mirror is used on the bottom of alternate high-low refractive index materials. For instance, Raman et al.[16] reported alternate layers of HfO_2 and SiO_2 on top of an Ag thin film and demonstrate a high solar reflectivity of 0.96. In another work, HfO_2 is replaced with TiO_2 to achieve similar high solar reflectivity. Materials[16,20] like TiO_2, SiO_2, SiC, MgF_2, Al_2O_3 are usually used for alternate layers, both experimentally and computationally.

To enhance the absorptivity in the atmospheric transmission window in the infrared region, multilayer films composed of various materials are used to exhibit phonon-polariton excitation. The resulting spectral emissivity depends mainly on the number of layers and the specific wavelengths that the material resonates. Bao et al.[21] reported a single layer of SiO_2-nanoparticle layer and the calculated emissivity is close to 0.9. Kou et al.[17] proposed a 500-nm-thick fused SiO_2 wafer layer coated on top with a 100-um-thick PDMS, which shows a high emissivity lager than 0.9 in the atmospheric window. Alternating layers of SiO_2 and HfO_2[16]; layers of SiO_2 and BN; layers of Si and Si_3N_4; alternating layers of TiO_2, SiO_2, and Al_2O_3; layers of VO_2, MgF_2, and W; and layers of HfO_2, BN, SiC, and SiO_2 were reported to exhibit high emissivity in the infrared region especially in the atmospheric window as well.

The radiative cooling performance of multi-layer structures during the daytime has been fully evaluated experimentally[16–18,20,22–24] and through simulations. The surface temperature and the cooling power of such structures is related not only to the optical properties of materials, the atmospheric radiation, and the convection-conduction heat gains/losses of the surface. Chen et al.[25] utilized a vacuum chamber to host the radiative cooler to minimize the convection losses and experimentally showed that the daytime surface temperature of the cooler is reduced to 42°C below the ambient temperature while during the whole daytime it was kept up to 33°C lower than the ambient temperature. In ambient conditions, the radiative cooler is also reported to exhibit daytime surface temperature below ambient temperature. The temperature reduction and cooling power is varied with different locations, testing conditions and ambient environments. For instance, Raman et al.[16] reported a daytime surface temperature 5°C lower than the ambient temperature while the cooler presented a net cooling power of 40 W/m^2. Given the large diversity between the testing conditions and the simulation assumptions, it is hard to compare the performance reported previously.

1.2.2.2 Polymers for Radiative Cooling

Radiative coolers with polymers is also an attractive solution for daytime radiative cooling due to its low-cost and simple fabrication. In general, polymers are doped with nanomaterials-resonators[18] which shows high emissivity in the atmospheric transmission window wavelengths where nanoparticles resonate. Huang et al.[26] mixed carbon black particles in an acrylic resin to enhance the infrared emissivity and the average emissivity in the atmospheric window is around 0.9. Zhai et al.[18] reported a transparent polymer with SiO_2 microspheres randomly distributed inside and backed with a reflective Ag layer. The polymer with 6% of microspheres exhibits high infrared emissivity of 0.93 due to the phonon enhanced resonance of the microspheres. The backed Ag layer provides the high reflectivity of 0.96 so that the net cooling power of the material is reported to be 93 W/m^2 during the daytime. Kou et al.[17] used a thin layer of PDMS to enhance the infrared emissivity due to strong absorption of the polymer. Many polymer-based radiators use metallic layers to provide high reflectivity in the solar region, like Al or Ag, with a reflectivity higher than 0.92. Experimental and theoretical investigations reveal that the cooling power of such polymer based radiators varies between 93 W/m^2 to around 100 W/m^2.

Mandal et al.[23] developed a hierarchically porous poly(vinylidene fluoride-cohexafluoroproprene) (P(VDF-HFP)HP) coating in the format of a paint and can be applied in building structures. Its solar reflectance is close to 0.96 with a small thickness of 300 μm while its emissivity in the infrared region is 0.97. The high solar reflectivity and infrared emissivity is due to the micro- and nano-pores in the coating that backscatter sunlight and enhance thermal emittance. Daytime temperature measurement shows that its surface temperature is 6°C lower than the ambient temperature and the net cooling power is close to 96 W/m^2.

1.2.2.3 Pigments-Embedded Composite Systems

Passive cooling materials under the form of paints, do not use expensive metallic materials or complicated nanostructure fabrication techniques and rely on simple and low-cost fabrication methods, which make them attractive in the field. For such materials, nanoparticles, or microspheres, are usually embedded in organic or inorganic binder matrix. For example, a random photonic media composed of SiO_2 microspheres is reported by Atiganyanun et al.[27] to show high reflectivity in the solar region and high emissivity in the infrared region. It is calculated that a media composed of 2-μm-diameter SiO_2 microspheres with a filling factor of 0.6 and a thickness of 500 μm presents a solar absorptivity less than 0.03 and a high emissivity in the atmospheric transmission window higher than 0.95. The radiative cooler with a thickness of 700 μm thickness and 2-μm-diameter SiO_2 microspheres deposited on a glass slide is experimentally tested. During the daytime, the cooler presents a temperature almost 12°C lower than the ambient temperature while the nighttime temperature is around 4°C lower than the ambient.

Recently many composite systems using TiO_2 nanoparticles[28], hollow glass microspheres[29], $CaCO_3$ nanoparticles[30], $BaSO_4$ nanoparticles[24], and hexagonal boron nitride (BN)[31] were developed to exhibit high solar reflectivity and infrared emissivity for radiative cooling applications. People et al.[28] demonstrate broadband enhanced solar reflectivity by tuning the size composition of low-concentration TiO_2 nanoparticles of 104±37 nm. Li et al.[24,30] developed white coatings with high solar reflectivity using $CaCO_3$ or $BaSO_4$ nanoparticles with acrylic binder. The development of such white coatings presents ultrahigh solar reflectivity without any metallic reflectors and provide an inexpensive solution to surface cooling applications.

1.3 Outline of Doctoral Research

This doctoral research will talk about the use of hollow microspheres, including hollow glass microspheres and Y_2O_3 hollow microspheres, in white coatings for surface cooling applications in buildings. Chapter 2 presents the effects of sizes, shell thicknesses, refractive index, and extinction coefficient values in hollow microspheres on solar reflectivity in composite systems by using 2D FDTD simulations. This chapter also identifies several ceramic materials to be promising materials to achieve high solar reflectivity. Chapter 3 discusses the polymer coating based on hollow glass microspheres and PDMS with high solar reflectivity and infrared emissivity, leading to significant temperature reduction and energy savings in buildings. Chapter 4 compares organic binders such as PDMS and solar transparent binder such as potassium bromide in white coatings and demonstrates that solar transparent binders lead to larger solar reflectivity due to its high solar transparency in the near-infrared region. Chapter 5 shows the experimental fabrication of Y_2O_3 hollow microspheres and its ultrahigh solar reflectivity when integrated with solar transparent binders. Chapter 6 demonstrates the energy and cost savings analysis of ideal white coatings with unity solar reflectivity and infrared emissivity for prototype midrise apartment building model in different cities across the US. The impact of white coatings on energy savings, carbon emission savings, utility cost savings, and cooling degree days reduction in buildings is discussed in this chapter. Chapter 7 concludes the use of hollow microspheres in radiative cooling applications in buildings and discusses the opportunities for future research.

Chapter 2 Effects of Sizes, Shell Thicknesses, Refractive Index and Extinction Coefficient in Hollow Microspheres for Solar Reflection

While solid and hollow microsphere composites have received significant attention as solar reflectors or selective emitters, the driving mechanisms and the fundamental determinants for their optical properties and material selection criteria are relatively unknown. In this dissertation, we study the solar reflectivity of solid and hollow microspheres with varying diameters. Based on Mie theory and finite-difference time-domain simulations, our analysis shows that hollow microspheres with a thinner shell are more effective in scattering the light compared to solid microspheres and lead to a higher solar reflectivity. We also show the effects of refractive index and extinction coefficient values and explain how the reflectivity of hollow microspheres is attributed to a combination of strong backscattering and limited absorption. Our analysis indicates several ceramic materials with high refractive index and low extinction coefficient values are promising candidates to achieve a high solar reflectivity.

2.1 Introduction

Passive radiative cooling using outer space as the heat sink has revolutionized the thermal management of buildings[18,23], human body[32,33], and deep space applications[34]. Optical coatings that reflect sunlight in the wavelengths of 0.2-2.4 μm, which cover the ultraviolet, visible, and near-infrared regions, may lead to significant surface cooling and energy savings for buildings[29,35,36], spacecraft thermal control on extreme environments[34,37], and efficient heliostats for concentrating solar power plants[38,39].

Over the past decades, several experimental and numerical demonstrations of perfect reflection have been reported using all-dielectric metamaterials[40–42]. However, narrow bandwidth limits its application in shielding high-power irradiation such as solar irradiation. Metallic reflectors[17,37] and distributed Bragg reflectors[7,8,16] are commonly used to achieve broadband high solar reflectivity. However, metallic reflectors cannot provide high solar reflectivity in the wavelength region of 0.3-0.5 µm, and Bragg reflectors composed of alternating layers are typically made by sophisticated fabrication techniques, which require either many layers or expensive metallic films to achieve the desired reflectivity.

Another inexpensive and scalable solution for achieving broadband near-perfect solar reflectivity is to fabricate dielectric nanoparticle-polymer composites[19,23,29,43] with or without metallic reflectors, using hierarchical porous polymer[23] or hollow microspheres[29,44–46]. Hollow microspheres made of dielectric materials[29,44,46] or polymers[45] are studied to exhibit broadband high solar reflectivity. For instance, our previous work[29,46] shows that hollow microsphere designs enable low-refractive-index materials such as SiO_2 to have higher backscattering intensity compared to solid microspheres and thus show high solar reflectivity.

In addition to novel solar reflector discovery, analytical and numerical studies[28,46] based on Mie theory, Monte Carlo method and finite-difference time-domain (FDTD) method have been performed to investigate mechanism for high solar reflectivity. A noteworthy hierarchical cooling film developed by Peoples et al[28] lately demonstrated broadband enhanced solar reflectivity by tunning the size composition of low-concentration TiO_2 nanoparticles of 104±37 nm. The efficacy of size hierarchy was supported by Monte Carlo and Mie theory calculations assuming individual scattering. The composite with the optimized particle size constitution yields reflectivity higher than that of each building block, yet precise control on the particle size could be practically challenging. Despite these efforts, little attention has been paid to material selection principles for solar reflectivity enhancement. In this work, we performed systematic investigation on composite systems using randomly closed-packed hollow glass (SiO_2) microspheres with uniform and varying diameters ranging in 0.125-8 μm using the Mie theory and finite-difference time-domain (FDTD) calculations. By conducting single-particle Mie theory calculation, we identify geometric parameters that drive high reflectivity. By performing 2D FDTD simulations, which are valid and more computationally affordable[47] than previous approaches[48,49], we investigate the effect of the shell thickness and material. We separately investigate the effects of refractive index and extinction coefficient in hollow microsphere on weighted solar reflectivity in the solar wavelength region of 0.2-2.4 μm. We also identify several materials that lead to broadband ultrahigh solar reflectivity with a small thickness. These findings could help to benefit solar reflector designs.

2.2 Effects of Sizes and Shell Thicknesses

We first compute the scattering efficiency $\boldsymbol{Q_{scat}}$ of single hollow microsphere in PDMS based on Mie theory (See Approach and Methods Section). We choose the outer diameter $\boldsymbol{d_o}$ of hollow microspheres from 0.5 to 8 μm. For each $\boldsymbol{d_o}$, we let the diameter, $\boldsymbol{d_i}$, of the air core, to increase from 0 to $\boldsymbol{d_o}$, where $\boldsymbol{d_i}$ of 0 and $\boldsymbol{d_o}$ are solid microsphere and porous PDMS, respectively. In **Fig. 2.1a**, we plot $\boldsymbol{Q_{scat}}$ as colormaps to visualize its dependences on $\boldsymbol{d_i} / \boldsymbol{d_o}$ and the wavelength (λ) (0.4-2.4 μm). We can make two key observations. First, by increasing the volume of the air, or decreasing shell thickness $\boldsymbol{t} = (\boldsymbol{d_o} - \boldsymbol{d_i}) / 2$, a hotspot representing high scattering efficiency appears for all $\boldsymbol{d_o}$ simulated. Second, the location of the high $\boldsymbol{Q_{scat}}$ on the spectrum redshifts as we increase $\boldsymbol{d_o}$. These results show the advantage of employing hollow structures that have a larger interface density. We define the interface density as $\varrho_{int} = \frac{\sum_N 4\pi r_N^2}{4/_3 \pi \max\limits_N (r_N^3)}$, where $\boldsymbol{r}$ is the radius associated with each interface and $\boldsymbol{N}$ is the number of interfaces. Thus, for instance, a hollow microsphere with $\boldsymbol{d_i}/\boldsymbol{d_o} = 0.9$ and $\boldsymbol{d_o} = 1$ μm has an interface density of 10.86 μm^{-1} and a solid microsphere with

d_o = 1 μm has an interface density of 6 μm^{-1}. Due to light scattering at the interface with refractive-index contrast, the hollow microspheres with greater interface densities leads to higher scattering efficiency and hence higher solar reflectivity. In **Fig. 2.1b**, we set **d_i** / **d_o** to be 0.9 and plot the wavelength-dependent **Q_{scat}** curves. We can more clearly visualize the redshift of the **Q_{scat}** peak for the **d_o** chosen. By increasing **d_o** from 1 μm to 5 μm, the peak of **Q_{scat}** shifts from approximately 0.5 to 2.4 μm on the spectrum; further increasing or decreasing **d_o** to 8 or 0.5 μm shift the peaks out of **λ** = 0.4 to 2.4 μm.

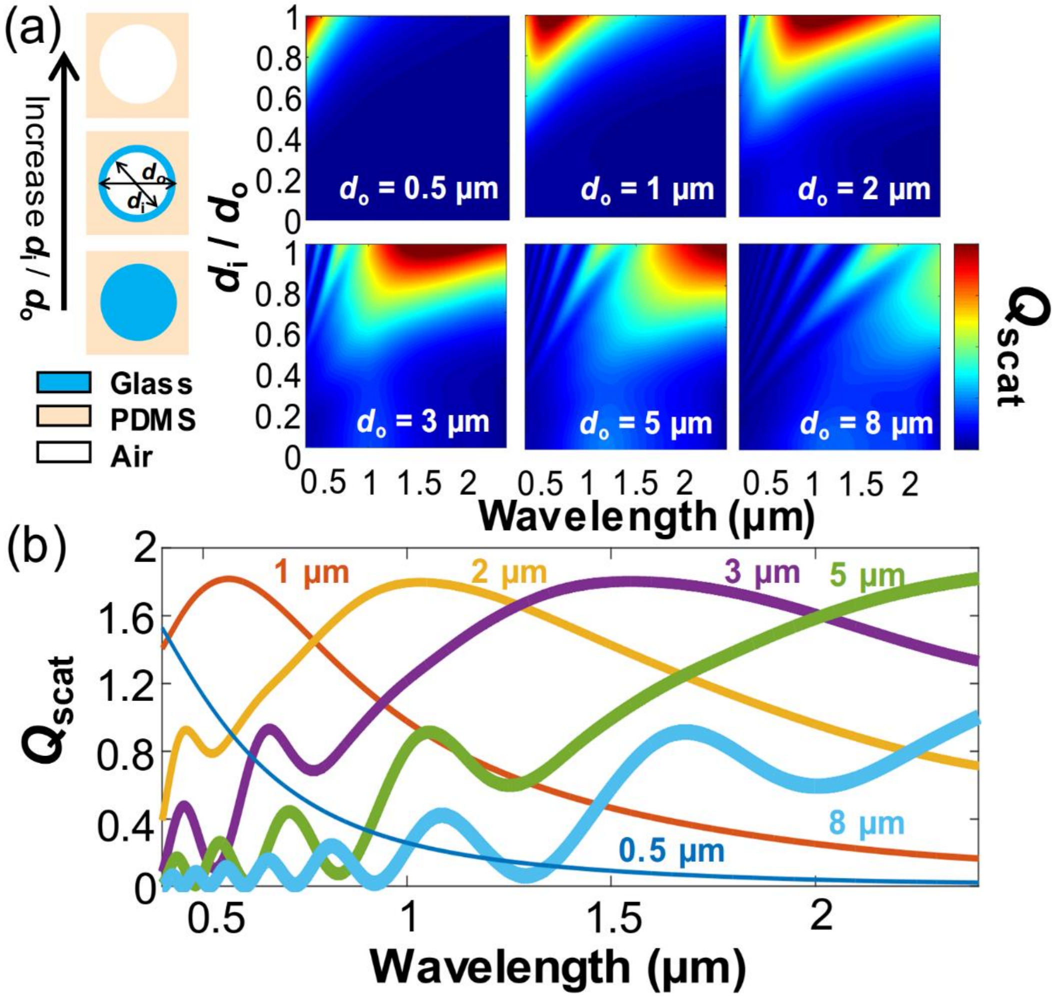

Figure 2.1 The scattering efficiency of hollow glass microspheres. (a) The scattering efficiency (**Q_{scat}**) calculated using the Mie theory for individual hollow SiO_2 microspheres in PDMS background in the

wavelength of 0.4-2.4 μm. The outer diameters $\boldsymbol{d_o}$ are varied from 0.5 to 8 μm, over which the scattering efficiency peaks redshift over the wavelength of interest. The shell thickness is indicated by the diameter ratio $\boldsymbol{d_i / d_o}$, which corresponds to the diameter of air core and SiO_2 microsphere, respectively. By changing from solid SiO_2 microsphere to porous PDMS, the scattering efficiency increases. (b) $\boldsymbol{Q_{scat}}$ as a function of wavelength for $\boldsymbol{d_i / d_o} = 0.9$. The diameter $\boldsymbol{d_o}$ is color-labeled correspondingly. The scattering efficiency shows peak with location and width corresponding to $\boldsymbol{d_o}$. For $\boldsymbol{d_o} = 0.5$ and 8 μm, the scattering efficiency does not show the peak in the wavelength from 0.4 to 2.4 μm.

We compute the spectral-average solar reflectivity $\langle \boldsymbol{R} \rangle_\lambda = \frac{\int \boldsymbol{R(\lambda) d\lambda}}{\int \boldsymbol{d\lambda}}$ to compare composites with varying geometrical parameters. 2D FDTD simulations are performed in a 20 μm × 100 μm unit cell (Fig.S3(c)) periodically repeated in $\boldsymbol{x}$ with perfectly matched layers (PML) in $\boldsymbol{y}$. Using wider unit cell or finer mesh change results insignificantly. As the shell thickness and number of interfaces remain the same for 2D and 3D simulations. Our 2D model can capture the light transport and field information in the *x-y* plane, which is a cross-section of the 3D hollow microsphere. Similar treatment using 2D FDTD models have been employed for 3D nanostructures including retinas[50], nanodots[23], and nanoparticles[51]. We illuminate the unit cell with a broadband (0.4-2.4 μm) unpolarized plane wave from below. Hollow microspheres are randomly generated in the unit cell at the filling fraction (f.f.) of 55 vol%, which approaches the packing density of typical self-assembly structures[52]. The refractive indices of PDMS, SiO_2 and TiO_2 are from previous work[53,54]. To investigate the effect of shell thickness, we fix $\boldsymbol{d_o}$ of hollow SiO_2 microspheres to 1 μm. In **Fig. 2.2a**, $\langle \boldsymbol{R} \rangle_\lambda$ increases from 0.04 to 0.77 by changing $\boldsymbol{d_i} / \boldsymbol{d_o}$ from 0 to 1. When $\boldsymbol{d_i} / \boldsymbol{d_o} = 0.9$, $\langle \boldsymbol{R} \rangle_\lambda$ peaks at 0.77, which outperforms that of solid microspheres and the porous PDMS. This could imply a significant reduction of coating thickness offered using hollow microsphere structure. From the point of view of refractive-index-contrast, $\langle \boldsymbol{R} \rangle_\lambda$ depends strongly on the air (n_{glass} - n_{air} is the largest contrast in this system) core size, $\boldsymbol{d}_{\mathbf{i}}$, where larger $\boldsymbol{d}_{\mathbf{i}}$ offers greater interface-to-volume ratio and thus enhanced scattering efficiency. The propagation of light is randomized due to repeated scattering by the air core which shortens photon transport mean free path[55] and hence strengthens reflection. Moving on to the effect of diameter variation, we find that $\langle \boldsymbol{R} \rangle_\lambda$ increases with increasing $\boldsymbol{d}_{\mathbf{i}}$ / $\boldsymbol{d}_{\mathbf{o}}$ even though $\boldsymbol{d}_{\mathbf{o}}$ is not uniform. In **Fig. 2.2b**, for $\boldsymbol{d}_{\mathbf{i}}$ / $\boldsymbol{d}_{\mathbf{o}} = 0.9$, $\langle \boldsymbol{R} \rangle_\lambda$ generally decreases as the diameter variation extends towards larger $\boldsymbol{d}_{\mathbf{o}}$ and increases as the variation expands to the nanoscale. Notably, $\langle \boldsymbol{R} \rangle_\lambda$ drops by 8.3% from 0.84 to 0.77 as $\boldsymbol{d}_{\mathbf{o}}$ varies from {0.5-1} to 0.5 µm; further increasing $\boldsymbol{d}_{\mathbf{o}}$ to {0.75-1} and 0.75 µm leads to slight reflectivity reductions (to 0.825 and 0.815, respectively) while still maintaining the advantage of the varying- over uniform-diameter design. Hollow SiO_2 microspheres with the varying $\boldsymbol{d}_{\mathbf{o}}$ induce scattering efficiency peaks located differently over the entire solar spectrum (Fig. 2.1b); scattering efficiency dips associated with certain sizes are successfully compensated by others. The diameter variation thus provides broadband solar reflectivity enhancement in the hollow SiO_2 microsphere composites. Note that the distribution of $\boldsymbol{d}_{\mathbf{o}}$ is skewed towards smaller sizes (inset of Fig. 2.2b), however, at the filling ratio of 55 vol%, we do not observe significant effect on the solar reflectivity from varying the current size distribution to a normal one.

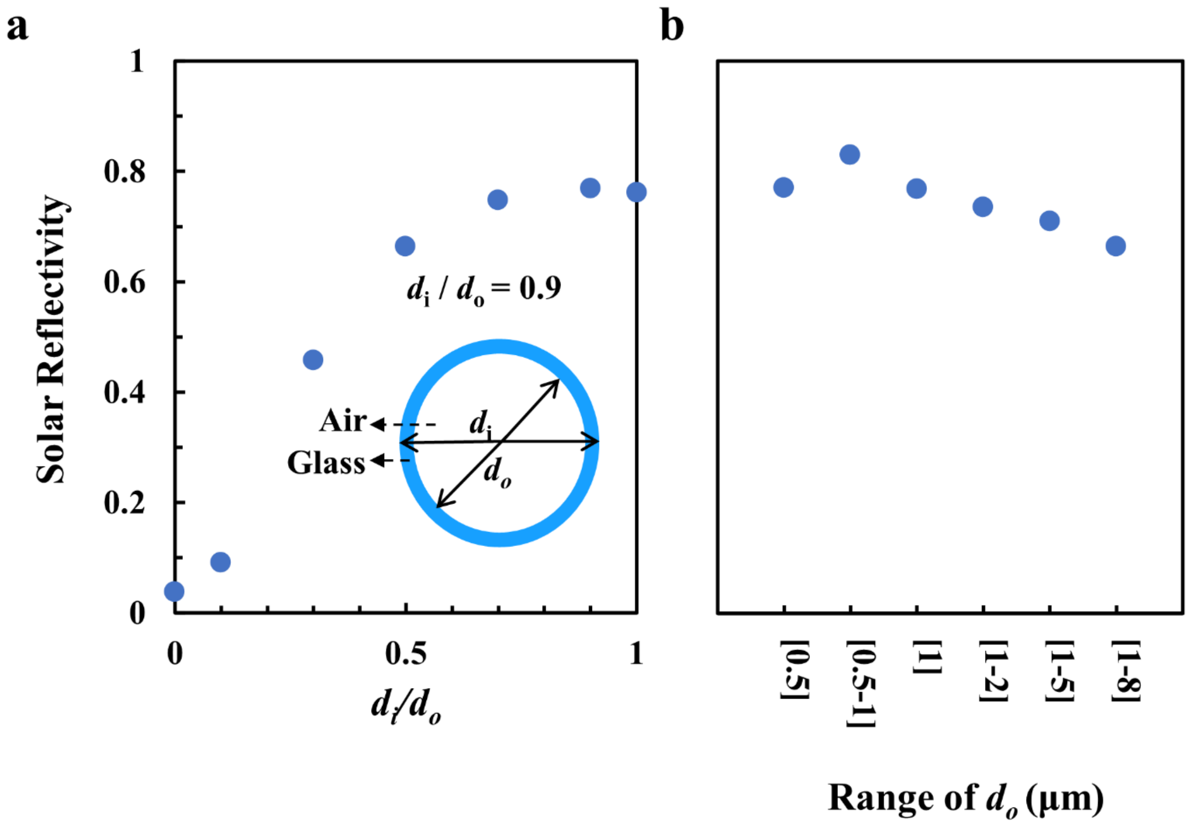

Figure 2.2 Solar reflectivity of hollow glass microspheres. (a) Integrated reflectivity $\langle R \rangle_\lambda$ as a function of shell thickness for uniform-diameter hollow SiO_2 microspheres with $\boldsymbol{d_o}$ = 1 µm in the wavelength of 0.4-2.4 µm. (b) $\langle R \rangle_\lambda$ of varying-diameter hollow SiO_2 microspheres with $\boldsymbol{d_o}$ ranges in {0.5-1}, {1-2}, {1-5}, and {1-8} µm. $\langle R \rangle_\lambda$ computed for the uniform-diameter microspheres, {0.5} and {1} µm, are plotted for comparison. The shell thickness defined by $\boldsymbol{d_i / d_o}$ = 0.9 is studied.

2.3 Effects of Refractive Index and Extinction Coefficient

Our previous analysis[46] has demonstrated that hollow microspheres enable low-refractive-index materials (such as SiO_2) to exhibit high solar reflectivity, and it indicate an enhanced solar reflectivity when hollow SiO_2 microspheres are replaced with hollow TiO_2 microspheres. In the solar region, TiO_2 has a refractive index of ~2.5, which is higher than the refractive index of SiO_2

(~1.45). The refractive index difference between two materials, along with the fact that high-refractive-index materials are commonly used in solar reflective materials, motivate us to study the effect of refractive index in improving solar reflectivity. Previous studies[56,57] proposed various effective medium approximations to predict the dielectric and/or optical properties of composite systems by treating them as homogeneous media with effective refractive index and extinction coefficient values denoted by $\boldsymbol{n_{eff}}$ and $\boldsymbol{k_{eff}}$, respectively. At normal incidence, Fresnel reflectivity[58] on the interface of the composite film can be simplified as $\boldsymbol{R} = \left(\left(\boldsymbol{n_{eff}} - \boldsymbol{n_1}\right)/\left(\boldsymbol{n_{eff}} - \boldsymbol{n_1}\right)\right)^2$, where $\boldsymbol{n_1}$ is the medium from which the irradiance comes. Larger $\boldsymbol{n_{eff}}$ is expected when hollow microspheres with higher-refractive-index materials are dispersed in the composite system, which leads to increasing $\boldsymbol{R}$. In this work, we use the Volume Averaging Theory (VAT)[59,60] in equations (2.1) to (2.3) to calculate $\boldsymbol{n_{eff}}$ and assume $\boldsymbol{n_1}$ to be 1.

$$n_{eff}^2 = \frac{1}{2}\left[A + \sqrt{A^2 + B^2}\right] \tag{2.1}$$

$$A = \varepsilon_{r,eff} = \phi(n_d^2 - k_d^2) + (1 - \phi)(n_c^2 - k_c^2) \tag{2.2}$$

$$B = 2n_d k_d \phi + 2n_c k_c (1 - \phi) \tag{2.3}$$

Where $\boldsymbol{n}$ and $\boldsymbol{k}$ respectively refer to the refractive index and extinction coefficient of the continuous medium (subscript $\boldsymbol{c}$) and the dispersed medium (subscript $\boldsymbol{d}$), and $\boldsymbol{\phi}$ is the volume fraction of the dispersed medium.

Although the analytical model based on effective medium approximations and Fresnel reflectivity equation at normal incidence is able to predict higher $\boldsymbol{R}$ with larger $\boldsymbol{n_{eff}}$, it underestimates $\boldsymbol{R}$ for such hollow-microspheres-based systems with scattering[61] to all the directions and scattering efficiency of hollow microspheres whose dimensions are similar to the solar wavelengths. Thus, FDTD numerical simulations are utilized to investigate the effect of refractive index on solar reflectivity. FDTD is the method providing solutions to Maxwell's equations in a discretized unit cell. We set a unit cell with a dimension of 20 μm × 20 μm in 2D FDTD domain (**Fig. 2.3a**). We choose to work with 2D instead of three-dimensional (3D) unit cells since changing the dimensionality of the simulation does not change the results as the hollow microspheres are symmetric in both 2D and 3D. Inside the unit cell we generated the closely packed random hollow microspheres with a diameter range of 0.5-1 μm and an inner-to-outer diameter ratio d_i/d_o of 0.9[46], which gives a final areal fraction of 58.56%. To evaluate the effect of refractive index (n) in hollow microspheres on solar reflectivity, we set n to wavelength-independent values from 1.5 to 100, while keeping the extinction coefficient as 0. While the realistic ceramic materials does not have a refractive index as high as 100 in the solar region, we set the upper limit extremely large to gain more understandings. We utilize an ideal matrix material by setting the refractive index as 1.45 and extinction coefficient as 0 to eliminate any absorption from the matrix. The matrix is a binding material that can be a polymer such as PDMS.

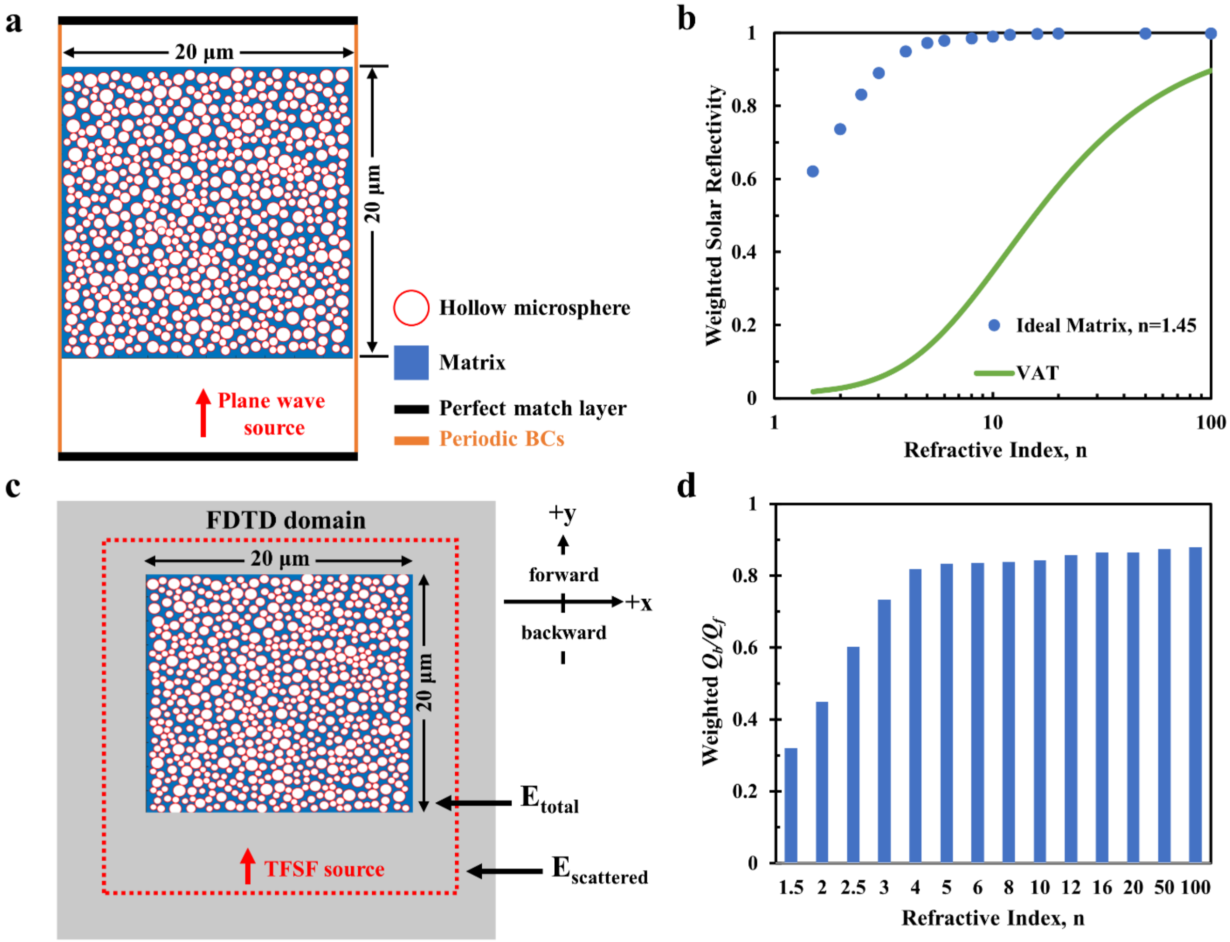

Figure 2.3 The effect of refractive index values (n) in shells of hollow microspheres. (a) The schematic of the 2D FDTD simulation unit cell, showing randomly distributed hollow microspheres with a diameter range of 0.5-1 μm; (b) The weighted solar reflectivity from 0.2 μm to 2.4 μm for different refractive index values from 1.5 to 100 in shells of hollow microspheres using the ideal matrix material (n=1.45, k=0). The areal fraction is kept 58.56%. The analytical results using the VAT model and simplified Fresnel reflectivity is also plotted (green); (c) The schematic of the 2D total-field-scatter-field (TFSF) simulation unit cell; (d) Spectrally average backscattering ratio Q_b/Q_f of different n values in shells of hollow microspheres with varying diameters of 0.5 μm to 1 μm and d_i/d_o=0.9. In TFSF unit cells, the areal fractions are all 59.17%.

After we obtain the spectral reflectivity, we calculated the weighted solar reflectivity ($R_{weighted}$) based on solar spectrum distribution[7]:

$$R_{weighted} = \frac{\int_{0.2}^{2.4} R(\lambda) I_{AM1.5}(\lambda) d\lambda}{\int_{0.2}^{2.4} I_{AM1.5}(\lambda) d\lambda} \quad (2.4)$$

Where $I_{AM1.5}(\lambda)$ is the solar irradiance with an air mass of 1.5. When we set ***n*** value to 1.5, $\boldsymbol{R_{weighted}}$ is 0.6215 for the ideal matrix whose ***n***=1.45. It is evident from **Fig. 2.4** and **Fig. 2.3b** that $\boldsymbol{R_{weighted}}$ increases with increasing ***n*** and the increment becomes asymptotically smaller with ***n*** approaching 100. The solar reflectivity is reduced slightly when PDMS is used as the matrix material (**Fig. 2.4c**) because of its inherent properties[54]. In Fig. 2.3b we show the analytical results calculated using $\boldsymbol{n_{eff}}$ calculated from VAT[59,60] defined in equation (2.1) to (2.3) and simplified Fresnel reflectivity equation at normal incidence assuming $\boldsymbol{n_1}$ equals to 1 as a comparison. The difference between FDTD results and VAT calculations can be explained by the scattering efficiency of the hollow microspheres whose dimensions are similar as the solar wavelengths[62], which cannot be captured in the effective medium approximations[63,64]. The enhancement of $\boldsymbol{R_{weighted}}$ is further evidenced in FDTD computations using a Total-Field-Scatter-Field (TFSF) source (**Fig. 2.3c**), which is generally used to capture the scattering efficiency of the structure[65,66]. The forward scattering efficiency ($\boldsymbol{Q_f}$) and the backward scattering efficiency ($\boldsymbol{Q_b}$) are both simulated and we use a backward-to-forward scattering ratio $\boldsymbol{Q_b/Q_f}$ to represent the capability of the structure to backscatter incident irradiance. As shown in **Fig. 2.3d**, spectrally integrated $\boldsymbol{Q_b/Q_f}$ increases from 0.3202 to 0.8783 as ***n*** increases from 1.5 to 100, which agrees with $\boldsymbol{R_{weighted}}$ enhancement in FDTD computations using a plane wave source.

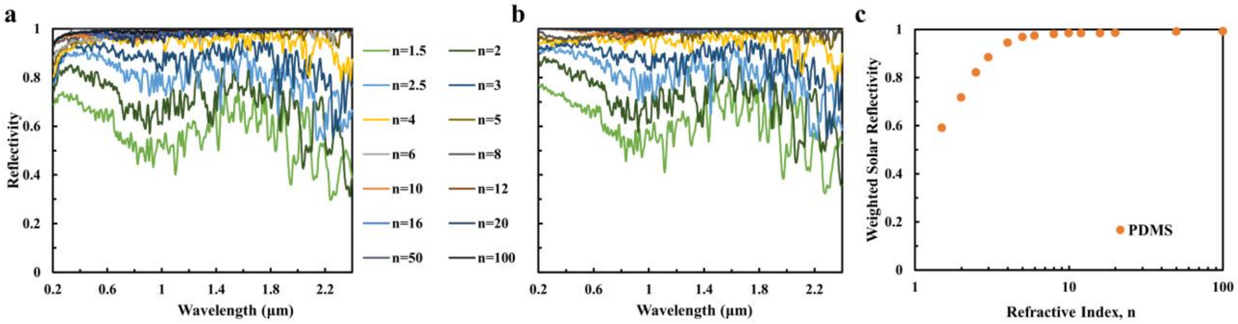

Figure 2.4 The solar reflectivity Spectrum of hollow-microsphere-based composites with different refractive index values using (a) PDMS and (b) ideal matrix material (n=1.45, k=0) as the matrix. The refractive index of the shell is set from 1.5 to 100 while keeping the extinction coefficient as 0; (c) The weighted solar reflectivity $\boldsymbol{R_{weighted}}$ as a function of refractive index values from 1.5 to 100, with PDMS being the matrix material.

After understanding the effect of $\boldsymbol{n}$ values in solar reflectivity, we investigate the effect of extinction coefficients ($\boldsymbol{k}$) with the same model. For each $\boldsymbol{n}$, we vary $\boldsymbol{k}$ values from 10^{-6} to 10^{0}. **Fig. 2.5a** and **Fig. 2.6a** show the effect of $\boldsymbol{k}$ values while $\boldsymbol{n}$=1.45. When we set $\boldsymbol{k}$ value as 10^{0}, $\boldsymbol{R_{weighted}}$ is only 0.0559 in the solar region of 0.2-2.4 μm. Decreasing $\boldsymbol{k}$ value from 10^{0} to 10^{-4} leads to increased $\boldsymbol{R_{weighted}}$ from 0.0559 to 0.5908. It is also noticed that $\boldsymbol{R_{weighted}}$ remains almost unchanged when $\boldsymbol{k}$ changes from 10^{-4} to 10^{-6}. The increase in $\boldsymbol{R_{weighted}}$ is only 0.62%. We further calculate the spectral absorptivity **ε(λ)**=1-R(λ)-T(λ) and weighted solar absorptivity ($\varepsilon_{weighted}$) values based on the solar spectrum distribution:

$$\varepsilon_{weighted} = \frac{\int_{0.2}^{2.4} \varepsilon(\lambda) I_{AM1.5}(\lambda) d\lambda}{\int_{0.2}^{2.4} I_{AM1.5}(\lambda) d\lambda} \tag{2.5}$$

It is evident from **Fig. 2.6b** that $\varepsilon_{weighted}$ in the solar region decreases with decreasing $\boldsymbol{k}$ from 10^{0} to 10^{-6} and approaches 0 when $\boldsymbol{k}$ is equal to or smaller than 10^{-4}, when n equals to 1.5.

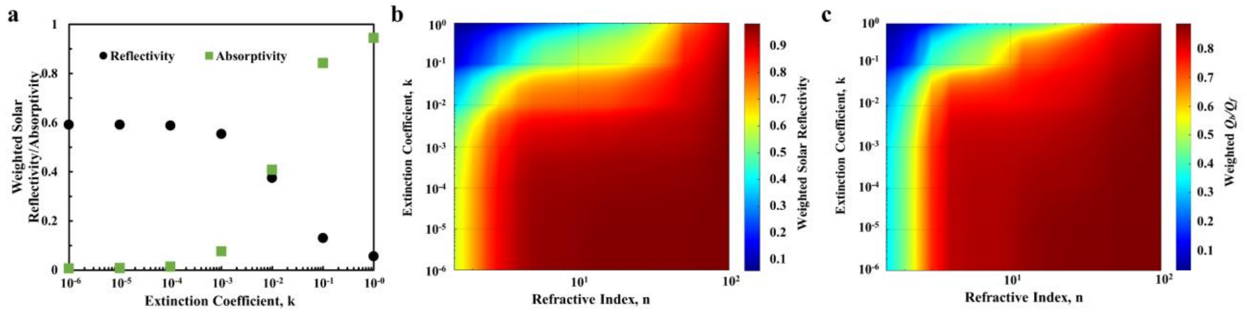

Figure 2.5 The effect of extinction coefficient values (k) in shells of hollow microspheres. (a) The solar reflectivity spectrum from 0.2 μm to 2.4 μm for different extinction coefficient values from 10^{-6} to 10^{0} in shells of hollow microspheres, with the refractive index value (n) setting to 1.5. n is set to 1.5 as an example to show the significant effect of extinction coefficient on the solar reflectivity and absorptivity; (b) Weighted solar reflectivity $\boldsymbol{R_{weighted}}$ and (c) weighted backward-to-forward scattering ratio $\boldsymbol{Q_b/Q_f}$ from 0.2 μm to 2.4 μm as a function of refractive index values and extinction coefficient values in shells of hollow microspheres with varying diameters of 0.5-1 μm and $\boldsymbol{d_i/d_o}$=0.9. The areal fraction of hollow microspheres is set to 58.56%. Color legends are used to represent weighted solar reflectivity and weighted $\boldsymbol{Q_b/Q_f}$ values.

The similar trend is observed as well when $\boldsymbol{n}$ value is increased and $\boldsymbol{k}$ value is varied. Using $\boldsymbol{n}$ values ranging from 1.5 to 100 and $\boldsymbol{k}$ values ranging from 10^{-6} to 10^{0}, $\boldsymbol{R_{weighted}}$ can be plotted as a function of both values, as shown in **Fig. 2.5b**. It is noticed that when $\boldsymbol{n}$ is as large as 20 or more, $\boldsymbol{R_{weighted}}$ at extinction coefficient equals to 1 is more than 0.8 and the solar reflectivity increment with decreasing $\boldsymbol{k}$ is much smaller compared to the increment at $\boldsymbol{n}$=1.5. This phenomenon can also be found when we evaluate the backward-to-forward scattering ratio $\boldsymbol{Q_b/Q_f}$ using the TFSF source in the simulations (**Fig. 2.5c**). We believe the plots could provide the material selection guidance for a combination of two components in optical constants to achieve desired solar reflectivity, which could be used to perfect solar reflectivity optimization.

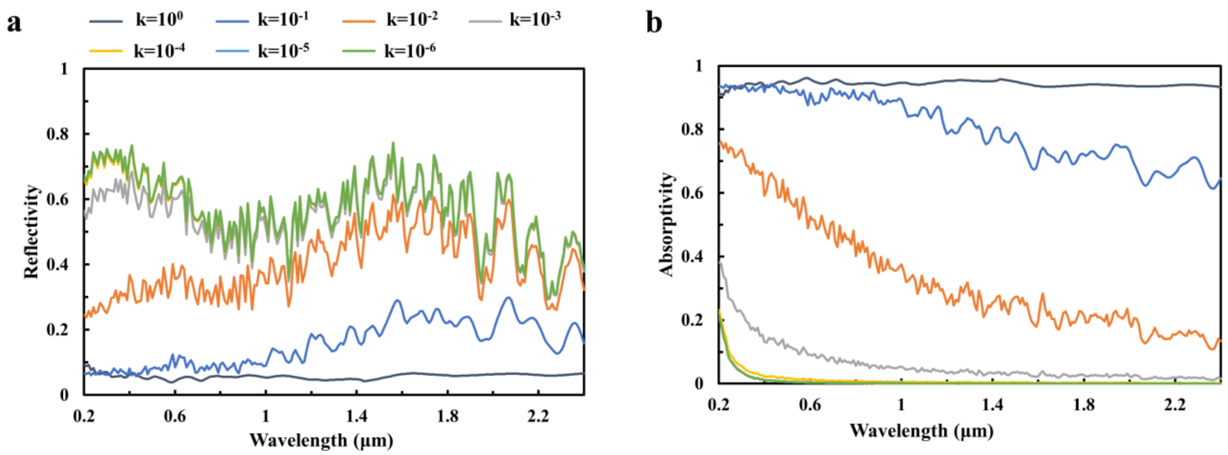

Figure 2.6 The effect of extinction coefficient values on optical properties of hollow-microsphere-based composites with the ideal matrix material (n=1.45, k=0). (a) The solar reflectivity spectrum and (b) solar absorptivity spectrum of hollow-microsphere-based composites with different extinction coefficient. The extinction coefficient of the shell is set from 10^{-6} to 10^{0} while keeping the refractive index value (n) as 1.5. n is set to 1.5 as an example to show the significant effect of extinction coefficient on the solar reflectivity and absorptivity.

2.4 Promising Materials for High Solar Reflectivity

The investigations on the effect of ***n*** and ***k*** values indicate that materials with a high ***n*** and low ***k*** in the solar region are preferred for a high solar reflectivity in such hierarchical hollow-microsphere-embedded polymeric systems. We have previously demonstrated high solar reflectivity by integrating SiO_2 hollow microspheres within PDMS[29,46], and we would like to find out some other material candidates that could also be promising to achieve high solar reflectivity. Here several ceramic materials are chosen since they exhibit similar optical constants as SiO_2. **Fig. 2.7a** and **Fig. 2.7b** shows ***n*** and ***k*** values of SiO_2, TiO_2, Yttrium oxide (Y_2O_3), Magnesium fluoride (MgF_2), Cerium trifluoride (CeF_3) and Strontium fluoride (SrF_2). All the optical constants are obtained from previous publications[67–70], and optical constants of MgF_2 and CeF_3 are only from wavelength of 0.2 μm to 2 μm according to previous work[67]. It can be seen that TiO_2 has the highest ***n*** value in the solar region and a very high ***k*** value in the ultraviolet region. When we use these optical constants as the input for our 2D FDTD computations while using the ideal matrix material (**Fig. 2.7c**), we can compare the solar reflectivity spectrum in **Fig. 2.7d** and average reflectivity values in three separate regions in the solar wavelength region in **Table 2.1**. The solar wavelength of 0.2-2.4 μm can be divided into three separate regions[7]: ultraviolet (UV) region in 0.2-0.4 μm, visible region in 0.4-0.8 μm and near-infrared (NIR) region in 0.8-2.4 μm. Our simulation results indicate that with a thickness of 20 μm, Y_2O_3 hollow microsphere contributes to the highest $\boldsymbol{R_{weighted}}$ of 0.7154, due to its high ***n*** and low ***k*** value throughout the entire solar region. Because of 6% solar irradiation intensity in the UV region, $\boldsymbol{R_{weighted}}$ of Y_2O_3 is higher than that of TiO_2 ($\boldsymbol{R_{weighted}}$=0.7076). The comparison between SiO_2 or Y_2O_3 hollow-microsphere-based composite using PDMS as the matrix material with porous PDMS (**Fig. 2.8**) indicate that hollow microspheres are more effective in achieving higher solar reflectivity than hierarchical porous polymer. Compared to previously reported SiO_2 hollow microspheres, Y_2O_3 hollow microspheres exemplify its potential application in perfect solar reflectors.

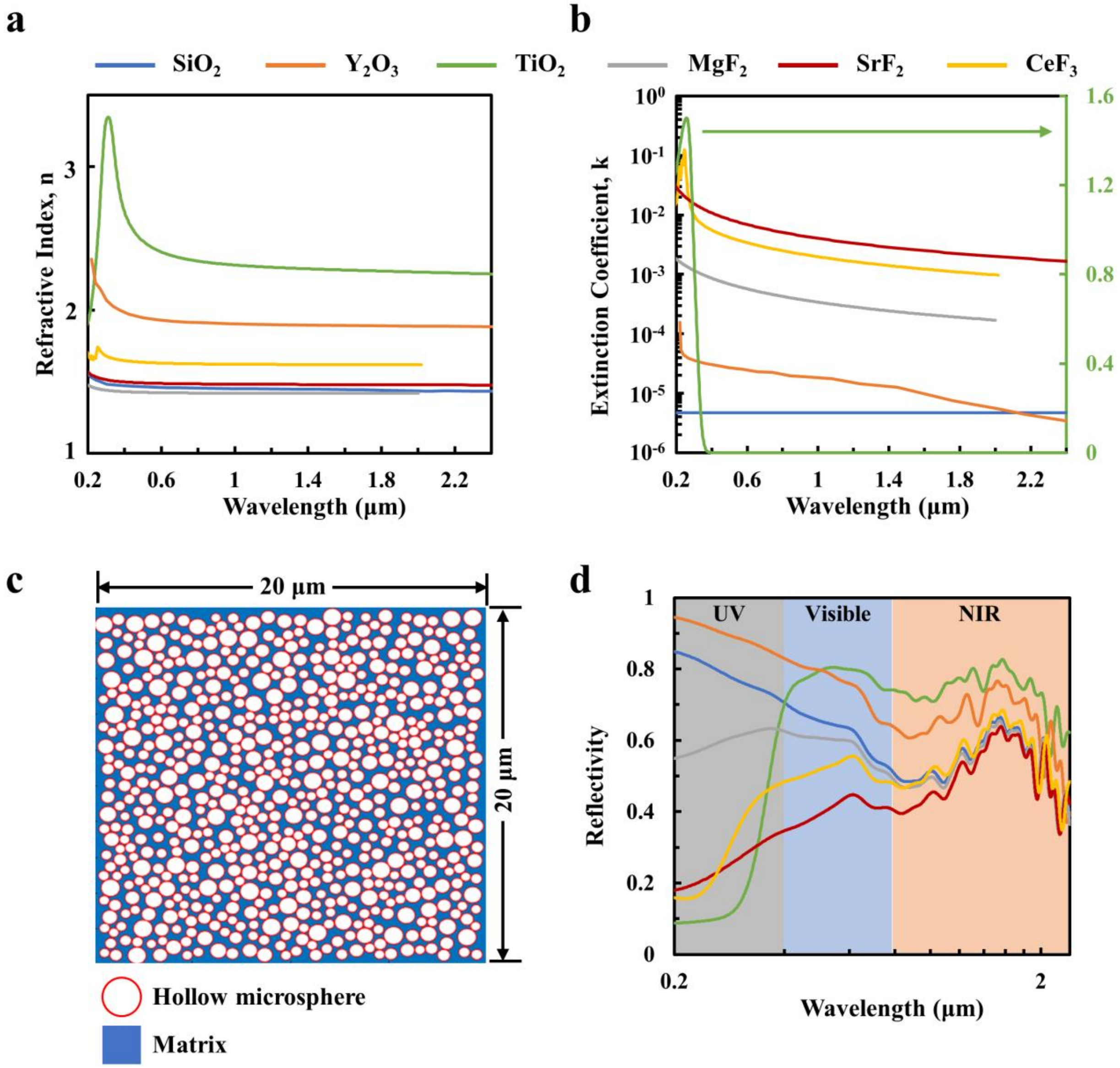

Figure 2.7 The solar reflectivity of hollow-microsphere-embedded composite systems with naturally existing or commonly used pigment materials. (a) The refractive index values and (b) extinction coefficient values from 0.2-2.4 μm for various naturally existing or commonly used pigment materials. For MgF_2 and CeF_3, the refractive index and extinction coefficient values are in the wavelength region of 0.2-2 μm. The extinction coefficient curve of TiO_2 corresponds to y-axis in the right, while other curves correspond to the y-axis on the left; (c) The schematic of the composite system used in the FDTD simulations. The composite includes the ideal matrix material (n=1.45, k=0) and hollow microspheres with varying diameters of 0.5-1

μm and $\boldsymbol{d_i/d_o}$=0.9. The areal fraction of hollow microspheres is 58.56%. The thickness used in the simulations is 20 μm for all composites; (d) The solar reflectivity spectrum in the wavelength region of 0.2-2.4 μm for different materials. The solar wavelength region is divided into three parts: ultraviolet (UV) region, visible region and near-infrared (NIR) region.

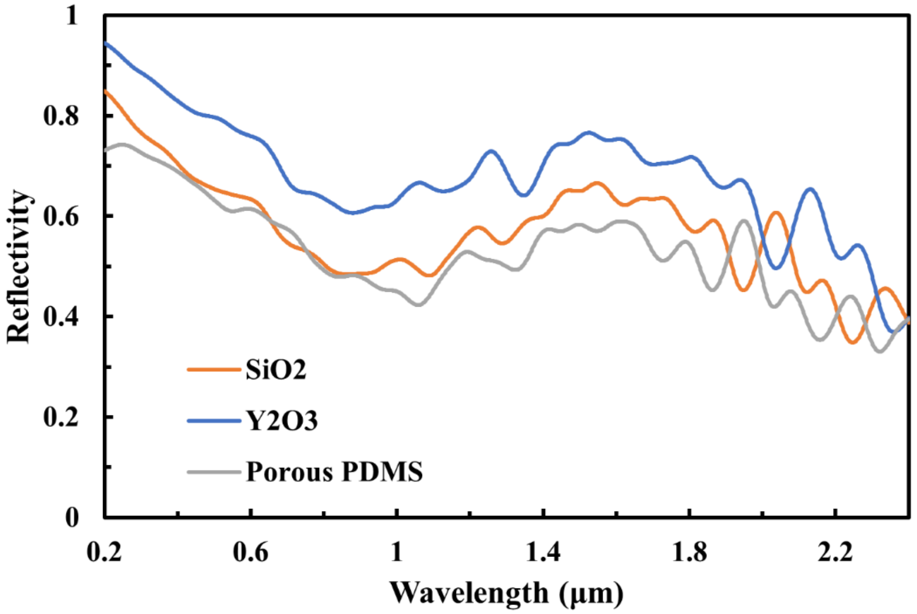

Figure 2.8 The solar reflectivity of PDMS/hollow microsphere composites with shell made of SiO_2, Y_2O_3 and air (which is porous PDMS).

Materials	UV (0.2-0.4 μm)	Visible (0.4-0.8 μm)	NIR (0.8-2.4 μm)	$R_{weighted}$
SiO_2	0.7770	0.6096	0.5360	0.5873
TiO_2	0.2489	0.7589	0.7288	0.7076
Y_2O_3	0.8888	0.7401	0.6643	0.7154
MgF_2	0.6054	0.5720	0.5253	0.5525
SrF_2	0.2652	0.4080	0.5066	0.4438
CeF_3	0.3299	0.5133	0.5514	0.5178

Table 2.1 The reflectivity values of the hollow microsphere embedded composite systems with various pigment materials in three different wavelength regions: UV region (0.2-0.4 μm), visible region (0.4-0.8 μm) and NIR region (0.8-2.4 μm). $R_{weighted}$ is calculated based on equation (2.19).

We have demonstrated that Y_2O_3 hollow microsphere contributes to a $R_{weighted}$ of 0.7154 with a thickness of 20 μm and it indicates the potential of Y_2O_3 hollow microspheres for broadband near-perfect solar reflectors. We thus study the thickness dependence of Y_2O_3 hollow-microsphere-based composite systems. We set the thickness to 20, 50, 100 and 300 μm (**Fig. 2.9a**), which are some general thicknesses used for coatings[18,23,43], while maintaining the areal fraction as 58.56%. It shows that with a higher thickness of 50, 100 and 300 μm, $R_{weighted}$ is enhanced to 0.8504, 0.9226 and 0.9664 respectively (**Fig. 2.9b**). Besides FDTD simulations, we also study the thickness dependence using the diffusion theory[23,27,55,71,72] involving transport mean free path (l^*), which is the length over which the direction of propagation of the photon is randomized. The diffusion theory relates transmissivity of the composite system (T) to its thickness (L) by the following equation[23,27,72]:

$$T = \frac{l^*(1+s)}{L+2l^*s} \tag{2.6}$$

In equation (2.6), ***s*** is the extrapolation length ratio that can be calculated using ***s=2(1+R)/[3(1-R)]***, where ***R*** is the internal reflectance. The Volume-Averaging-Theory (VAT)[59,60] and the Maxwell-Garnett Theory (MGT)[57] are used to estimate the value of ***s*** by using the refractive index of Y_2O_3 (n=1.9) and PDMS (n=1.45), and the areal fraction of 58.56%. We here use the spectrally independent refractive index value of Y_2O_3 in the calculation for convenience and using the spectrally dependent refractive index would help to estimate the spectrally dependent transmissivity. The spectral reflectivity (R_s) is calculated using $R_s=1-T$. **Fig. 2.9c** indicate the thickness dependence on solar reflectivity of Y_2O_3 hollow-microsphere-based composites with an ideal matrix material from a thickness of 20 μm to 1000 μm using the diffusion theory, which shows the agreement with the FDTD simulation results with a thickness of 20 μm, 50 μm, 100 μm and 300 μm. Both MGT and VAT approximations show identical predictions on the thickness-dependence (**Fig. 2.10**), which indicate a solar reflectivity beyond 0.98 for a thickness of larger than 500 μm. The solar reflectivity we demonstrate here is among the highest solar reflectivity for such polymeric systems with similar thicknesses (**Table 2.2**) and we believe Y_2O_3 hollow microspheres is promising to achieve near-perfect solar reflectivity which benefits applications for spacecrafts, buildings, or electronics.

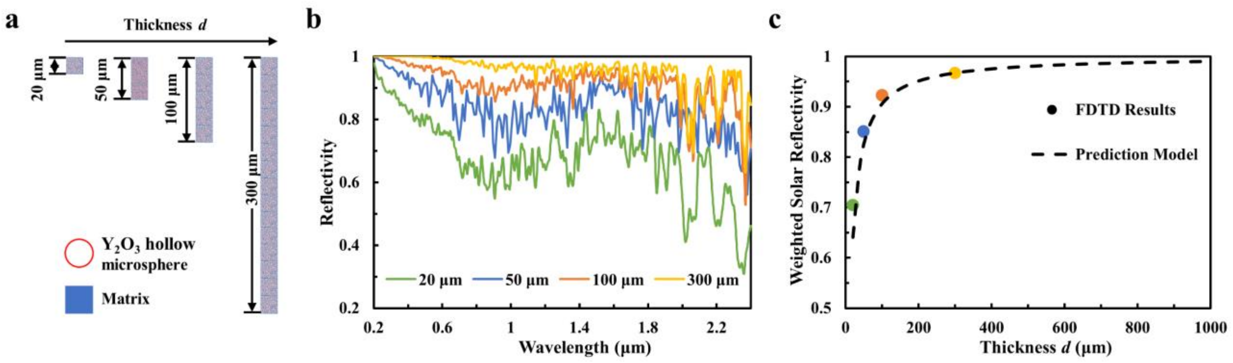

Figure 2.9 The solar reflectivity of Y_2O_3 hollow-microsphere-based composites with various thicknesses. (a) The schematic of Y_2O_3 hollow-microsphere-based composites with a thickness of 20 μm, 50 μm, 100 μm and 300 μm. The parameter ***d*** is used to stand for the thickness of the composite; (b) The solar reflectivity spectrum in the wavelength region of 0.2-2.4 μm with a thickness of 20 μm, 50 μm, 100 μm and 300 μm; (c) FDTD simulated weighted solar reflectivity as a function of thickness in Y_2O_3 hollow-microspheres-based composites and reflectivity predictions based on the diffusion theory with transport mean free path calculations for a thickness of 20-1000 μm. The weighted solar reflectivity $\boldsymbol{R}_{weighted}$ is calculated using equation (2.19) in the main text and the prediction model uses the Volume Averaging Theory (VAT) defined in equation (2.16) to (2.18) and the diffusion theory in equation (2.21).

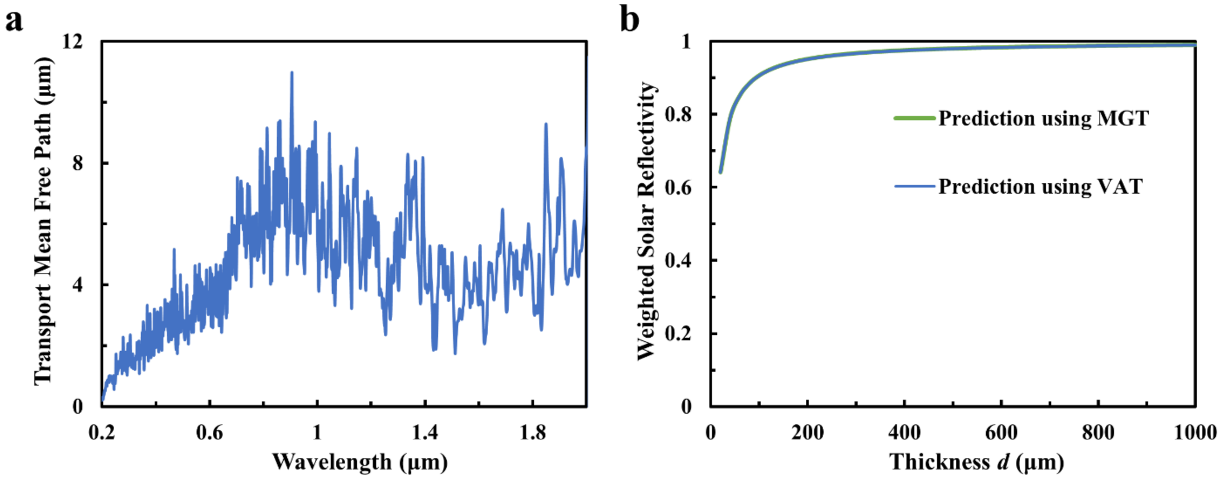

Figure 2.10 Solar reflectivity prediction model of PDMS/Y_2O_3 hollow microsphere systems based on the diffusion theory involving transport mean free path (***l****). (a) The transport mean free path as a function of

wavelength in the PDMS/Y_2O_3 hollow microsphere system with a 20-μm thickness; (b) The comparison of thickness dependence prediction results using the Maxwell-Garnett Theory (MGT) or Volume Averaging Theory (VAT), showing the almost identical prediction results of two effective medium approximations.

Materials	Experiment/Simulation	Thickness	Weighted Solar Reflectivity	References
Randomly packed SiO_2 microsphere	Experiment	700 μm	0.9926	44
6% SiO_2+TPX matrix+200 nm Ag	Experiment	50 μm	0.9517	1
Hierarchical porous PVDF-HFP	Experiment	100 μm	0.86	2
		150 μm	0.875	
		200 μm	0.9	
		300 μm	0.96	
		480 μm	0.98	
TiO_2 nanoparticles+ resin	Experiment	2 mm	0.87	21
	Simulation	1 mm	0.91	
$CaCO_3$+resin	Experiment	98 μm	0.889	44
		131 μm	0.934	
		177 μm	0.951	
		400 μm	0.955	
TiO_2+hollow thermoplastic microspheres	Experiment	600 μm	0.8546	45

Table 2.2 State-of-the-art polymeric systems with high solar reflectivity in previous publications.

2.5 Conclusions

To sum up, we have studied the solar reflectivity in the 0.2-2.4 µm wavelength range of solid and hollow microspheres with the diameter varying from 0.125 to 8 µm using Mie theory and FDTD simulations. SiO_2 and TiO_2 are considered as low- and high-refractive-index microsphere materials while the PDMS is considered as a polymer matrix. Our analysis has shown that hollow microspheres with a thinner shell are more effective in scattering light, compared solid microspheres, and lead to a higher solar reflectivity up to 20 times. The high scattering efficiency, owing to the refractive-index contrast and large interface density, in hollow microspheres allows low-refractive-index materials to have a high solar reflectivity of 0.77, which is only 8.3% less than that of solid TiO_2 microspheres. When the diameter is uniform, 0.75 µm SiO_2 hollow microspheres provide the largest solar reflectivity of 0.81. When the diameter is varying, the random distributed 0.5-1 µm SiO_2 hollow microspheres provide the largest solar reflectivity of 0.84. We investigate the effects of refractive index and extinction coefficient values on solar reflectivity in randomly distributed hierarchical hollow microsphere with a diameter range of 0.5-1 µm and an inner-to-outer diameter ratio $\boldsymbol{d_i/d_o}$ of 0.9 using FDTD simulations. The weighted solar reflectivity ($\boldsymbol{R_{weighted}}$) in the wavelength region of 0.2-2.4 µm increases from 0.5902 to 0.9913 as the refractive index increases from 1.5 to 100 due to enhanced backscattering, which is supported by the increasing value of backward-to-forward scattering ratio $\boldsymbol{Q_b/Q_f}$. We also demonstrate that solar reflectivity enlarges with a smaller extinction coefficient because of weaker solar absorption. By implementing with various refractive index values from 1.5 to 100 and extinction coefficient values from 10^{-6} to 10^{0} we obtain the contour plots showing $\boldsymbol{R_{weighted}}$ and $\boldsymbol{Q_b/Q_f}$ variations, which provide the guideline for material selections for broadband perfect solar reflectivity. Our study indicates ceramic materials with the combination of high refractive index and low extinction coefficient values such as Y_2O_3 are promising candidates. Our FDTD simulation indicates a $\boldsymbol{R_{weighted}}$ of 0.9664 with a 300-µm thickness with Y_2O_3 hollow microspheres. In addition, the diffusion theory we utilize in Y_2O_3 hollow-microspheres-based composite indicates a $\boldsymbol{R_{weighted}}$ of 0.98 at a 500-µm thickness and 0.99 at a 1-mm thickness. This work helps to identify the desired optical constants to achieve a broadband perfect solar reflectivity when combined with the hierarchical hollow microsphere designs and provides a material selection guidance for pigment-embedded polymeric materials. We believe this work provides the findings that can be potentially utilized to optimize solar reflectivity or radiative cooling performance for deep-space and building applications.

2.6 Approach and Methods

2.6.1 Mie Theory

The scattering coefficients of individual hollow microspheres are computed based on Mie theory formalism adopted for core-shell particles and the open source program developed by Matzler. The scattering, extinction, and absorption efficiencies are outlined as the following

$$Q_{sca} = \frac{2}{x^2}\sum_{n=1}^{\infty}(2n+1)(|a_n|^2 + |b_n|^2) \tag{2.7}$$

$$Q_{ext} = \frac{2}{x^2}\sum_{n=1}^{\infty}(2n+1)\mathrm{Re}(a_n + b_n) \tag{2.8}$$

$$Q_{abs} = Q_{ext} - Q_{sca} \tag{2.9}$$

The coefficients a_n and b_n are

$$a_n = \frac{\left(\widetilde{D}_n/m_2 + \frac{n}{y}\right)\psi_n(y) - \psi_{n-1}(y)}{\left(\widetilde{D}_n/m_2 + \frac{n}{y}\right)\xi_n(y) - \xi_{n-1}(y)} \tag{2.10}$$

$$b_n = \frac{\left(m_2\widetilde{G}_n + \frac{n}{y}\right)\psi_n(y) - \psi_{n-1}(y)}{\left(m_2\widetilde{G}_n + \frac{n}{y}\right)\xi_n(y) - \xi_{n-1}(y)} \tag{2.11}$$

where the size parameters are defined for both core and shell as $x = \frac{2m_1\pi r_1}{\lambda}$, and $y = \frac{2m_2\pi r_2}{\lambda}$ with r_1 and r_2 being their radii, respectively. The coefficients $\widetilde{D}_n$ and $\tilde{G}_n$ are given by

$$\widetilde{D}_n = \frac{D_n(m_2x) - A_n\chi_n'(m_2y)/\psi_n(m_2y)}{1 - A_n\chi_n(m_2y)/\psi_n(m_2y)} \tag{2.12}$$

$$\widetilde{G}_n = \frac{D_n(m_2x) - B_n\chi_n'(m_2y)/\psi_n(m_2y)}{1 - B_n\chi_n(m_2y)/\psi_n(m_2y)} \tag{2.13}$$

Where

$$A_n = \psi_n(m_2x)\frac{mD_n(m_1x) - D_n(m_2x)}{mD_n(m_1x)\chi_n(m_2x) - \chi_n'(m_2x)} \tag{2.14}$$

$$B_n = \psi_n(m_2x)\frac{D_n(m_1x)/m - D_n(m_2x)}{D_n(m_1x)\chi_n(m_2x)/m - \chi_n'(m_2x)} \tag{2.15}$$

with effective optical indices defined by m_1 and m_2 for the core and shell, and $m = \frac{m_2}{m_1}$.

2.6.2 Finite-Difference-Time-Domain Simulation

A two-dimensional Finite-Difference-Time-Domain (FDTD) method is used in calculating the wavelength-dependent reflectivity and transmissivity of the PDMS/hollow microsphere structure using commercial Lumerical FDTD solver. A plane wave source with the normal incidence is used and the perfect matching layers (PML) are applied in the direction of propagating wave source to serve as the absorbing boundaries. The periodic boundary conditions are applied perpendicular to the wave source. The unit cell is set to 20 μm × 20 μm (for thickness-dependent study, the thickness of the unit cell are from 20 μm to 300 μm while the width is kept as 20 μm). The random particle generation algorithm inside the software is modified to generate randomly distributed hollow microspheres inside the unit cell and areal fraction is calculated to be 58.56% when the algorithm stops particle generation. The inner-to-outer diameter ratio $\boldsymbol{d}_{\mathbf{i}}$ / $\boldsymbol{d}_{\mathbf{o}}$ is set to 0.9 and the diameter range is set as 0.5-1 μm, which are confirmed to exhibit highest reflectivity in our previous work8 on PDMS/hollow SiO_2 microsphere composite. The refractive index of the void inside the hollow microspheres is 1. The refractive index of PDMS and materials we study are from previous references.

2.6.3 Effective Medium Approximations

Previous studies proposed several effective medium approximations to predict the dielectric and/or optical properties of composite systems by treating them as homogeneous media with effective refractive index and extinction coefficient values denoted as $\boldsymbol{n_{eff}}$ and $\boldsymbol{k_{eff}}$, respectively. At normal incidence, Fresnel reflectivity can be simplified as $\boldsymbol{R} = \left((\boldsymbol{n_{eff}} - \boldsymbol{n_1})/(\boldsymbol{n_{eff}} + \boldsymbol{n_1})\right)^2$, where $\boldsymbol{n_1}$ is the medium from which the irradiance comes.

The most commonly used effective medium approximations for the effective refractive index predictions are series, parallel, Maxwell-Garnett Theory (MGT), and VAT models. The MGT models is expressed for both three-dimensional (3D) spherical inclusions and two-dimensional (2D) cylindrical inclusions. For the composite system in this work, we work with 3D MGT models.

The series model can be expressed as

$$\frac{1}{n_{eff}} = \frac{1-\phi}{n_c} + \frac{\phi}{n_d} \tag{2.16}$$

In the equation, *n* refers to the refractive index of the continuous medium (subscript *c*) and the dispersed medium (subscript *d*), and ϕ is the volume fraction of the dispersed medium.

The parallel model can be expressed as

$$n_{eff} = (1-\phi)n_c + \phi n_d \tag{2.17}$$

The 3D MGT models can be expressed as

$$n_{eff}^2 = n_c^2\left[1 - \frac{3\phi(n_c^2 - n_d^2)}{2n_c^2 + n_d^2 + \phi(n_c^2 - n_d^2)}\right] \tag{2.18}$$

The VAT model can be expressed as

$$n_{eff}^2 = \frac{1}{2}\left[A + \sqrt{A^2 + B^2}\right] \tag{2.19}$$

$$A = \varepsilon_{r,eff} = \phi(n_d^2 - k_d^2) + (1-\phi)(n_c^2 - k_c^2) \tag{2.20}$$

$$B = 2n_d k_d \phi + 2n_c k_c (1-\phi) \tag{2.21}$$

In the VAT model equations, $\boldsymbol{k}$ refers to the extinction coefficient of the continuous medium (subscript *c*) and the dispersed medium (subscript *d*).

By setting the refractive index of the shell in hollow microspheres is from 1.5 to 100, we can first calculate $\boldsymbol{n_{eff}}$ of hollow microspheres using these models, assuming an inner-to-outer diameter ratio $\boldsymbol{d_i/d_o}$ of 0.9 and a refractive index of 1 for the void inside hollow microspheres. After getting $\boldsymbol{n_{eff}}$ of hollow microspheres, we can predict $\boldsymbol{n_{eff}}$ **[Fig. S1(a)]** and reflectivity **[Fig. S1(b)]** of the composite system using these models assuming the refractive index of the matrix is 1.45 and an areal fraction of 58.56%.

It is noticed that series model and VAT model predict increased n_{eff} and Fresnel reflectivity with increasing refractive index in hollow microspheres, while parallel and 3D MGT models failed to estimate the increase trend. Therefore, VAT model is chosen as an example in the main manuscript to show the increased reflectivity with higher-refractive-index materials dispersed in the hollow-microsphere-embedded composite system.

2.6.4 Comparison between 2D and 3D Simulations

We try to create the 3D FDTD simulation models via modifications of our random particle generation code. The dimension of the 3D unit cell is set to 5 μm × 5 μm × 20 μm, so that the thickness of the unit cell is kept as 20 μm. A plane wave source with the normal incidence is placed in the z-direction. The perfect matching layers (PML) are applied in the direction of propagating wave source to serve as the absorbing boundaries and the periodic boundary conditions are applied perpendicular to the wave source. Inside the unit cell, we generated the closely packed random hollow microspheres with a diameter range of 0.5-1 μm and an inner-to-outer diameter ratio d_i/d_o of 0.9. After around 10-hour generation time, 1142 microspheres are randomly distributed inside the unit cell and give a volume fraction of 48.25%. The volume fraction is defined as the fraction of total volumes of 3D microspheres over the volume of the unit cell and can be calculated as $Volume\ Fraction = \sum_{i=1}^{N} \frac{4}{3}\pi r_i^3 / (5 \times 5 \times 20)$, where r_i is the radius of ***i***th microsphere with a unit of μm and N is the total number of microspheres.

To evaluate the effect of refractive index (n) in 3D hollow microspheres on solar reflectivity, we set n to wavelength-independent values of 1.5, 2 and 2.5, while keeping the extinction coefficient as 0. We utilize an ideal matrix material by setting the refractive index as 1.45 and extinction coefficient as 0 to eliminate any absorption from the matrix, as we have done for 2D FDTD simulations.

Although the volume fraction of 3D microspheres is 48.25%, lower than the areal fraction of 58.56% in 2D simulations, it is found that the 3D simulation requires much larger memory and takes much longer time compared to 2D simulations. When using the same FDTD settings, the 3D simulation with a unit cell of 5 µm × 5 µm × 20 µm requires 8.46 GB for the initialization, 15.59 GB to run the simulation and 22.73 GB for the data collection, while 2D simulation only requires 230 MB for initialization and mesh, 228 MB to run the simulation and 225 MB for the data collection. In terms of the total number of FDTD Yee nodes, the 3D simulation contains 72.14 million nodes while the 2D simulation contains 1.90 million nodes. We run a 3D simulation on a lab workstation with a 64-GB memory and it takes about 120 hours (5 days) to finish. The expensive memory requirements and ultralong simulation running time in 3D simulations, as well as large differences in numbers of Yee nodes between 2D and 3D simulations, is another reason we choose to work with 2D simulations.

With the 3D unit cell with randomly distributed hollow microspheres inside **(Fig. 2.11a)**, we run 3D simulations with $\boldsymbol{n}$ values of 1.5, 2 and 2.5, while keeping the extinction coefficient as 0. The reflectivity spectrums are presented in **Fig. 2.11b**. We also run three more 2D simulations for $\boldsymbol{n}$ values of 1.5, 2 and 2.5, with 517 hollow microspheres inside a 20 µm × 20 µm unit cell and an areal fraction of 48.26% **(Fig. 2.11c)**, to match the volume fractions of 2D and 3D simulations. $\boldsymbol{R_{weighted}}$ values of 2D and 3D simulations are plotted in **Fig. 2.11d**. It is evident from Fig. 2.11d that $\boldsymbol{R_{weighted}}$ increases with increasing $\boldsymbol{n}$ in either 2D or 3D simulations, and the values are close between 2D and 3D simulations. Although we have limited numbers of 3D simulations done, the results in Fig. 2.11 should help to show the same effect of refractive index (***n***) values on solar reflectivity as what we report in our manuscript using 2D simulations.

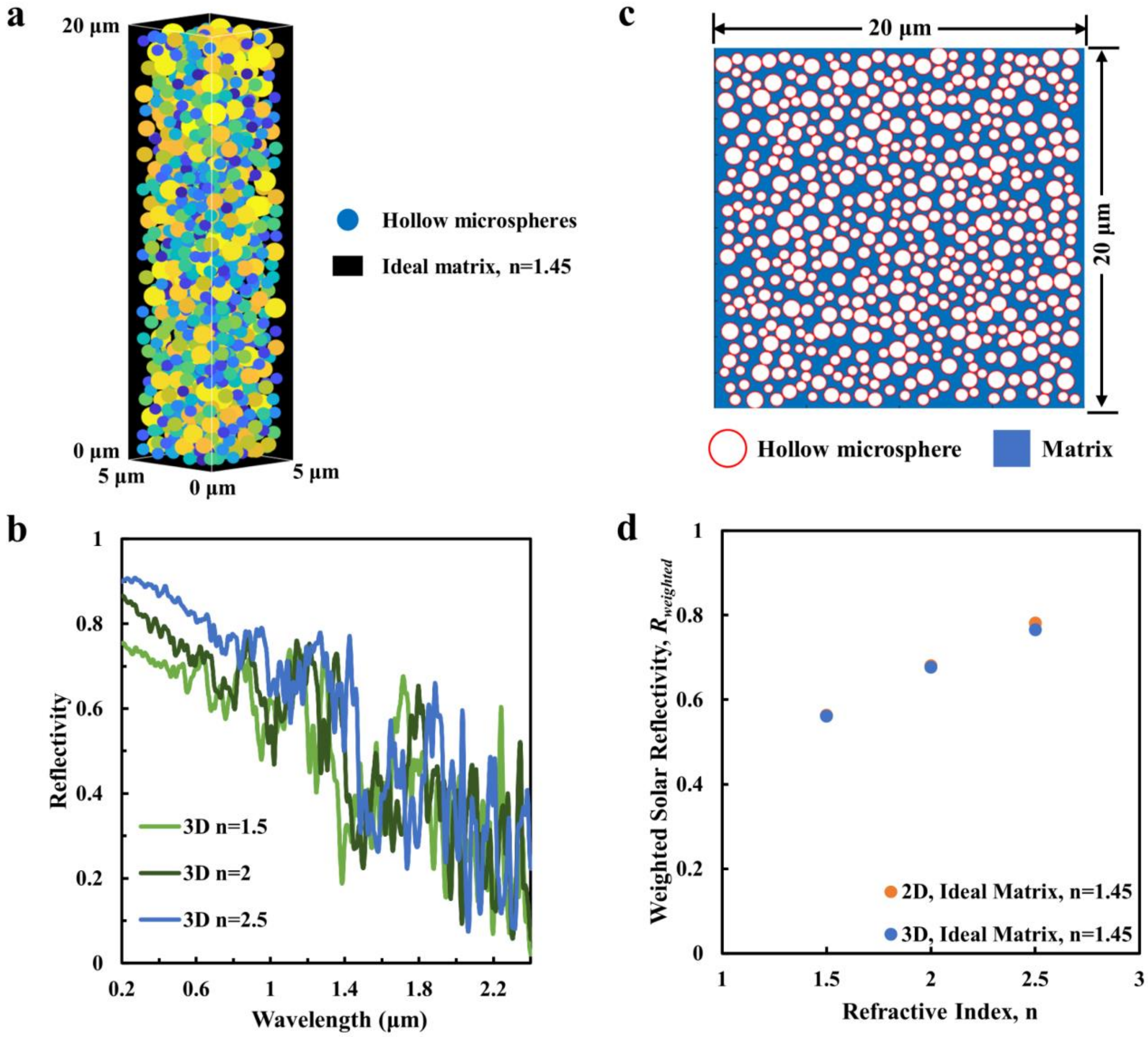

Figure 2.11 3D FDTD simulations. (a) The schematic of the 3D unit cell with a dimension of 5 μm × 5 μm × 20 μm, along with randomly distributed hollow microspheres with a diameter range of 0.5-1 μm and an inner-to-outer diameter ratio d_i/d_o of 0.9. The volume fraction of hollow microspheres is 48.25%. The ideal matrix material is assumed, with a refractive index of 1.45 and extinction coefficient of 0. Various colors have been applied to the surface of hollow microspheres, only to distinguish them from each other; (b) The

effect of refractive index (***n***) values on solar reflectivity, for ***n*** values of 1.5, 2 and 2.5 in hollow microspheres; (c) The schematic of the 2D unit cell with a dimension of 20 μm × 20 μm, and an areal fraction of 48.26%; (d) The weighted solar reflectivity $\boldsymbol{R_{weighted}}$ in 2D and 3D FDTD simulations, for ***n*** values of 1.5, 2 and 2.5.

Chapter 3 Cool White Polymer Coatings based on Hollow Glass Microspheres

While some nanophotonic structures and metal-film-backed polymer composites have demonstrated substantial radiative cooling, the processing requirements, related costs, and the use of expensive metallic films are inappropriate for large-scale building applications. In this chapter, we present techno-economically viable and scalable white coatings by integrating microscale hollow glass microspheres into a polymer (polydimethylsiloxane, PDMS) binder. The combination of high solar reflectivity and infrared emissivity of white coatings based on hollow glass microspheres leads to a significant temperature reduction when coated on the surface of building materials and shows superiority compared to commercial white paints. The cool white coatings demonstrate considerable amount of cooling energy savings on common commercial and residential building models according to our building energy analysis.

3.1 Introduction

It is expected that more than 6 billion people will live in urban environments by 2050[73], and the aggressive urban infrastructure growth to accommodate larger population may result in critical side effects in energy consumption, air quality, and even human health. In particular, the annual cooling or air conditioning energy demand is forecasted to exceed ten quintillion (10^{19}) joules by 2040[5]. and the associated carbon emissions and air pollution may play a critical role in early death, which is linked to 6.5 million premature deaths across the world in 2015[74]. On the other hand, the lack of air conditioning in old European building led to thousands of deaths estimated during the record-breaking heat wave in the summer 2019[1].

Resolving the interconnected energy, greenhouse gas emission, air quality, and human health problems will require highly innovative approaches to surface cooling and advanced materials for use in urban environments. As a potential solution, engineering building surfaces[8,75] to passively control thermal radiation or the concept of radiative cooling has drawn much attention in recent years[8,76]. While the incoming solar irradiation[77] within the wavelength (λ) range of 0.3 μm to 2.5 μm heats up the surface, radiation from the object to the cold outer space through the atmosphere's transmission window[9] in the mid-infrared (mid-IR) wavelength range of 8 μm to 13 μm helps cool the surface. Optical coating materials for radiative cooling require a high solar reflectivity to minimize heating by the sun and a high mid-infrared (IR) emissivity to maximize thermal emission from the surface to the atmosphere and to the cold space. This novel method decreases the amount of energy required for the active cooling of large-area outdoor buildings which cannot avoid intensive exposure to solar irradiation and need to maintain a controlled thermal environment. While some nanophotonic structures including silicon (Si) or silicon dioxide (SiO_2)-based layered structures[16] have demonstrated substantial radiative cooling, the processing requirements and related costs might be inappropriate for building applications. Other approaches could include using dielectric pigments-embedded paints[11,78], but near-infrared (NIR) and ultraviolet (UV) absorption are not attractive. Polymer composites[18,79] can also achieve significant radiative cooling, but the use of expensive metallic films and complicated process may limit large-scale applications. For example, the silver-coated polymer composite[18] can cost \$2.49/m^2 or \$0.027/W while providing 93 W/m^2 cooling power. The use of simple process and inexpensive materials is necessary. Daytime radiative cooling capability has been demonstrated both experimentally and theoretically, using randomly packed SiO_2 microspheres[27], hierarchal coating designs[23,28] and hollow microspheres made of pure glass[44] or organic polymer[80], to enable more hierarchical control of the polymer coatings. For large-scale lightweight structures, hollow glass microspheres can be considered a good substitute for solid glass microspheres considering their low density and high interface-to-volume ratio.

Here we present low-cost and scalable polymer coatings by integrating a controlled volume concentration of hollow glass microspheres within a polymer (polydimethylsiloxane, PDMS) matrix and show a significant radiative cooling capability for buildings. Our polymer coating achieves a radiative cooling performance that is comparable or better compared to previously reported designs that required costly materials or processes[16,18,79]. We then use a building energy analysis tool to estimate the impact of cool white polymer coatings on building energy savings, and associated cost savings and carbon dioxide (CO_2) emission savings. We perform techno-economic evaluations in terms of cost per area and cost per cooling power for our polymer coating material, commercial white paints, and the state-of-the-art polymer coating solution.

3.2 Preparation, Characterization and Density Analysis

We prepared polymer coatings (**Fig. 3.1a**) with a varying volume concentration (ϕ) of 0 to 70% (denoted as 0 to 70 vol%). The volume concentration (ϕ) of hollow glass microspheres inside the polymer coating is defined as

$$\phi = \frac{V_{HGM}}{V_{PC}} \tag{3.1}$$

Where V_{HGM} is the volume of hollow glass microspheres, and V_{PC} is the volume of the polymer coating.

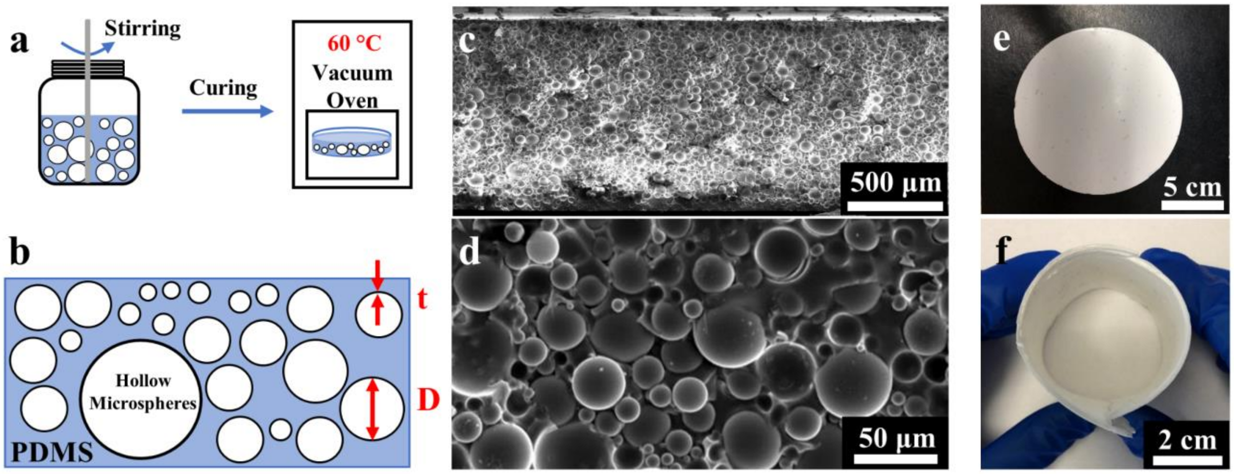

Figure 3.1 The fabrication and characterization of polymer coatings. (**a**) The schematic of the fabrication process of the polymer coatings; (**b**) The schematic of the polymer coating in which hollow glass microspheres take up certain volume concentration inside PDMS matrix. The diameters (D) of hollow glass microspheres are from 1 μm to 40 μm, with a mean value of 10 μm. The shell thicknesses (t) of hollow glass microspheres are ranging from around 0.05 μm to 2 μm, and volume concentrations of hollow glass microspheres inside the PDMS matrix are from 0 to 70% during our fabrication process; (**c**) The low-magnification and (**d**) high-magnification cross-sectional SEM image of the as-prepared 70 vol% polymer coating; (**e**) Top-down view of the circular 70 vol% polymer coating sample with a dimeter of 5.5 inches; (**f**) The rolled 70 vol% polymer coating to demonstrate the flexibility.

Fig. 3.1b shows a cross-sectional schematic of the polymer coating, in which hollow glass microspheres occupy certain ϕ, changing the film to an opaque appearance without sacrificing the robustness and lightweight attributes of pure PDMS. **Fig. 3.2a** to **3.2d** shows the Scanning Electron Microscope (SEM) images and the corresponding size analysis of hollow glass microspheres. The size measurements and analysis indicate that the diameters of hollow glass microspheres (D) range from 1 μm to over 40 μm and center at ~8 μm. The mean value of the hollow glass microspheres' diameters is around 10 μm, which is supported by size analysis of multiple SEM images in different observation locations. From the SEM observation, the shell thicknesses of hollow glass microspheres (t) are roughly from 0.05 μm to 2 μm. After being mixed with PDMS, the hollow glass microspheres distribute from 1 μm to 50 μm for over 95% microspheres and the mean value is 12 μm (**Fig. 3.2e**), as studied by nano Computed Tomography (CT) which uses X-rays to detect the cross-sections from a three-dimensional polymer coating that are later used to recreate a virtual model (**inset** in Fig. 3.2e).

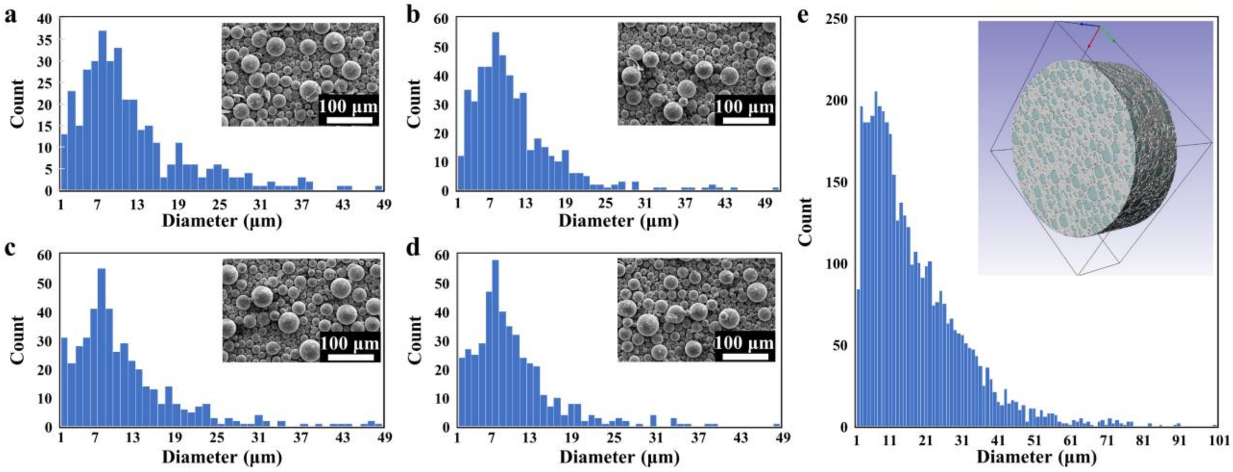

Figure 3.2 Diameter distribution analysis of hollow glass microspheres before mixed with PDMS from SEM images and after mixed with PDMS from nano CT analysis. (**a-d**) The corresponding diameter distribution of hollow glass microspheres from top-down view SEM image in the inset. All the diameter distributions agree well, with similar diameter ranges and mean values. For all SEM images, the mean values of diameters are 10.9 μm, 9.7 μm, 10.4 μm and 9.9 μm, respectively; (**e**) The diameter distribution of the hollow glass microspheres after blended with PDMS using nano CT analysis. The inset is the three-dimensional model of the 70 vol% polymer coating rebuilt from cross-sectional images obtained from nano CT analysis.

It is also observed that the hollow glass microsphere has a very thin shell with a large air void inside, which leads to an extremely low mass density (0.460 g/cm^3, or 460 kg/m^3). As we prepare polymer coatings by integrating hollow glass microspheres within uncured PDMS – which has a higher theoretical mass density (0.965 g/cm^3, or 965 kg/m^3) – it should be noted that the larger ϕ of hollow glass microspheres in the polymer coating, the lower mass density the mixture possesses. We prepare polymer coatings with varying ϕ, ranging from 3 to 70%. As shown in **Table 3.1**, the measured mass density of the polymer coating drops from 905 kg/m^3 to 681 kg/m^3. Regarding the areal density, 3 vol% with a thickness of 330 μm results in 0.306 kg/m^2, while 70 vol% with a thickness of 1300 μm leads to 0.885 kg/m^2. The theoretical mass density (ρ) of the polymer coating in Table 3.1 can be obtained as a function of ϕ of hollow glass microspheres by

$$\rho\left(\frac{kg}{m^3}\right) = \frac{(100-\phi)}{100} * 965 + \frac{\phi}{100} * 460 \tag{3.2}$$

Volume Concentration (%)	Measured Thickness (μm)	Theoretical Density (kg/m^3)	Measured Density (kg/m^3)	Areal Density (kg/m^2)
0	330	965	927	0.306
3	330	950	905	0.299
6	340	935	892	0.303
10	300	915	881	0.264
20	260	864	855	0.222
40	380	763	845	0.321
60	740	662	810	0.599
70	1300	612	681	0.885

Table 3.1 The density information of polymer coatings with varying ϕ from 0 to 70%.

After blending with uncured PDMS, hollow glass microspheres are randomly distributed and take up a large area inside the polymer matrix, according to the cross-sectional SEM images of the 70 vol% polymer coating in **Fig. 3.1c** and **3.1d**. Since the mixture shows a paint-like format, the final shape of the polymer coating depends on the shape of the substrate. This feature can be utilized to fabricate any arbitrary shape desired, and it indicates the possibility of fabricating a large-scale polymer coating that meets the massive needs for surface radiative thermal management when combined with advanced manufacturing techniques such as blade coating. We therefore achieve the 5.5 inch-diameter circular sample preparation, as indicated in **Fig. 3.1e**. Furthermore, the polymer coating can be twisted or rolled to meet any special practical needs; even with a 70vol%, the sample demonstrates excellent flexibility **(Fig. 3.1f).** Mechanical properties can be very important for polymer coating applications with regards to reliability and stability. We observed that the stiffness and the Young's modulus of the polymer composites increase as the volume concentration of hollow glass microspheres increases, but the stretchability and the flexibility decrease.

3.3 Optical Properties of Polymer Coatings

As the volume concentration (ϕ) of hollow glass microspheres increases within a polymer matrix, the reflectivity increases selectively within the solar spectrum while remaining low in mid-IR wavelengths. We attribute the increasing solar reflectivity to increasing number of interfaces in the polymer coating and consequent increasing backscattering efficiency, which is confirmed by Ultraviolet-Visible-NIR (UV-VIS-NIR) spectroscopic measurement (λ, 0.4 μm to 2.5 μm). The mid-IR optical properties of polymer coatings with varying ϕ from 0 to 70% are characterized using a Fourier-transform infrared (FTIR) spectrometer in the mid-IR region (λ, 2.5 μm to 16 μm). We measured the diffuse reflectivity and transmissivity of polymer coatings with varying ϕ from 0 to 70% with integrating spheres which are used to account for the scattered light from the full solid angle in both UV-VIS-NIR and FTIR spectroscopic measurements[81]. For diffuse reflectivity, the polymer coating is placed on the reflection port of the integrating sphere in which all the backscattered light bounces off the integrating sphere surface several times until detected by the detector (**Fig. 3.3a** and **3.3b**). For diffuse transmissivity, the polymer coating is placed on the front port of the integrating sphere, allowing all the light transmitted through the polymer coating to be received by the detector (**Fig. 3.3c** and **3.3d**). It is noted that the average reflectivity in both the visible (λ, 0.4 μm to 0.8 μm) and NIR region (λ, 0.8 μm to 2.5 μm) gradually rises with increasing ϕ from 0 to 70%, while the diffuse transmissivity drops significantly with increasing ϕ in both regions. It is validated by the optical images of polymer coatings in **Fig. 3.3e**. As ϕ increases from 0 (left) to 70% (right), the surface changes opacity and becomes whiter. In the mid-IR region, ϕ dependence in both diffuse reflectivity and transmissivity is also observed between 2.5 μm and 6 μm, while it is not significant between 6 μm to 16 μm including the atmosphere's transmission window. Using the measured diffuse reflectivity and transmissivity, the emissivity of polymer coatings with varying ϕ in solar region and mid-IR region is calculated and plotted in **Fig. 3.4a**, based on the sum of transmissivity, reflectivity and absorptivity being unity and assumption that emissivity is considered equal to absorptivity under Kirchhoff's Law[82]. In **Fig. 3.4b**, the measured UV-VIS-NIR reflectivity of 70 vol% polymer coating with different thicknesses from 500 μm to 2500 μm are plotted. It can be seen that a thickness of 500 μm leads to a fairly high reflectivity while the reflectivity varies little when the thickness is higher than 750 μm. The high solar reflectivity (0.92) in the 70 vol% polymer coating is comparable to or exceeds many previous reported values[16,18,28,79], which enables strong reflection of sunlight for possible radiative cooling applications and eliminates the need for using metallic reflectors reported in some previous designs[16,18]. We attribute the broadband high reflectivity to the broad distribution of the hollow glass microsphere diameter ranging from 1 μm to over 40 μm with the average of 8 μm. Based on our understanding supported by the Mie Scattering theory, we can expect that far smaller or larger hollow glass microspheres won't provide a high reflectivity in the solar wavelengths and that hollow glass microspheres with a uniform size distribution may not provide a broadband reflectivity, which is essential for solar reflection and radiative cooling.

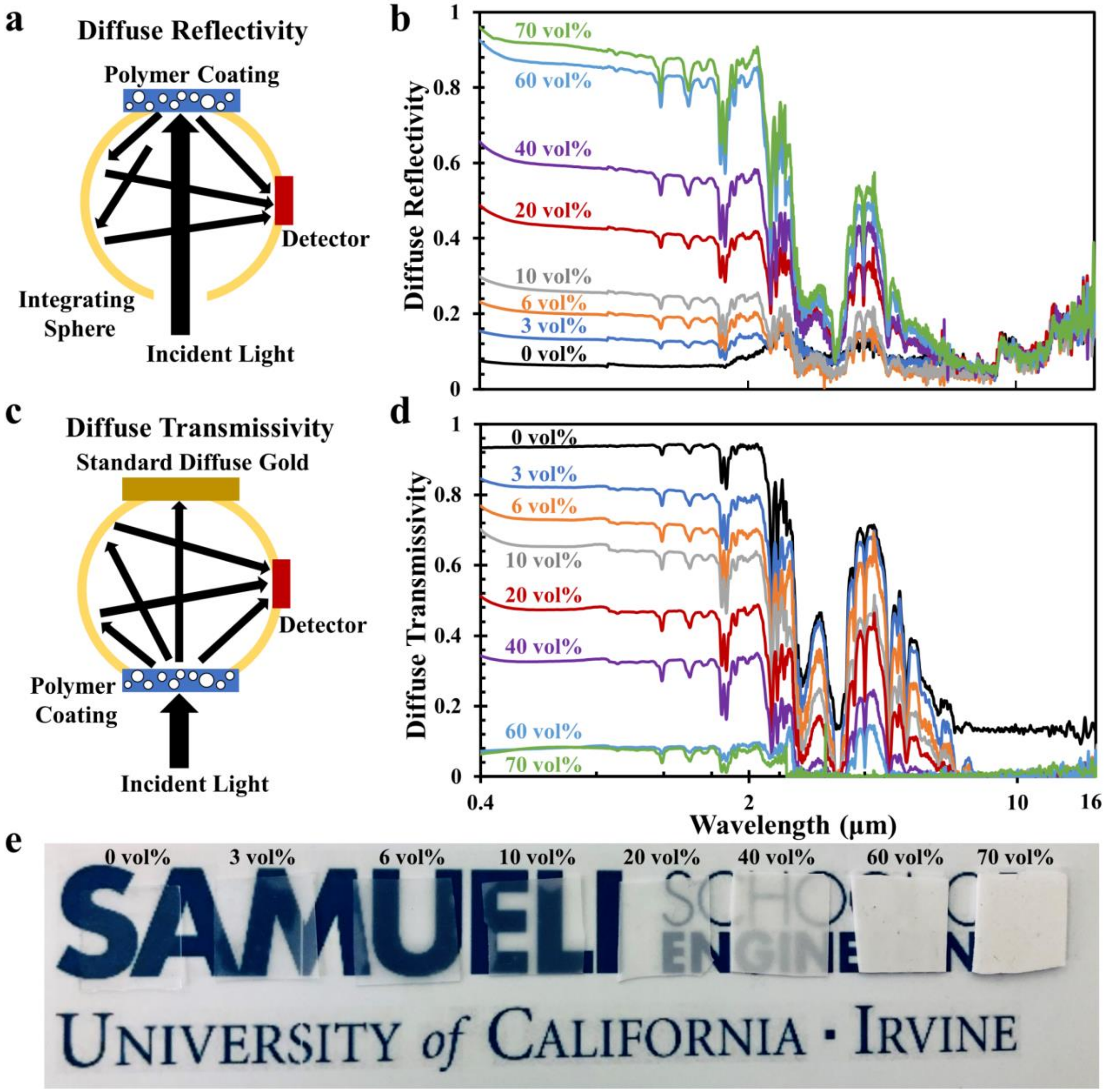

Figure 3.3 The measured diffuse reflectivity and transmissivity of the polymer coatings with varying ϕ for wavelength from 0.4 μm to 16 μm. (**a-b**) Diffuse reflectivity and (**c-d**) transmissivity of the polymer

coatings with ϕ from 0 to 70% in the wavelength range of 0.4 μm to 16 μm. An integrating sphere is used to account for the scattered light from the full solid angle in the measurement. For (a) diffuse reflectivity, the polymer coating is placed on the reflection port of the integrating sphere in which all the backscattered light bounces off the integrating sphere surface several times until detected by the detector. For (c) diffuse transmissivity, the polymer coating is placed on the front port of the integrating sphere, allowing all the light transmitted through the polymer coating to be received by the detector; (**e**) Optical images of polymer coatings with increasing ϕ of glass bubbles from 0 vol% (left) to 70 vol% (right).

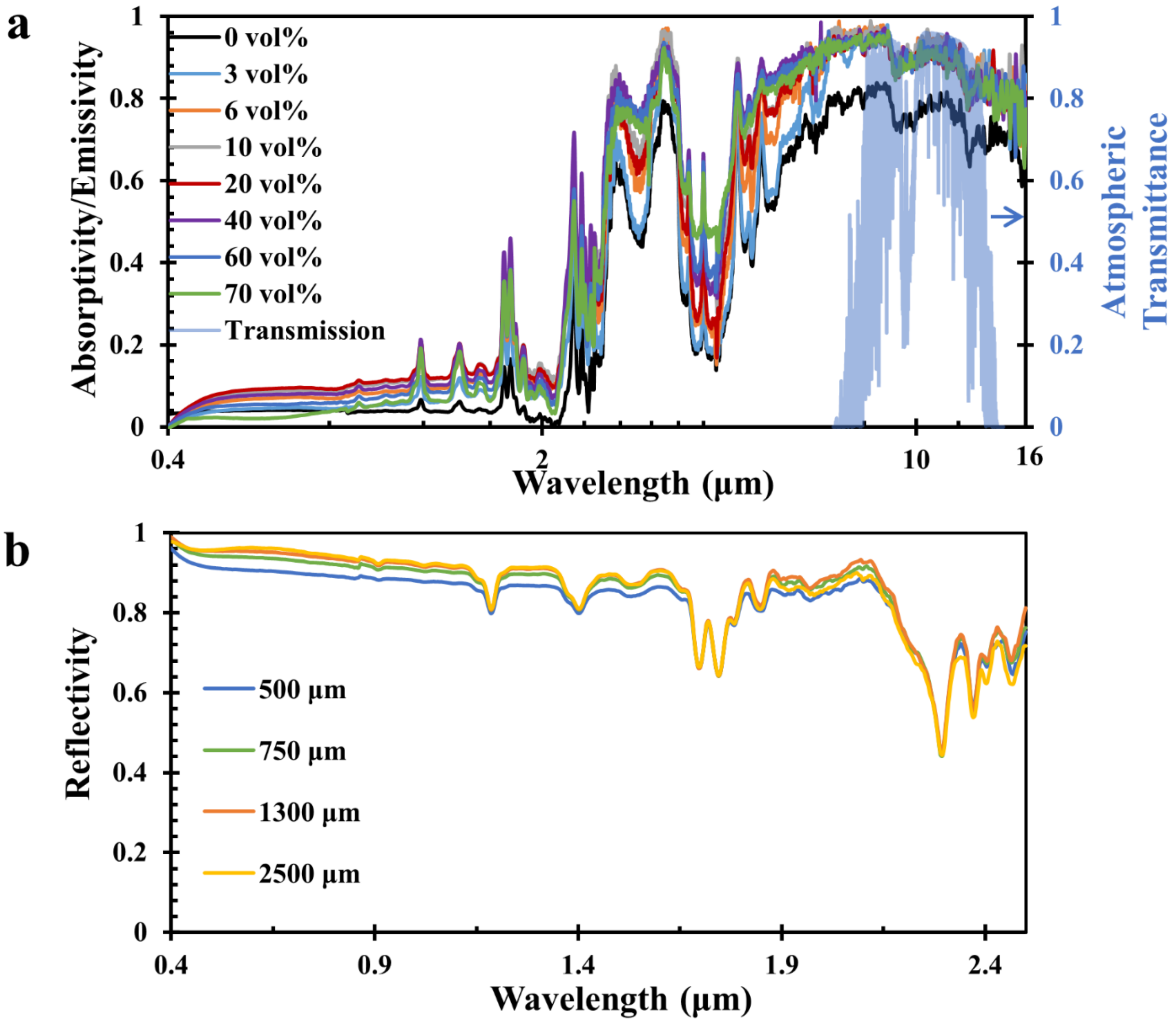

Figure 3.4 The optical properties of polymer coatings with varying ϕ from 0 to 70%. (**a**) The emissivity of polymer coatings with varying ϕ from 0 to 70% in the wavelength range from 0.4 μm to 16 μm. The

emissivity is calculated using E=1-R-T and measured values of diffuse reflectivity and transmissivity presented in Fig. 2. The as-called atmospheric window is added for reference; (**b**) The measured UV-VIS-NIR reflectivity of 70 vol% polymer coating with different thicknesses from 500 μm to 2500 μm.

Apart from diffuse reflectivity, we also measured specular reflectivity for polymer coatings with varying ϕ and determine the refractive index values n(λ) and k(λ) using measured specular reflectivity and transmissivity values from the following expression[83]:

$$\mathrm{n}(\lambda) = \left[\frac{4r}{(r-1)^2} - k^2\right]^{0.5} - \frac{r+1}{r-1} \tag{3.3}$$

$$\mathrm{k}(\lambda) = \frac{\alpha\lambda}{4\pi} \tag{3.4}$$

Where α is the absorption coefficient and defined as $\alpha = \frac{1}{d}\ln\left(\frac{1}{t}\right)$. Equation (3) and (4) clearly indicate that specular reflectivity (r) and diffuse transmissivity (t) are required as input parameters, but the values of reflectivity (R) and transmissivity (T) directly obtained from the spectrometer need to be corrected before incorporating them to calculate the optical parameters because some losses at the air-sample interfaces generally come into picture[83,84]. Using corrections stated elsewhere, r and t are related to R and T using equations (5) and (6) below[84]:

$$\mathrm{r} = \frac{2R}{1 + t^2 + \sqrt{(1+t^2)^2 - 4t^2R(2-R)}} \tag{3.5}$$

$$\mathrm{t} = \frac{2T}{(1-r)^2 + \sqrt{(1-r)^4 - 4T^2r^2}} \tag{3.6}$$

The values of r and t are obtained by solving the equations through an iterative process until the value of r and t can repeat itself. **Fig. 3.5a** shows the specular reflectivity as a function of wavelength from 0.4 μm to 0.8 μm for polymer coatings with varying ϕ. For specular reflectivity measurements, the incident beam angle and detector angle are set to 6° and 12°, respectively, as the **inset** in Fig. 3.5a shows. It is observed that specular reflectivity increases gradually with increasing ϕ, which agrees with what we found in diffuse reflectivity measurements but with smaller increments. We observe some noise in the measured values of specular reflectivity in the visible region due to the inherent uncertainty of the spectrometer. Thus, the average specular reflectivity between 0.4 μm to 0.8 μm as a function of volume concentration ϕ is plotted in **Fig. 3.5b** and it increases from 0.018 to 0.026 for increasing ϕ from 0 to 70%. The values of refractive index $n(\lambda)$ and $k(\lambda)$ as a function of wavelength has been determined using equation (3.3) to (3.6). The calculated n and k values are functions of wavelength possibly because the refractive index of two components, PDMS and SiO_2, are both functions of wavelength. Similar to both the specular reflectivity and the diffuse reflectivity, $n(\lambda)$ and $k(\lambda)$ both increase with increasing ϕ. Average values of $n(\lambda)$ and $k(\lambda)$ from 0.4 μm to 0.8 μm for varying ϕ are plotted in **Fig. 3.5c** and **3.5d**. The average n and k values increase from 1.21 to 1.38 and from 9.576×10^{-6} to 3.655×10^{-4} respectively, with increasing ϕ from 0 to 70%. The calculated refractive index values indicate how light propagates through the polymer coatings with varying ϕ. With a larger refractive index value for larger ϕ, the light travels slower, which correspondingly causes more changes in the direction of light propagation within polymer coatings. This leads to increased diffuse reflectivity or specular reflectivity and decreased diffuse transmissivity for polymer coatings with increasing ϕ as we report. We use the computation based on rigorous coupled-wave analysis (RCWA)[53,54,85] to verify the ϕ dependence on optical properties of polymer coatings and the computation results agree well with the measured optical properties of the polymer coatings.

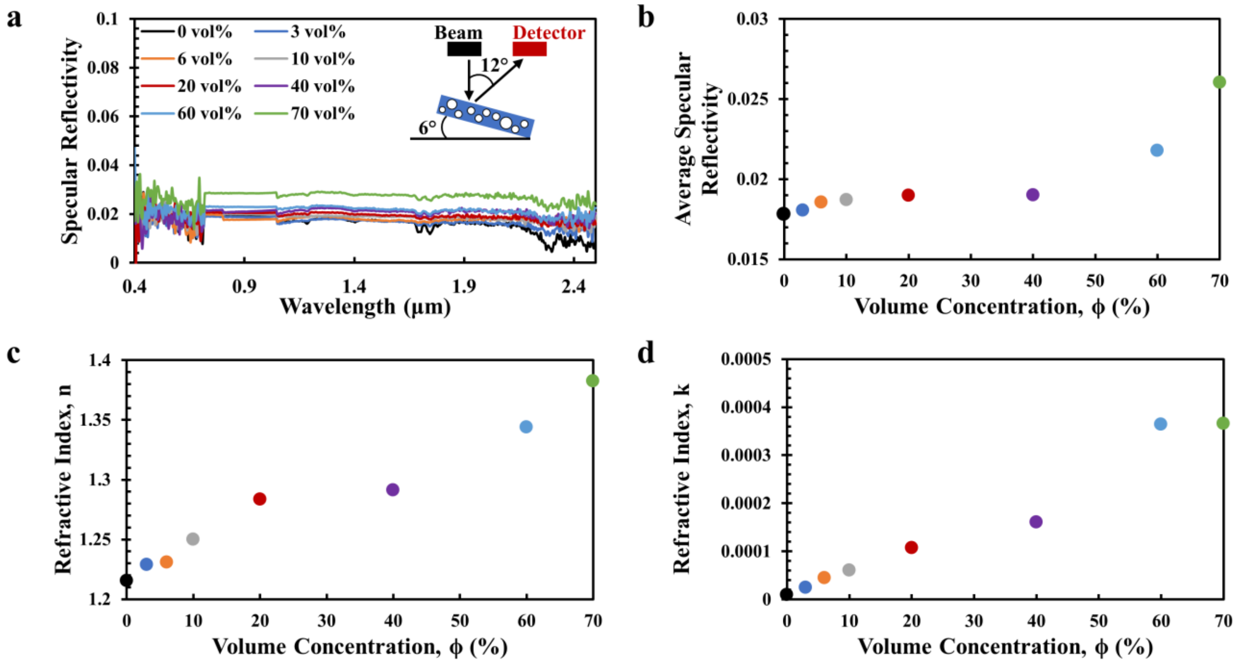

Figure 3.5 Refractive index values of polymer coatings with varying ϕ. (**a**) Specular reflectivity of polymer coatings with varying ϕ from 0 to 70% in the solar region and (**b**) the corresponding average specular reflectivity value from 0.4 μm to 0.8 μm. The inset in A shows that specular reflectivity is measured with an incident angle at 6° and detector angle at 12°; The average value of (**c**) real part, n(λ) and (**d**) imaginary part, k (λ) of refractive index from 0.4 μm to 0.8 μm for polymer coatings with varying ϕ from 0 to 70%. n(λ) and k(λ) are converted from measured reflectivity and transmissivity values from 0.4 μm to 2.5 μm for polymer coatings with varying ϕ from 0 to 70%.

3.4 Thermal Analysis and Outdoor Temperature Measurement

The combination of high solar reflectivity and mid-IR emissivity we have obtained from the spectroscopy is promising for radiative cooling applications. The measured values of 70 vol% polymer coating are used in the temperature predictions based on thermal analysis in the ambient environment (detailed in **Fig. 3.6a**). The prediction in **Fig. 3.7a** shows that the concrete temperature with 70 vol% polymer coating is 5.3 °C lower than the ambient air at noon due to the unique combination of high solar reflectivity and mid-IR emissivity, assuming a steady ambient environment, a representation daily weather data in the summer[86], a constant conductive and convective heat transfer coefficient h=10 W/m^{2}K and a peak solar irradiance[87] of 875 W/m^2 at 12 pm (shown in Fig. 3.7a). It is noticed that the bare concrete block without 70 vol% polymer coating is predicted to be 35°C higher than the ambient air at noon. In terms of the relation between temperature and heat flux (**Fig. 3.7b**), the prediction shows that the maximum temperature drop can reach 5.3°C, while the cooling power at the peak solar irradiance is 78.2 W/m^2, which is around half of the theoretical maximum cooling power (147.9 W/m^2) as the prediction indicates. This remarkable cooling performance is comparable to many previously reported works whose average daytime cooling power varies from 40 W/m^2 to 96 W/m^2, or from 42 W/m^2 to 109 W/m^2 [16,18,23,35,79] when we evaluate these radiative cooling materials under same cooling power prediction conditions as our polymer coating.

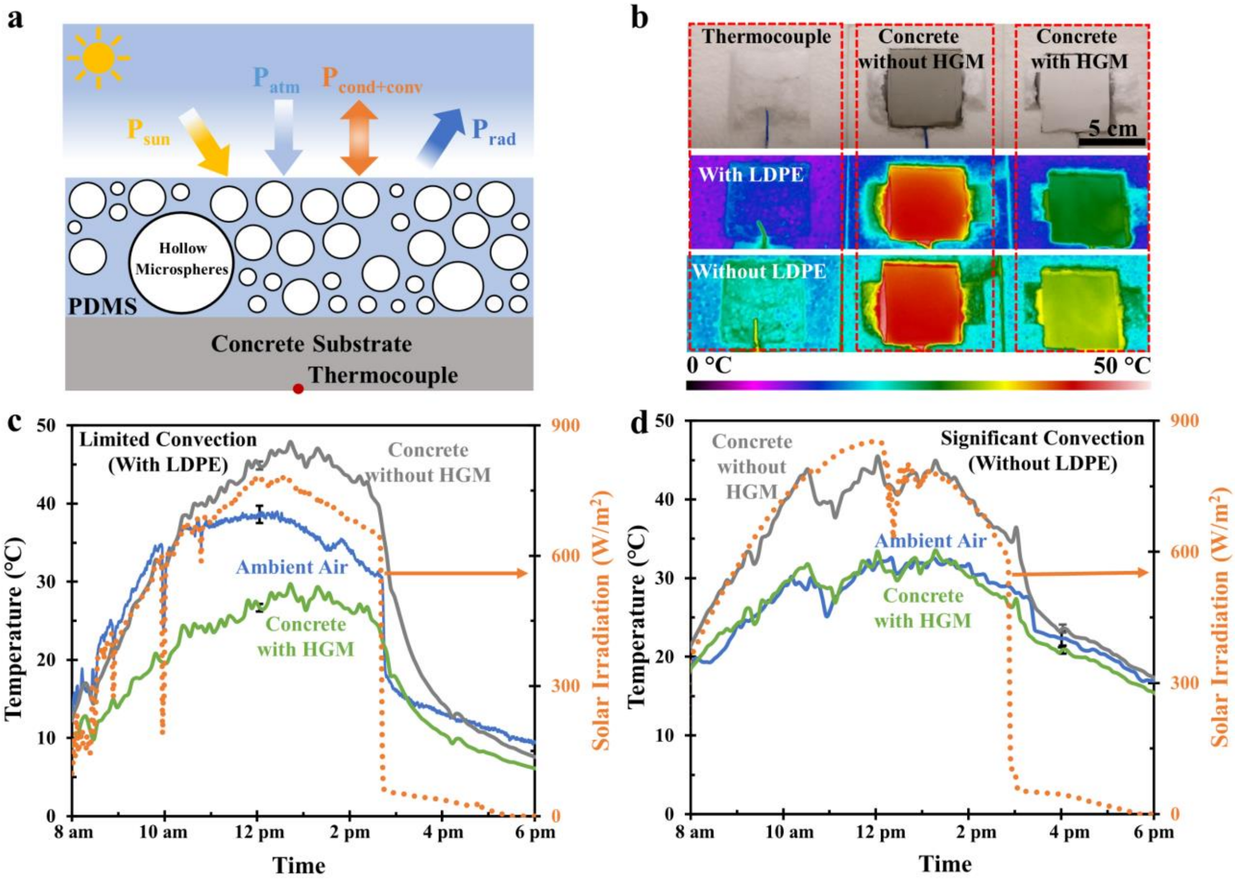

Figure 3.6 Thermal performance of 70 vol% polymer coating. (**a**) The schematic of the thermal analysis of a polymer coating in the ambient environment. The thermocouple in the schematic shows the location of thermocouples measuring sample temperatures during the measurements; (**b**) The optical images and the corresponding IR image of the temperature measurement apparatus with and without a 25 μm-thick layer of LDPE film as the wind shield. In the optical and IR image, the left is the thermocouple used for measuring ambient air temperature. The middle is the concrete block of 2 inch × 2 inch × 0.5 inch with a same-area 2mm-thick PDMS on top (denoted as 'concrete without glass bubble (GB)') and the right is the concrete block with a same-area 2 mm-thick 70 vol% polymer coating on top (denoted as 'concrete with GB'); Rooftop temperature measurement data from 8 am to 6 pm for ambient air (blue), concrete without GB (grey) and concrete block with GB (green) (**c**) with the LDPE film covered on the top as the wind-shield

and (**d**) without the LDPE film during the measurement. The temperature data in c and d was measured on Feb. 19th, 2020, and Mar. 3rd, 2020, respectively.

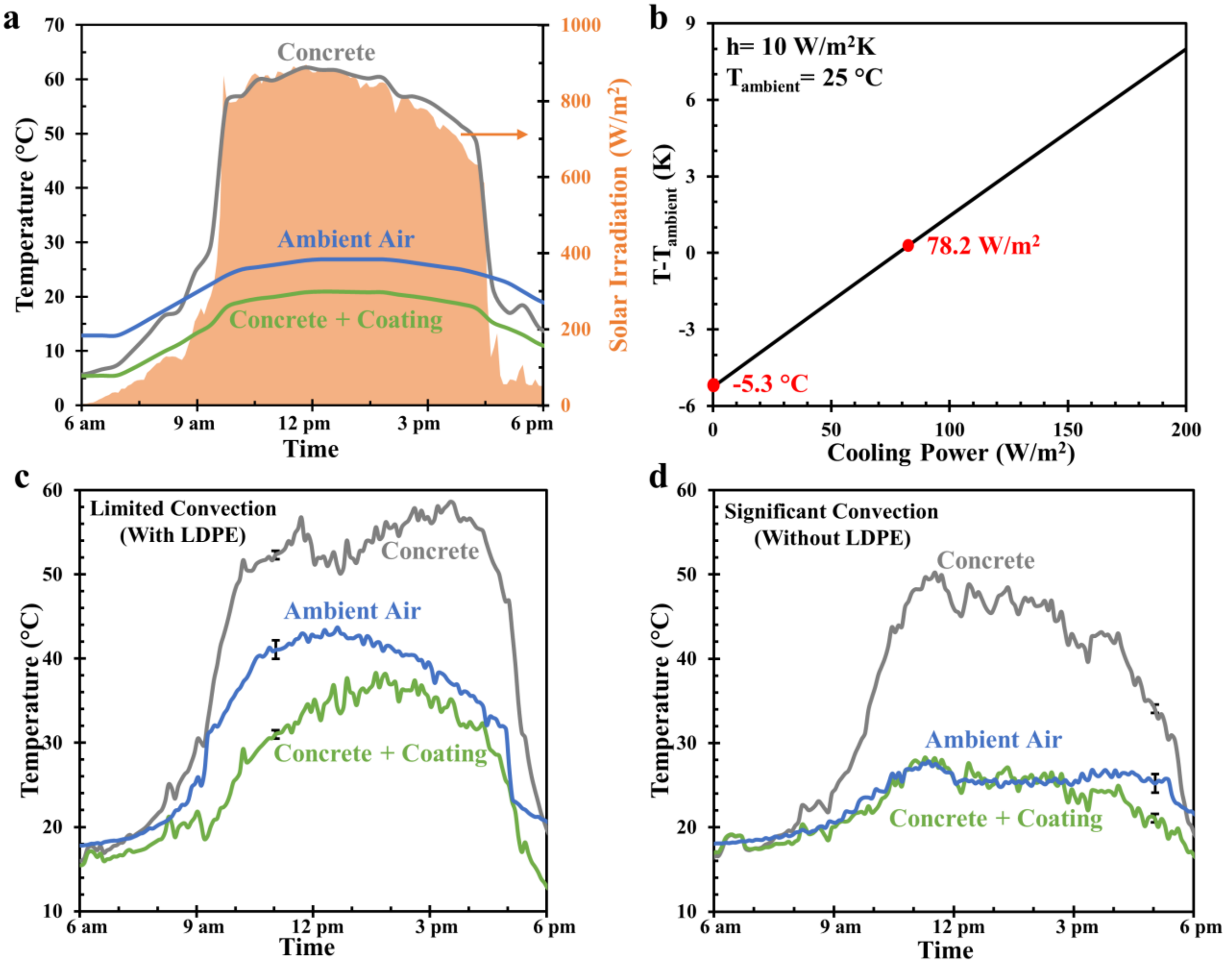

Figure 3.7 Thermal performance of the 70 vol% polymer coating. (**a**) The predicted temperatures of the ambient air (blue), bare concrete block (grey) and concrete block with 70 vol% polymer coating on top (green) from 6 am to 6 pm, assuming a steady ambient environment, a representative weather condition, a constant conductive and convective heat transfer coefficient h=10 W/m^{2}K and a peak solar irradiance of 532 W/m^2 at 12 pm in Southern California; (**b**) Temperature difference between surface of concrete block with 70 vol% polymer coating and ambient air as a function of cooling power. For this temperature prediction, the calculated emissivity values based on measured reflectivity and transmissivity data from spectroscopy are used. A constant conductive and convective heat transfer coefficient h=10 W/m^{2}K and an

ambient air temperature of 25°C are assumed; Rooftop temperature measurement data from 6 am to 6 pm for ambient air (blue), concrete block (grey) and concrete block with 70 vol% polymer coating (green) (**c**) with the LDPE film covered on the top as the windshield and (**d**) without the LDPE film during the measurement. The temperature data in c and d was measured on July 11th, 2019, and June 28th, 2019, respectively.

We conduct the temperature measurements to demonstrate the surface cooling capability of the 70 vol% polymer coating, as shown in **Fig. 3.6b**. A 2 inch × 2 inch × 0.5 inch concrete block with a same-area 2-mm thick PDMS on top (denoted as 'concrete without GB' in Fig. 3.6b, 'GB' means hollow glass microspheres) and another same-size concrete block with a 2 mm-thick 70 vol% polymer coating on top surface (denoted as 'concrete with GB' in Fig. 3.6b) are used for a comparative study. The samples are placed inside the insulation Styrofoam with a low thermal conductivity of 0.063 W/(m·K)[88] to minimize conductive heat loss. The temperature data in **Fig. 3.6c** and **3.6d** is obtained using the IR camera with an uncertainty of ±0.5 °C and thermocouples with an uncertainty of ±1.1°C. The solar irradiation corresponding to the right y-axis is measured using a pyranometer for reference. With a 2 mm-thick layer of 70 vol% polymer coating covered on top surface, the concrete block exhibits a sub-ambient cooling of 9.6 °C at peak solar irradiance of 780 W/m^2 when a 25 µm-thick low-density-polyethylene (LDPE) film lies above the box as an IR-transparent wind shield (Fig. 3.5c). The temperature reduction is also apparent in the IR image at 1 pm, in which the concrete with 70 vol% polymer coating on the right cools around 20 °C than concrete block with PDMS in the middle. We've confirmed that the temperatures of the bare concrete sample and the PDMS coated concrete sample with no hollow glass microspheres are nearly identical (**Fig. 3.8**). We also conduct the outdoor temperature measurement without the LDPE film to simulate the realistic exposed surfaces of buildings (Fig. 3.6d). Compared with concrete with PDMS, the concrete block with the 70 vol% polymer coating shows a comparable temperature as ambient air. This phenomenon is also apparent from the IR image at 12 pm. The abrupt drops of measured solar irradiance at 10 am and 12 pm is possibly due to the clouds in the sky, while the drop at approximately 3 pm is due to the shadows cast on the pyranometer. The mismatch between temperature prediction in Fig. 3.7a and temperature measurements in Fig. 3.6c and 3.6d is due to that the convective and conductive heat transfer coefficient h is always changing during the whole measurement slot and it deviates from the constant value we use in the temperature prediction. Considering concrete is a widely used building material, the outdoor temperature measurements both with and without wind-shielding LDPE film exemplify the surface radiative cooling capability of the 70 vol% polymer coating, thus enabling substantial energy savings and large-scale realistic application in surface radiative thermal management for buildings, spacecraft, or wearables.

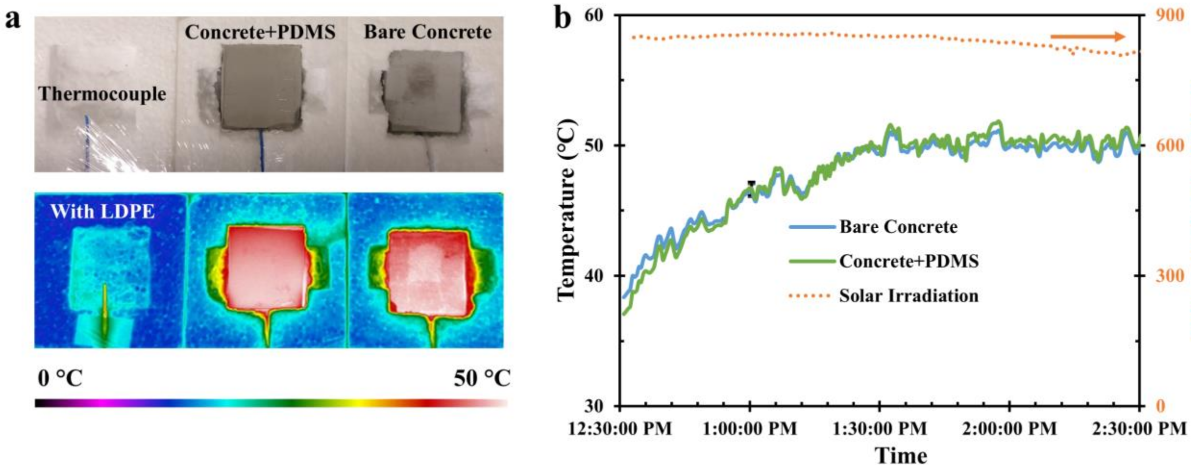

Figure 3.8 Temperature comparison between bare concrete and concrete with PDMS. (**a**) The optical images and the corresponding IR image of the temperature measurement apparatus with a 25 μm-thick layer of LDPE film as the wind shield. In the optical and IR image, the left is the thermocouple used for measuring ambient air temperature. The middle is the concrete block of 2 inch × 2 inch × 0.5 inch with a same-area

2mm-thick PDMS on top and the right is the bare concrete block; (**b**) Temperature measurement data from 12:30 pm to 14:30 pm for bare concrete and concrete with PDMS, with a LDPE film covered on the top as the windshield during the measurement. The temperature data was obtained on Mar. 8th, 2020.

3.5 Building Energy Consumption Analysis

The surface cooling capability of the 70 vol% polymer coating when applied onto the surfaces of generally used building materials motivates us to seek out the potential energy savings of using such polymer coatings on the exterior surfaces of commercial and residential buildings. Among different building types and representative cities in various climate zones provided by the US Department of Energy (DOE) commercial reference building database[89] and The American Society of Heating, Refrigerating and Air-Conditioning Engineers (ASHRAE) Standard 90.1 prototype building database[90], seven different building models (New Construction after 2004) located in Los Angeles are selected, representing common commercial and residential buildings and providing comparison within the same category. Los Angeles is selected because it is a representative city with a hot climate and large population. We use A, B, C, D, E, F and G to denote highrise apartment, midrise apartment, large hotel, small hotel, large office, medium office, and small office, respectively. Detailed dimensional information of these building models is listed in **Table 3.2** and three-dimensional models are provided in **Fig. 3.9a**. The total exterior surface area for seven building models varies much. The largest surface area of 15747 m^2 is provided by the large office model, while small office model only has a surface area of 880 m^2, which is smallest among seven different models. We use the building energy simulation software EnergyPlus developed by DOE to solve the governing heat balance equations with an hourly time step manner over a whole year. The simulation assumes that the internal air temperature is set to 24 °C and the external air temperature are determined by hourly Typical Meteorological Year

(TMY3) weather data[91], which are used as the input boundary conditions for the governing equations. The building models are directly used to establish the reference energy consumption patterns and then modified by adding a 2 mm-thick layer of 70 vol% polymer coating onto the exterior surfaces of roofs and walls to generate the modified energy consumption patterns. Detailed material properties of 70 vol% polymer coating are specified in **Table 3.3**.

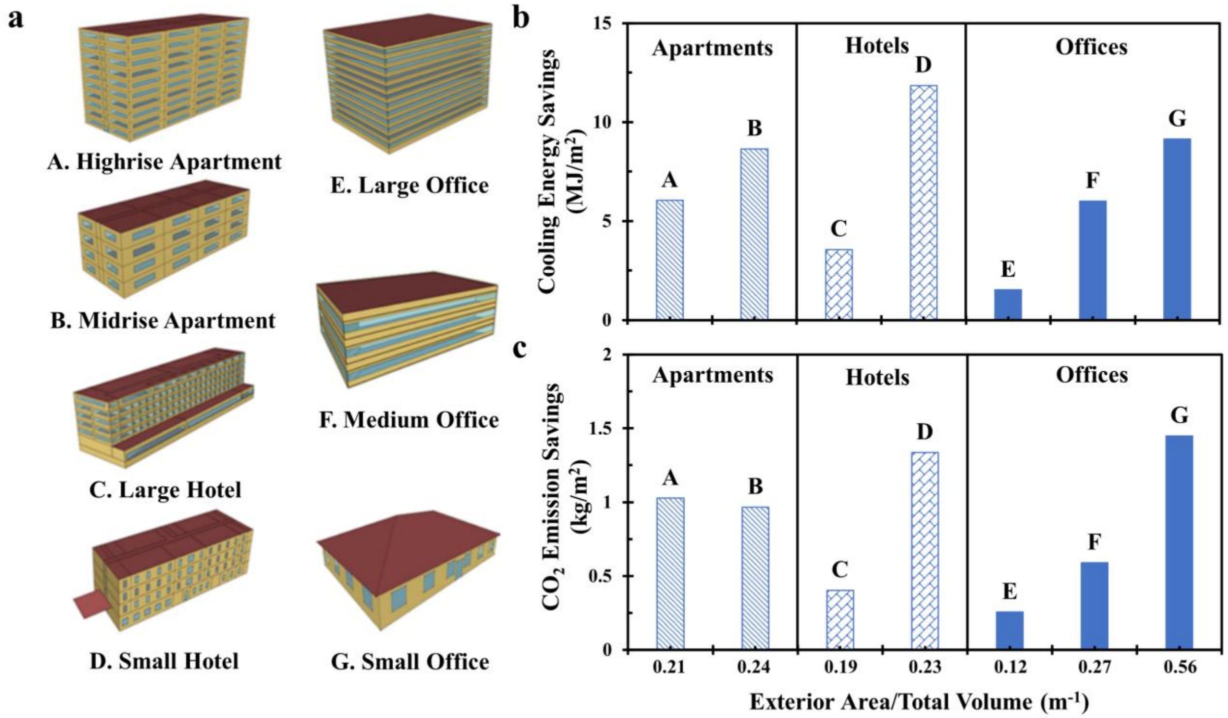

Figure 3.9 Annual cooling energy savings and CO_2 emission savings by modifying the reference building types with 70 vol% polymer coating. Here, Department of Energy (DOE) developed reference building models and ASHRAE Standard 90.1 prototype building models (New Construction after 2004) including highrise apartment (A), midrise apartment (B), large hotel (C), small hotel (D), large office (E), medium office (F) and small office (G) located in Los Angeles are used for the energy consumption analysis. The building structures are modified by adding a 2 mm-thick layer of 70 vol% polymer coating for roofing and siding on the exterior surfaces. (**a**) 3D models of the building models from highrise apartment (A) to small office (G); (**b**) Annual cooling energy savings per area for different building types, showing that building

types with larger ratio of exterior area over total volume saves more cooling energy per area per year; (**c**) Annual CO_2 emission savings per area associated with electricity consumption reduction for different building types.

Building Types	Exterior Surface Area (m^2)	Total Volume (m^3)	Exterior Area/Total Volume (m^{-1})	Number of Floors
Highrise Apartment	4536.49	21517.16	0.21	9
Midrise Apartment	2325.66	9553.61	0.24	4
Large Hotel	6538.43	35184.77	0.19	6
Small Hotel	2676.8	11447.42	0.23	4
Large Office	15747.01	126016.37	0.12	12
Medium Office	3638.4	13667.13	0.27	3
Small Office	880.27	1559.03	0.56	1

Table 3.2 Dimensional information of seven different types from US Department of Energy (DOE) Commercial Reference Building Database and ASHRAE Standard 90.1 Prototype Building Database (New Construction after 2004).

Property	70 vol% Polymer Coating	White Paint
Thickness (mm)	2	0.15
Conductivity (W/m·K)	0.3	0.57
Density (kg/m^3)	681	1162
Thermal Absorptance	0.85	0.85
Solar Absorptance	0.16	0.45
Visible Absorptance	0.08	0.14

Table 3.3 Detailed input material properties of the 70 vol% polymer coating and white paint used in the building energy consumption analysis.

We calculated the annual cooling energy savings for seven selected building types from A to G located in Los Angeles via comparing annual cooling energy generated by reference building types and modified building types (**Fig. 3.10a**). To eliminate the influence of different building area and surface area for different building models, the annual cooling energy savings per area are shown and compared in **Fig. 3.9b**. Seven building types are classified into three categories: apartments, hotels, and offices. We use the ratio of exterior surface area (including roofing area and siding area) over total volume of the building models as the x-axis in Fig. 3.9. We find that annual cooling energy savings of the modified building models ranges from 1.52 MJ/m^2 to 11.85 MJ/m^2 (0.42 kWh/m^2 to 3.29 kWh/m^2). It is also noticed that a lower-rise apartment, hotel, or office has a larger ratio of exterior area over total volume and saves more annual cooling energy per area or has a larger reduction in annual cooling energy when 70 vol% polymer coating is covered on the exterior surface. For instance, compared with highrise apartment with 9 floors and a ratio of 0.21 m^{-1}, the midrise apartment with 4 floors has a higher ratio (0.24 m^{-1}) of exterior area over total volume and saves 8.6 MJ/m^2 cooling energy per year, which is 2.5 MJ/m^2 higher than annual cooling energy savings of highrise apartment. The polymer-coating-modified midrise apartment saves 27.5% of annual cooling energy compared to reference midrise apartment, while polymer-coating-modified highrise apartment saves 19.7% annual cooling energy compared to reference one. The same relationship is found between large hotel and small hotel, as well as large, medium, and small offices. Besides annual cooling energy savings, we also carry out the analysis in terms of annual heating energy, electricity consumption and total energy. Total energy includes heating energy and electricity consumption, while electricity consumption consists of cooling energy, lightning, equipment electricity consumption, fan energy and refrigeration, etc. **Fig. 3.10b** to **3.10d** summarize the annual heating energy, annual electricity consumption and annual total energy for both reference and modified building models. It is observed that annual heating energy is increased for all building types possibly because the polymer coating on the exterior surface lower the indoor air temperature during cold days[35]. As for the annual electricity consumption and annual total energy, all seven building types exhibit a slight reduction despite the gained annual heating energy. Annual CO_2 emission savings associated with annual electricity consumption reduction for seven 70 vol%-polymer-coating-modified building models are also estimated and presented in **Fig. 3.9c**. We find that the annual CO_2 emission savings per area ranges from 0.26-1.45 kg/m^2, showing the excellent promise in reducing the greenhouse gas emission. Energy analysis in other locations such as Phoenix, Seattle or Chicago are also conducted and the annual cooling energy savings increase with a hotter and dryer climate, with the same input material properties of 70 vol% polymer coating specified in Table 3.3 and local TMY3 weather conditions. The building energy savings analysis exemplifies the significant cooling energy savings for common commercial and residential buildings, especially for low-rise buildings with a larger ratio of exterior area over total volume.

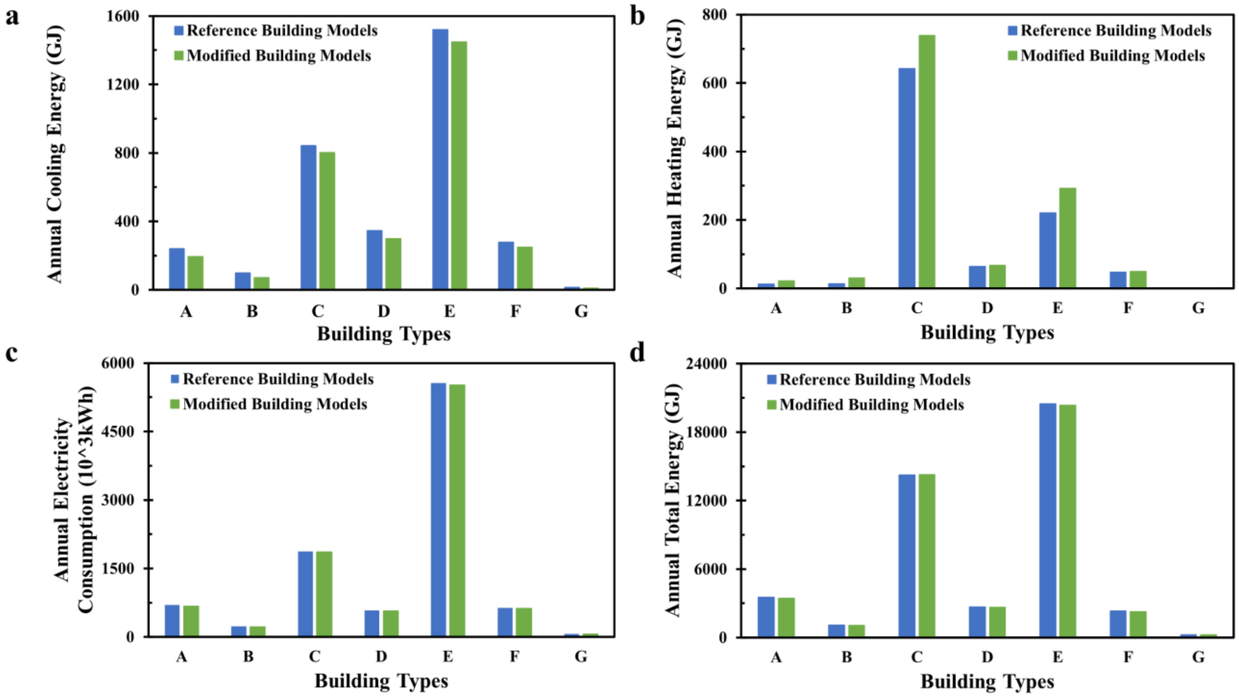

Figure 3.10 Annual building energy consumption change after we modify the DOE developed reference building types via adding a 2 mm-thick 70 vol% polymer coating for roofing and siding on the exterior surfaces. Here A, B, C, D, E, F and G denote highrise apartment, midrise apartment, large hotel, small hotel, large office, medium office and small office, respectively. Annual (**a**) cooling energy, (**b**) heating energy, (**c**) electricity consumption and (**d**) total energy for reference building types and modified building types with 70 vol% polymer coating. Total energy includes electricity consumption, while electricity consumption includes cooling energy, lightning, equipment electricity consumption, fan energy and refrigeration, etc.

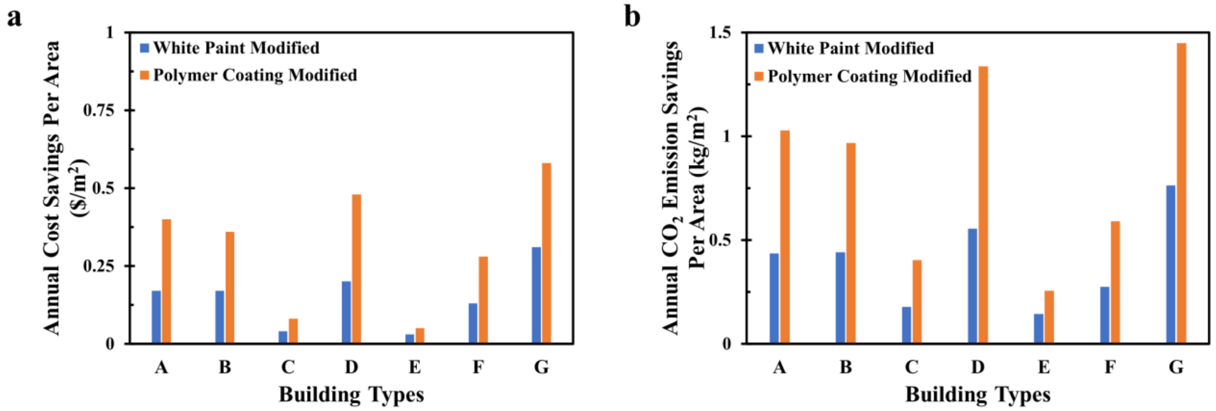

Figure 3.11 Annual cost savings and CO_2 emission savings via commercial white paint modification and 70 vol% polymer coating modification. Here A, B, C, D, E, F and G denote highrise apartment, midrise apartment, large hotel, small hotel, large office, medium office and small office, respectively. (**a**) Annual cost savings and (**b**) annual CO_2 emission savings for white paint modified building types and polymer coating modified building types.

Our cool white polymer coating exhibits great advantages over existing benchmarked approaches such as commercial white paints regarding building cost savings, greenhouse gas emission savings and material costs. Our analysis of representative buildings in Los Angeles shows that our cool white polymer coating will lead to annual cost savings of \$0.05–\$0.58/m^2 (**Fig. 3.11a**), while commercial white paints provide savings of \$0.03–\$0.31/m^2, with detailed input material properties of commercial white paints[16,23] specified in Table 3.3. For the annual CO_2 emission savings, our analysis predicts our cool white polymer coating to save 0.26-1.45 kg/m^2 (Fig. 3.10c), while commercial white paints are expected to save 0.14-0.76 kg/m^2 (**Fig. 3.11b).** The large NIR reflectivity of 0.82 and UV-resistant property (**Fig. 3.12**) make it more attractive for building applications compared to commercial white paints. The advantages of the polymer coating over white paints pave the way for potential applications in surface radiative cooling for buildings and spacecraft since they both suffer from heavy UV irradiation and UV rays damage the modern buildings gradually as reported before[92]. Additionally, it is noted that PDMS is not the only choice for matrix material. Our polymer coating system is compatible with a wide variety of polymers that have similar optical properties such as poly(methyl methacrylate)[93] and poly(vinylidene fluoride-co-hexafluoro propene)[78] (**Fig. 3.13**). In terms of techno-economic evaluation, cost per square meter or cost per cooling power is an important factor to determine whether the solution is cost-effective for realistic applications. Based on the representative bulking price on market and a thickness of 500 μm, our techno-economic analysis presents our cool white polymer coating to be very attractive in terms of \$0.39/m^2 and \$0.005/W compared to commercial white paints[11], which have \$0.48/m^2 and \$0.012/W, or even more superior compared to the state-of-the-art radiative cooling material[18] with \$2.49/m^2 and \$0.027/W in cost.

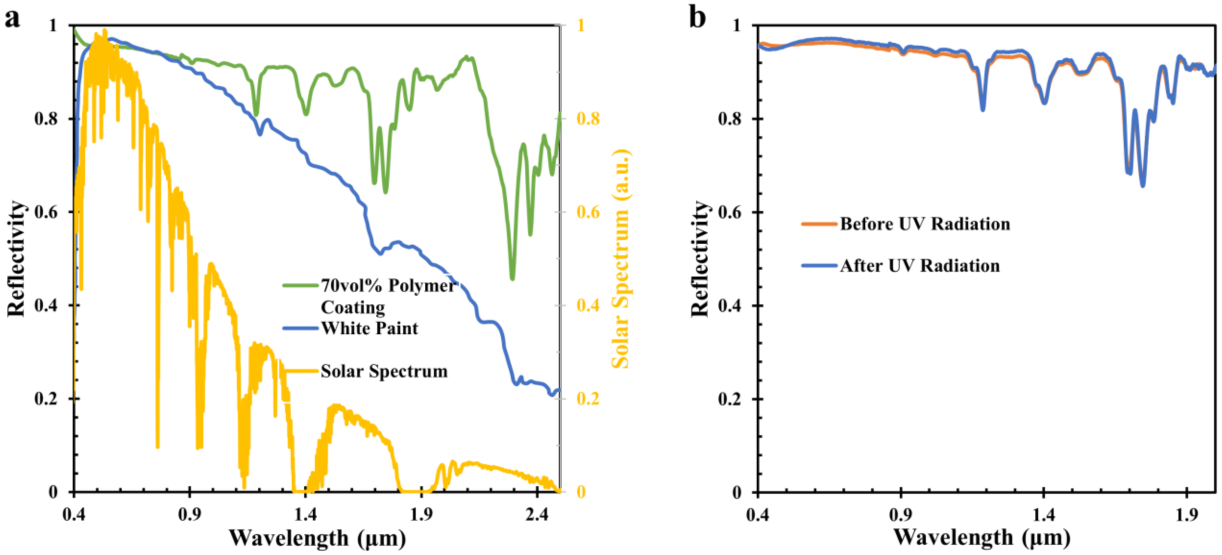

Figure 3.12 High NIR reflectivity and UV-damage-free property of 70 vol% polymer coating. (**a**) UV-VIS-NIR reflectivity comparison between commercially available TiO_2-based white paint and 70 vol% polymer coating; (**b**) UV-VIS-NIR reflectivity comparison for 70 vol% polymer coating before and after UV radiation.

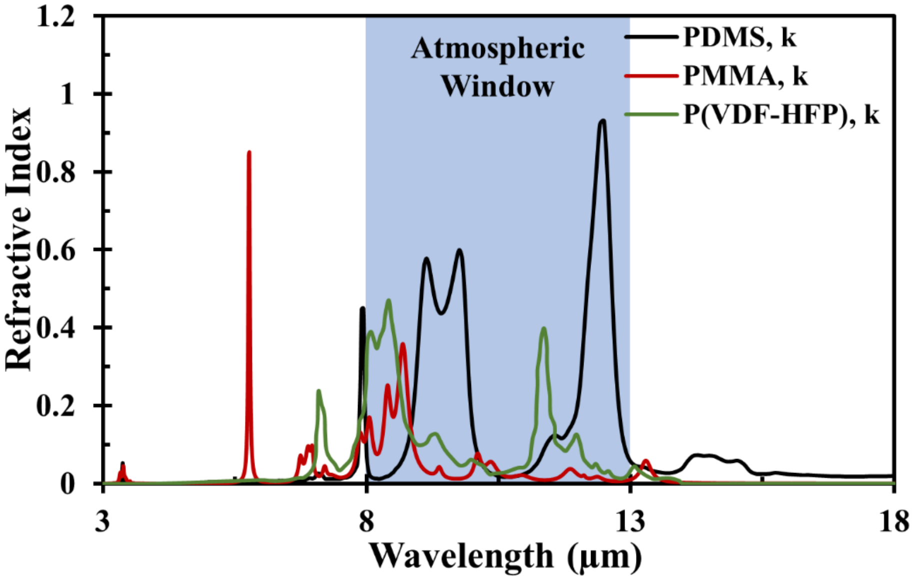

Figure 3.13 Extinction coefficients in refractive indices of PDMS, PMMA, P(VDF-HFP), showing their high emissivity in the mid-infrared wavelength region. The peaks in ***k*** correspond to different vibrational modes of various molecular structures.

3.6 Conclusions

To sum up, the low-cost and scalable cool white polymer coating with a controlled concentration of hollow glass microspheres can have the solar reflectivity of 0.92 and the mid-IR emissivity of 0.85, which leads to significant radiative cooling. The outdoor temperature measurement shows that 70 vol% polymer coating on a concrete surface helps to achieve a maximum temperature drop of 25 °C compared to the bare concrete block and exhibits a maximum sub-ambient cooling of 9 °C during the daytime with limited convective and conductive heat transfer. The building energy consumption analysis based on seven common building models in Los Angeles indicates that the annual cooling energy savings could be achieved from 2 MJ/m^2 to 12 MJ/m^2 by using the 70 vol% polymer coating on the exterior surface and the savings are more significant for higher surface area-to-volume buildings. The associated annual cost savings and annual CO_2 emission savings for representative buildings in Los Angeles are predicted to range from \$0.05/m^2 to \$0.58/m^2 and

$0.26 kg/m^2$ to $1.45 kg/m^2$, respectively. The techno-economic analysis shows that the material costs for our cool white polymer coatings is estimated to be $\$0.39/m^2$ and \$0.005/W. This work opens the possibility of using such polymer-based coatings in large-scale surface cooling for modern buildings and pave the way towards energy-efficient buildings to reduce energy consumption. Furthermore, this work provides a promising solution to resolve cooling issues for buildings with insufficient air conditioning systems, and address the global concern of the record-breaking heat waves that occurred in recent years.

3.7 Materials and Methods

3.7.1 Fabrication of Polymer Coatings

The silicone elastomer base and curing agent (Sylgard 184, from Dow Corning) is mixed with a 10:1 weight ratio in a vial to make polydimethylsiloxane (PDMS). After thoroughly stirring, it is added into a pre-weighted amount of hollow glass microspheres (iM16K, from 3M) for preparation of polymer coatings with varying volume concentrations (ϕ) of hollow glass microspheres. After being completely blended and degassed, the mixture is cast onto a substrate and dried under ambient conditions for 24 hours. It is then transferred into an oven for 2-hours 60 °C heating under vacuum conditions.

3.7.2 Mass Density Measurements

The theoretical mass density of the polymer coating is calculated by the known density of the PDMS and hollow glass microspheres. The measured mass density is equal to the measured weight of the polymer coating divided by the measured volume which is length times width times thickness. The areal density equals to the measured mass density times the measured thickness of the polymer coating.

3.7.3 Optical Spectroscopy

The optical properties of polymer coatings in the visible and NIR region are characterized by Ultraviolet-Visible-NIR (UV-VIS-NIR) spectrometer (Cary 7000, Agilent and Jasco V670 coupled with a 60 mm integrating sphere, Jasco Technology) in the wavelength range from 0.4 μm to 2.5 μm. The diffuse reflectivity and transmissivity measurements are calibrated with a standard white body. The optical properties of polymer coatings in mid-IR region are characterized by Fourier-transform infrared (FTIR) spectrometer (Nicolet 6700, Thermo Scientific) with an integrating sphere (Mid-IR IntegratIR^{TM}, Pike Technologies). The emissivity is calculated based on the sum of the transmissivity, reflectivity and absorptivity being unity and Kirchhoff's Law assuming that emissivity is considered equal to absorptivity. The optical measurements have an inherent uncertainty of ±0.003 for the properties ranging from 0 to 1 and the wavelength uncertainty of the spectrometers is ±0.3 nm at a standard room temperature of 25 °C.

3.7.4 Scanning Electron Microscopy

Scanning electron microscopy images of the polymer coatings and hollow glass microspheres are taken using a Philips XL-30 FEG scanning electron microscope (SEM).

3.7.5 Outdoor Temperature Measurements

The temperature measurement is conducted on the rooftop of the Engineering Tower at University of California, Irvine (UCI). The concrete block with a dimension of 2 inch × 2 inch × 0.5 inch and another same-size concrete block with a 2 mm-thick layer of 70 vol% polymer coating on top surface are used for a comparative study. The concrete blocks with and without 70 vol% polymer coating are placed inside the insulation Styrofoam with a low thermal conductivity of 0.063 W/(m·K), which is stabilized in a box with aluminum foil coated on the outside wall and white paper coated on the inside wall. The box with and without the wind-shield low-density-polyethylene (LDPE) film are used to simulate different surface conditions where convective heat transfer is minimized or presented. The infrared (IR) camera (FLIR, A655sc) and thermocouples (K-type, Omega) attached to a thermometer (RDXL12SD, Omega) are both used to measure the temperatures and calibrate each other. The resolution of the K-type thermocouple is 0.1 °C with an inherent measurement uncertainty of ±1.1 °C at a temperature region from 0 °C to 55 °C, while the resolution of the FLIR IR camera is 0.03 °C with an inherent uncertainty of ±0.5 °C for a measurement range of 0 °C to 70 °C. The temperature of ambient air is also measured using K-type thermocouples for comparison with predicted ambient air temperature and demonstration of temperature influence of different samples.

3.7.6 Synchrotron characterization

The tomography measurement (Nano CT) is done at Irvine Materials Research Center (IMRI). The effective pixel size is 1.02 μm × 1.02 μm. Tomography data reconstruction is done with Simpleware ScanIP, a three-dimensional (3D) segmentation and processing software developed by Synopsys Inc. The structures are thresholded and segmented from the tomographic reconstructed data and the hollow glass microspheres' size distribution analysis is done with ImageJ, '3D Objects Counter' plugin.

Chapter 4 Sprayable White Polymer Coatings based on Hollow Glass Microspheres and Binder Effect

Organic binders are widely used for optical coatings or white paints to meet the needs for efficient cooling of buildings since conventional cooling or air-conditioning approaches takes a lot of energy and even produce air pollutants. They are designed for sunlight reflection or surface cooling of buildings, but the inherent absorption of commonly used organic binders limits their reflectivity to the visible wavelength and is not effective in the near-infrared wavelength regions. In this chapter, we present a coating solution that is sprayable and reflective across the whole solar wavelength region. Instead of using organic binders, we integrate hollow glass microspheres in the diameter range of 2-40 μm within potassium bromide (KBr), with the advantage of having a lower solar absorption than the organic counterparts. The transmissivity of KBr approaches unity in the solar region according to our measurements. Solar reflectivity of white coating increases when replacing Polydimethylsiloxane (PDMS) with KBr as the binder since reflectivity in the near-infrared region is much enhanced. The solar reflectivity increases with increasing thickness. It exhibits high cooling power and is very techno-economically attractive in terms of cost per cooling power according to our calculations. We believe the sprayable white coating with the solar transparent binder provides a promising solution to improve reflectivity of white paints across the whole solar region and helps to resolve cooling issues for buildings with insufficient cooling systems.

4.1 Introduction

Resolving the increasing building energy demand across the world and associated greenhouse gas emission, air quality and human health problems requires highly innovative approaches to surface cooling and advanced materials in urban environments. The annual cooling or air conditioning energy demand is forecasted to exceed ten quintillion joules by 2040, and the associated carbon emissions and air pollution may play a critical role in early death, which is linked to 6.5 million premature deaths across the world. The lack of air conditioning in old European buildings led to thousands of deaths estimated during the record-breaking heat waves in the summer. As a potential solution, engineering building surfaces to passively control building temperatures has drawn much attention in recent years. Optical coatings for sunlight reflection or surface cooling in the ambient environment require a high reflectivity across the ultraviolet (UV), visible, and near-infrared wavelength ranges. An ideal solar-reflective coating may significantly reduce air-conditioning loads and related energy consumptions of buildings or outdoor systems that are constantly exposed to sunlight. However, the sunlight-reflection property of commercial white paints is often limited to the visible wavelength range and not very effective in the UV or in the near-infrared wavelength range, which is due to the popular use of titanium dioxide (TiO_2) pigments. In the recent literature, nanocomposites using silicon (Si), silicon dioxide (SiO_2)-based layered structures, or metallic reflectors have demonstrated considerable surface cooling properties, but their processing requirements and costs are inappropriate for large-scale applications such as cooling buildings. The cooling performance of the commercially available products is limited, and the high cost expected by the state-of-the-art materials reported in the previous literature make them not commercially viable. To address these aspects, randomly-packed SiO_2 microspheres[29] have been demonstrated with polymer composites and showed promising surface cooling properties in ambient environments. The prior work of hollow glass microspheres composites relied on a spin-coating method, in which the sample demonstration was limited to a Petri dish size and required a polydimethylsiloxane (PDMS) as a binder, which limited the near-infrared reflection. New processing approaches that are scalable and do not require casting or PDMS are necessary.

4.2 Preparation of Sprayable White Coatings

The successful demonstration of white polymer coatings based on hollow glass microspheres has indicated the potential of hollow glass microspheres in achieving high solar reflectivity. The significant temperature reduction by the polymer coating with 70 vol% of hollow glass microspheres is mainly due to its high solar reflectivity, especially high reflectivity in the visible region. However, we notice that the polymer coating using PDMS as the binder suffers some absorption in the near-infrared region and thus has a lower reflectivity than in the visible region. To further enhance the reflectivity of the white coating in the solar region, a different binder without or with little absorption in the solar region may be desired.

The possible binder material should be transparent to most of the sunlight in the wavelength region of 0.2-4 µm. There are several well-characterized broadband optical window materials that meet this transmission criterion, as shown in **Table 4.1**. Among these materials, potassium Bromide (KBr) is a commonly used binder material because it can form the matrix or sheet that integrates particles together after the solvent evaporates, as well as provide a good bond strength which provides resistance to both scaling and conformation geometry change and decreases instability of the sample. From the previous publication, we notice that KBr is highly transparent from UV to mid-infrared region (0.25-25 µm), which indicates it might be a good binder to eliminate much absorption in the solar region if it is mixed with hollow glass microspheres in the white coating.

Materials	UV Transition (μm)	IR Transition (μm)
CaF_2	0.12	8-9
MgF_2	0.12	8
BaF_2	0.14	12-14
SrF_2	0.13	10
NaCl	0.17-0.3	20
CsBr	0.2	30-40
NaF	0.14	10
KCl	0.18	18
KBr	0.21	20-30

Table 4.1 Several solar transparent materials from reference (X).

We have tried to mix KBr particles with hollow glass microspheres with various weight ratio and found that a weight ratio less than 50% for hollow glass microspheres is needed for them to be integrated by KBr sheets after the solvent evaporates. We use the de-ionized (DI) water as the solvent for sample fabrications. The commercially available hollow glass microspheres are mixed with potassium bromide (KBr) in a weight ratio of 3:7, and a certain amount of DI water is added to make the solution (**Fig. 4.1**). After thoroughly stirring, the solution is added into a commercial spray bottle and the spray bottle is used to spray the solution onto the surface that needs to be painted. The painted surface is left at room temperature or heated in the oven for the solvent to evaporate.

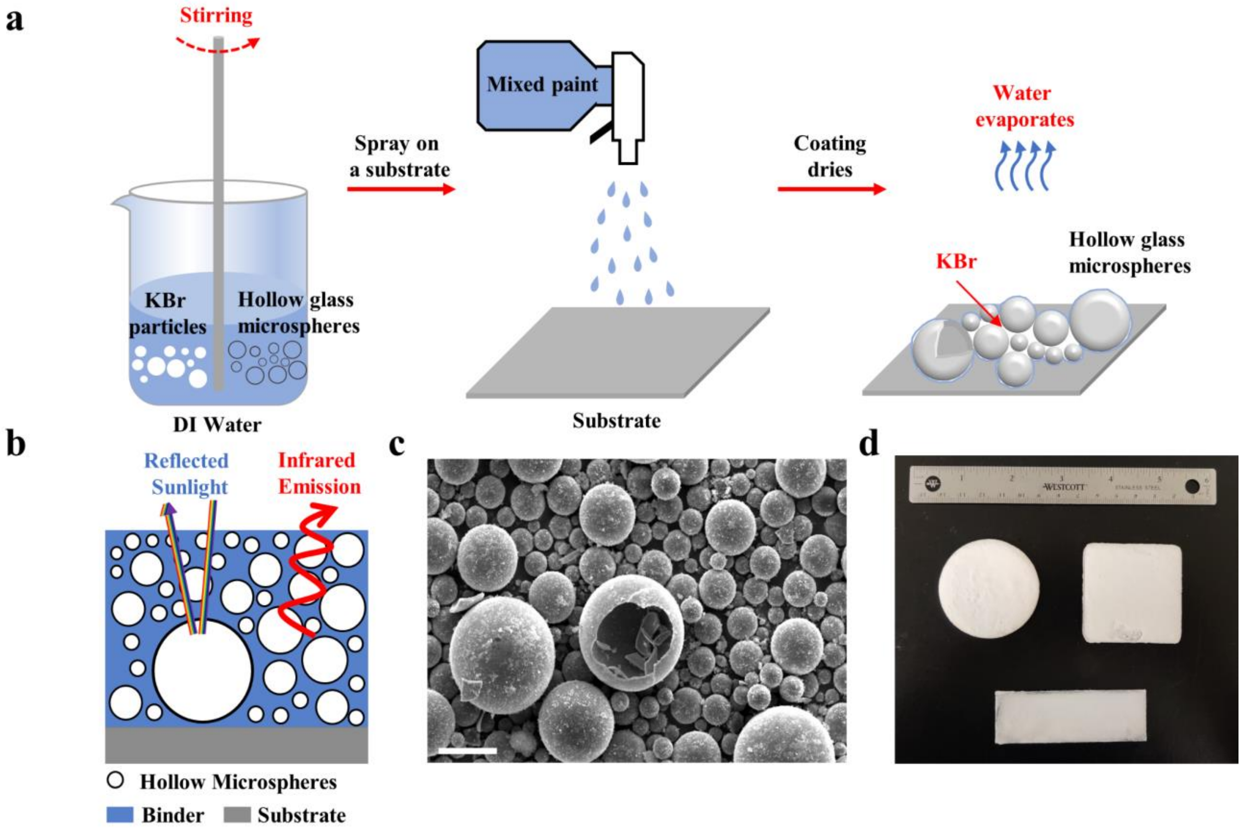

Figure 4.1 Sprayable white coating fabrication using hollow glass microspheres and solar transparent binders. (a) The schematic of sprayable white coating fabrication using spray coating method; (b) The schematic of sprayable white coating whose high solar reflectivity and infrared emissivity enables passive radiative cooling; (c) SEM image showing the diameter of hollow glass microspheres ranges from 1 to 40 µm; (d) The photos showing that the sprayable white coating could be easily applied to different substrates with various shapes.

4.3 Optical Properties and Thickness-Dependence of Sprayable Coatings

Our optical measurements indicate the little absorption of the spray coating based on hollow glass microspheres and KBr particles in the near-infrared region (**Fig. 4.2a**). A clear thickness-dependence is observed from various samples with different thicknesses. The diffusion theory can be used to develop the thickness-dependence predictions of hollow-microspheres-based-composites, and it can be applied to spray coating samples after the input has been changed to the refractive index of KBr in the solar region. The diffusion theory relates transmissivity of the composite system (***T***) to its thickness (***L***) by the following equation:

$$T = \frac{l^*(1+s)}{L + 2l^*s} \tag{4.1}$$

In equation (4.1), ***s*** is the extrapolation length ratio that can be calculated using ***s=2(1+R)/[3(1-R)]***, where ***R*** is the internal reflectance. The VAT model are used to estimate the value of ***s*** by using the refractive index of SiO_2 (n=1.45) and KBr (n=1.56), and the volume fraction of 79.7% based on the density information of two materials. The spectral reflectivity (***R_s***) is calculated using ***R_s=1-T***. **Fig. 4.2b** indicate the thickness dependence on solar reflectivity of spray coatings from a thickness of 20 µm (or 0.02 mm) to 12000 µm (or 12 mm) using the diffusion theory, which shows the agreement with measured weighted solar reflectivity values of spray coating samples that are calculated using the following equation:

$$R_{weighted} = \frac{\int_{0.3}^{2.5} R(\lambda) I_{AM1.5}(\lambda) d\lambda}{\int_{0.3}^{2.5} I_{AM1.5}(\lambda) d\lambda} \tag{4.2}$$

The thickness-dependence prediction based on the diffusion theory indicates that a solar reflectivity of 0.97 can be reached with a thickness of 3.18 mm and a solar reflectivity of 0.99 with a 9.68-mm thickness.

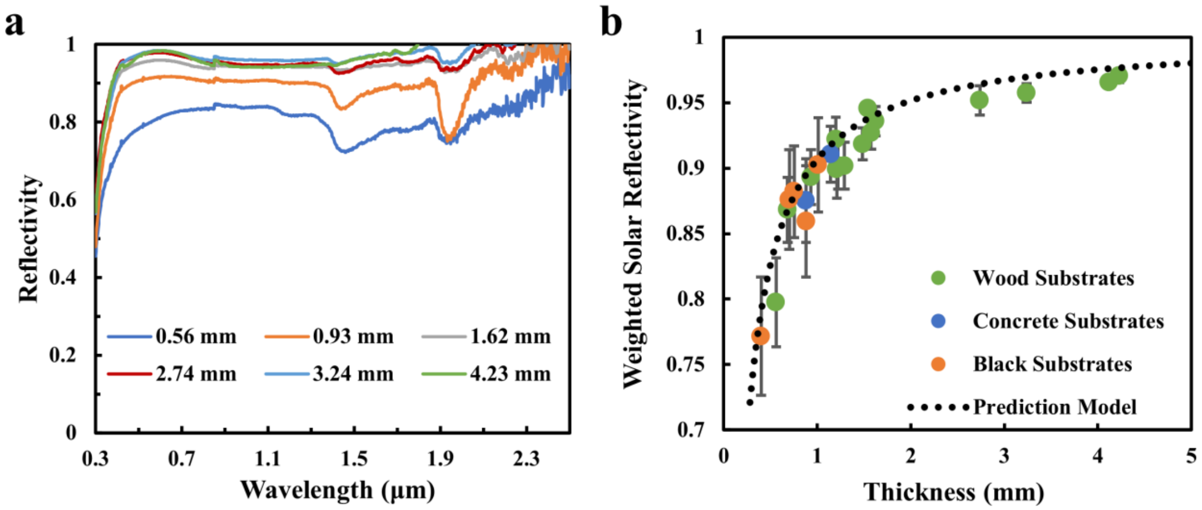

Figure 4.2 Solar reflectivity of sprayable white coatings. (a) UV-VIS-NIR reflectivity of spray coating samples with different thicknesses; (b) Weighted solar reflectivity as a function of thickness in spray coatings and reflectivity predictions based on the diffusion theory with transport mean free path calculations for a thickness of 0-5 mm. The weighted solar reflectivity $\mathbf{R}_{\mathbf{weighted}}$ is calculated using equation (X) using the measured values between wavelength of 0.3-2.0 μm.

4.4 Comparison between PDMS and KBr binder

It is clear from the UV-VIS reflectivity measurements that the spray coating samples exhibit higher reflectivity compared to polymer coatings using PDMS as the binder in the near-infrared region. **Fig. 4.3a** shows the comparison between PDMS and KBr binder. While UV and visible reflectivity of both white coating samples are similar to each other, KBr helps to increase the near-infrared reflectivity of spray coating samples compared to PDMS binder due to its solar-transparent property. This difference can be explained by the difference in the extinction coefficient values of both materials in the near-infrared region. **Fig. 4.3b** and **Fig. 4.3c** shows the extinction coefficient values of PDMS and KBr in the wavelength region of 0.3-2.5 μm and 0.1-50 μm, respectively. It is clear that PDMS has some high extinction coefficient values in the near-infrared region, leading to its strong absorption. According to our study on extinction coefficients, absorption depends on extinction coefficient values of materials. In contrast, KBr shows smaller extinction coefficient values in the whole solar region and thus leads to its solar transparency.

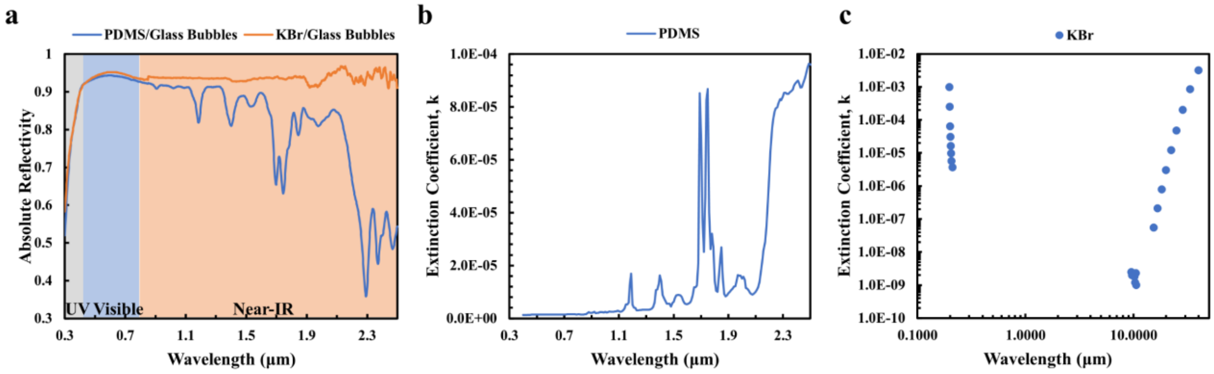

Figure 4.3 (a) Comparison of solar reflectivity between PDMS and KBr binders. For both white coatings, hollow glass microspheres are used as pigments; The extinction coefficient values of (b) PDMS in Comparison between PDMS and KBr binders. the wavelength region of 0.3-2.5 μm and (c) KBr in the wavelength region of 0.1-50 μm.

4.5 Temperature Analysis and Outdoor Temperature Measurements

We also measure the infrared optical property of sprayable white coating samples using the Fourier-transform infrared (FTIR) spectrometer using a diffuse gold as the reference. Thus, the full spectrum optical properties of sprayable white coating samples with various thicknesses are depicted in **Fig. 4.4a**. The measured values of sprayable white coatings are used in the temperature predictions and cooling power calculations based on thermal analysis in the ambient environment. Assuming a steady ambient environment, a representation daily weather data in the summer, a constant conductive and convective heat transfer coefficient h=10 W/m^{2}K and a peak solar irradiance of 1000 W/m^2, the calculation shows that the maximum temperature drop can reach

5.3°C while the cooling power at the peak solar irradiance is 78.2 W/m^2 for the spray coating with a thickness of 3.24 mm (**Fig. 4.4b**).

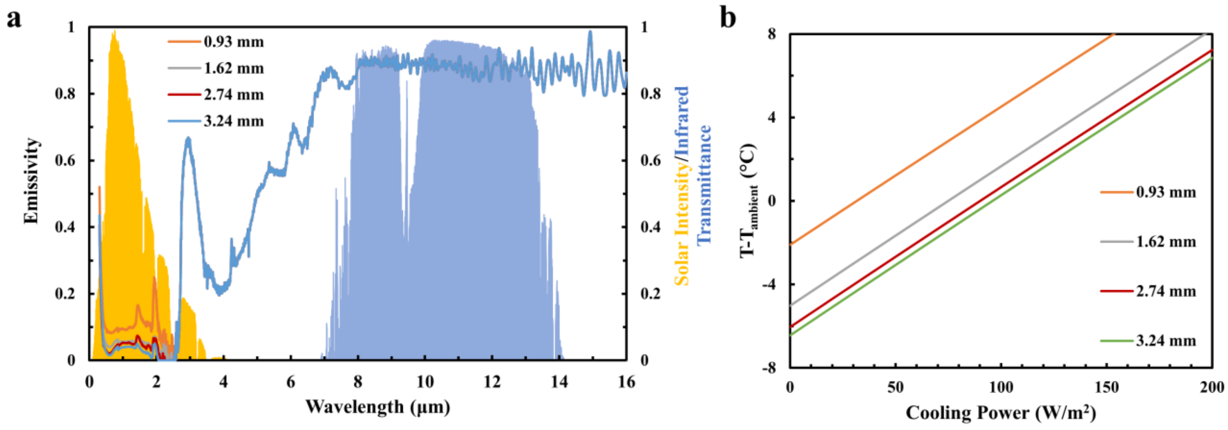

Figure 4.4 Full spectrum optical property and cooling power of spray coatings. (a) Full spectrum optical property of spray coatings with different thicknesses in the wavelength region of 0.3-16 μm; The solar intensity distribution (yellow) and atmospheric transmission (blue) are plotted as references. (b) Temperature difference between surface of spray coating and ambient air as a function of cooling power. For this temperature and cooling power prediction, the calculated emissivity values based on measured reflectivity data from spectroscopy are used. A solar intensity of 1000 W/m^2, a constant conductive and convective heat transfer coefficient h=10 W/m^2K and an ambient air temperature of 27°C are assumed.

We also conduct the outdoor temperature measurements on the spray coating samples with and without the wind-shield infrared-transparent LDPE film, when the spray coating are coated on the concrete surface (**Fig 4.5**). A 2 inch × 2 inch × 0.5 inch concrete block with spray coating on the surface is compared with a same-size concrete block without any coating and another same-size concrete block with commercial TiO_2-based white paint on the surface, for a comparative study. The measurement results indicate that the spray coating helps to achieve a significant temperature reduction of 30°C compared to the black-painted concrete when the LDPE film is covered on the top to limit the convection. When LDPE film is not covered and the convection is more significant, the spray-coated concrete maintains around 5°C below ambient temperature during the daytime, and its temperature is around 25°C lower than the black-painted concrete. The measurements also indicate the superior cooling performance of the spray coating sample compared to the commercial TiO_2-based white paint, which shows the potential of such spray coatings in surface cooling applications.

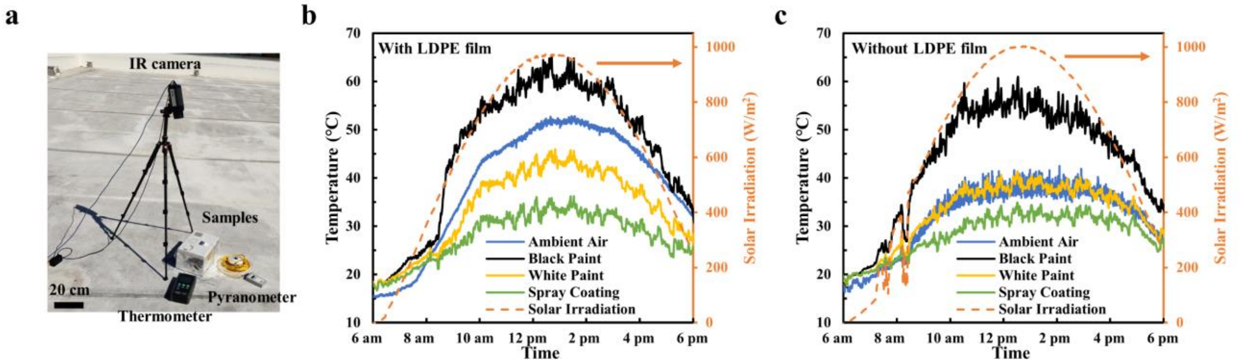

Figure 4.5 Rooftop temperature measurements for sprayable white coatings. (a) The picture of the rooftop temperature measurement apparatus; Daytime rooftop temperature measurement results (b) with and (c) without wind-shield IR transparent LDPE film.

4.6 Conclusions

We have already successfully prepared the sprayable white coating samples using the KBr binder and hollow glass microspheres, with a simple spray coating method. The white coating samples can be fabricated with various substrates, different shapes, or dimensions. Our optical measurements show that the spray coating samples with KBr binders exhibits high reflectivity throughout the whole solar region due to high solar transparency of KBr, and high emissivity in the infrared region. Solar reflectivity of white coating increases from 0.92 to 0.96 when replacing Polydimethylsiloxane (PDMS) with KBr as the binder since reflectivity in the near-infrared region is much enhanced. The net cooling power of the sprayable white coating is calculated to be 96 W/m^2 when assuming a solar intensity of 1000 W/m^2 and a constant ambient temperature of 25°C. The solar reflectivity increases from 0.90 to 0.97 with increasing thickness from 1 mm to 4 mm. Our temperature measurement results shows that the spray coating leads to lower surface temperature compared to commercial white paint when coated on commercial wood substrate. We believe the sprayable white coating with the solar transparent binder provides a promising solution to improve reflectivity of white paints across the whole solar region and helps to resolve cooling issues for buildings with insufficient cooling systems.

4.7 Materials and Methods

4.7.1 Fabrication of Spray Coatings

The potassium bromide powders are mixed and dissolved in the certain amount of DI water in a beaker. After thoroughly stirring, a pre-weighted amount of hollow glass microspheres (iM16K, from 3M) is added to the beaker for preparation of spray coatings with certain weight ratio of hollow glass microspheres. After transferring the solution from the beaker to a common spray bottle, the solution is sprayed onto a substrate and dried under ambient conditions for 24 hours. It is then transferred into an oven for 60 °C heating until fully dried.

4.7.2 Optical Spectroscopy

The optical properties in the visible and NIR region are characterized by Ultraviolet-Visible-NIR (UV-VIS-NIR) spectrometer (Jasco V670 coupled with a 60 mm integrating sphere, Jasco Technology) in the wavelength range from 0.3 μm to 2.5 μm. The diffuse reflectivity measurements are calibrated with a standard white Spectralon standard. The optical properties in mid-IR region are characterized by Fourier-transform infrared (FTIR) spectrometer (Nicolet 6700, Thermo Scientific) with an integrating sphere (Mid-IR IntegratIR^{TM}, Pike Technologies). The emissivity is calculated based on the sum of the transmissivity, reflectivity and absorptivity being unity and Kirchhoff's Law assuming that emissivity is considered equal to absorptivity. The optical measurements have an inherent uncertainty of ±0.003 for the properties ranging from 0 to 1 and the wavelength uncertainty of the spectrometers is ±0.3 nm at a standard room temperature of 25°C.

4.7.3 Scanning Electron Microscopy

Scanning electron microscopy images of spray coatings and hollow glass microspheres are taken using a Magellan 400 scanning electron microscope (SEM).

4.7.4 Outdoor Temperature Measurements

The temperature measurement is conducted on the rooftop of the Engineering Hall at University of California, Irvine (UCI). The wood substrate with a dimension of 2 inch × 2 inch × 0.1 inch with a commercial black paint, a commercial white paint, and a spray coating on top surface are used for a comparative study. The wood substrates are placed inside the insulation Styrofoam with a low thermal conductivity of 0.063 W/(m·K), which is stabilized in a box with aluminum foil coated on the outside wall and white paper coated on the inside wall. The box with and without the wind-shield low-density-polyethylene (LDPE) film are used to simulate different surface conditions where convective heat transfer is minimized or presented. The infrared (IR) camera (FLIR, A655sc) and thermocouples (K-type, Omega) attached to a thermometer (RDXL12SD, Omega) are both used to measure the temperatures and calibrate each other. The resolution of the K-type thermocouple is 0.1°C with an inherent measurement uncertainty of ±1.1°C at a temperature region from 0°C to 55°C, while the resolution of the FLIR IR camera is 0.03°C with an inherent uncertainty of ±0.5°C for a measurement range of 0°C to 70°C. The temperature of ambient air is also measured using K-type thermocouples for comparison with predicted ambient air temperature and demonstration of temperature influence of different samples.

Chapter 5 High Solar Reflectivity based on Y_2O_3 Hollow Microspheres

Since the numerical simulation results demonstrate that Y_2O_3 hollow microspheres are promising to achieve near-unity solar reflectivity with low thickness, we experimentally fabricate Y_2O_3 hollow microspheres using carbon microspheres templated hydrothermal approach. By integrating Y_2O_3 hollow microspheres with KBr binder, the white coating achieves an ultrahigh solar reflectivity without any metallic reflectors, which is comparable to or exceeds many previous reported values.

5.1 Introduction

Resolving the skyrocketing worldwide energy consumption associated with rapid urbanization and population growth calls for novel cooling technologies and innovative materials for use in urban environments. The annual cooling or air conditioning energy demand is forecasted to exceed ten quintillion joules by 2040, and the associated carbon emissions and air pollution may play a critical role in early death, which is linked to 6.5 million premature deaths across the world. As a potential solution, passive cooling materials with high solar reflectivity and infrared emissivity have gained more and more attention these years. To achieve passive radiative cooling, usually a solar reflectivity higher than 0.9 and an infrared emissivity higher than 0.9 is needed. Multilayer nanophotonic structures, two dimensional or three dimensional metamaterials, polymer-based radiative coolers, and pigment-embedded composite systems are developed for promising cooling applications. Considering solar intensity is around 1000 W/m^2 while theoretical radiation cooling power is around 150 W/m^2, people focus more on minimizing solar absorptivity of materials by enhancing solar reflectivity across the ultraviolet, visible, and near-infrared wavelength region. Many efforts have been tested for solar reflectivity values between 0.93 and 0.979, such as using metallic reflectors, porous structures, solid nanoparticles or microspheres, and hollow microspheres.

Our numerical simulation results indicate that ceramic materials with high refractive index and low extinction coefficient values such as Y_2O_3 are promising to achieve near-unity solar reflectivity once fabricated into hollow micro- or nanospheres. In this work, we successfully synthesize Y_2O_3 hollow microspheres using carbon microsphere templated hydrothermal approach and fabricate white coatings with Y_2O_3 hollow microspheres. The synthesized hollow microspheres are characterized using scanning electron microscope (SEM) and energy dispersive (EDS) analysis. We perform optical measurements to characterize reflectivity of white coatings in the solar region and calculate the weighted solar reflectivity. We also study the reflectivity with various thicknesses and developed a thickness-dependent reflectivity prediction model based on the diffusion theory. The thermal analysis of white coatings based on Y_2O_3 hollow microsphere are conducted to demonstrate the cooling performance.

5.2 Preparation of Y_2O_3 Hollow Microspheres

The preparation of metal oxide hollow microspheres have been studied and summarized in several previous publications. Templated hydrothermal reactions are generally used for hollow microspheres fabrication due to its safe and easy operations. Inspired by these studies, we also use similar hydrothermal treatment to fabricate Y_2O_3 hollow microspheres. The fabrication process is composed of three steps in the following:

1. The synthesis of carbon microspheres template by hydrothermal carbonization of glucose
2. Formation of a precursor with core-shell structure by a homogenous precipitation method using urea as the precipitation agent (90°C)

3. Calcination of the precursor in air to remove the carbon cores and make the precursor shell decompose completely, thus resulting in Y_2O_3 hollow microspheres

A schematic illustration for the overall formation process of the Y_2O_3 hollow microspheres is presented in **Fig. 5.1**. In the second step, urea serves as a precipitating agent and plays an important role in the formation of precursor shell onto the surfaces of carbonaceous microspheres. The decomposition of urea releases precipitating anions (mainly OH- and CO_3^{2-}) slowly into the solution at the elevated temperature and results in the homogeneous precipitation of the precursor nanoparticles coated on the carbon microsphere surface. In the calcination step, carbon microsphere cores are burned out and the shell of precursor nanoparticles is transformed into crystalline oxide hollow microspheres.

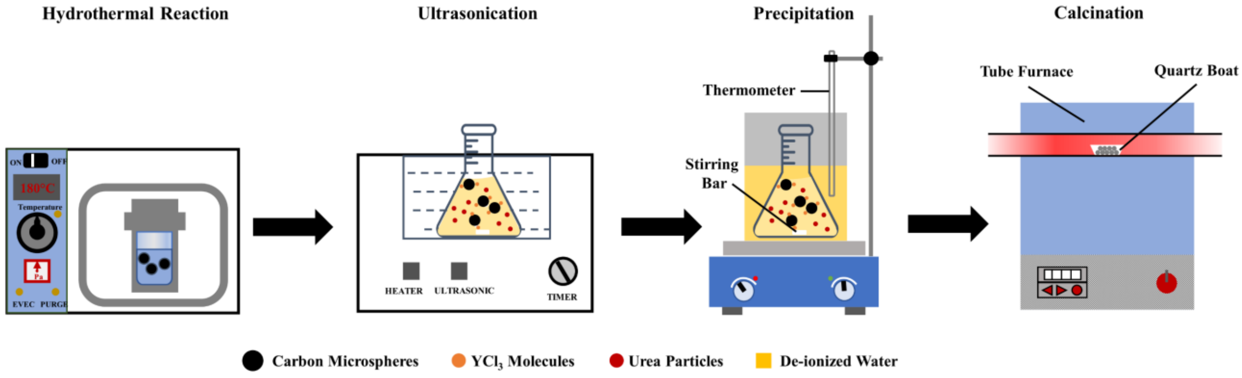

Figure 5.1 Schematic of fabrication process of Y_2O_3 hollow microspheres. The process involves (1) the formation of carbon spheres using hydrothermal treatment; (2) coating of the carbon microsphere cores with YCl3 precursors using ultrasonication and subsequent urea-based precipitation at elevated temperatures; and (3) removal of carbon cores via calcination at high temperatures in the tube furnace.

Fig. 5.2a shows the top-view scanning electron microscope (SEM) image of carbonaceous microspheres. The SEM image indicates carbonaceous microspheres have a diameter range of around 8-10 µm. **Fig. 5.2b** and **Fig. 5.2c** show the SEM images of Y_2O_3 hollow microspheres after

800°C calcination for 6 hours in tube furnace. Images show that hollow microspheres exhibit a diameter of around 5-8 µm, shrinking when the carbon cores are burned out during the calcination process. The hollow structures are also significant in the SEM images and the shell thickness is measured to be around 100-200 nm. **Fig. 5.2d** is the energy dispersive (EDS) analysis of hollow microspheres showing that Y and O elements are the main elements in them while C element is also shown because of the carbon tape beneath the microspheres. We also perform an EDS mapping on the SEM image shown in **Fig. 5.2e** and the results are presented in **Fig. 5.2f**. It is clear that Y and O elements are only abundant in hollow microspheres while C and Cl in the precursors are not apparent in microspheres. The SEM and EDS characterizations indicate the successful fabrication of Y_2O_3 hollow microspheres.

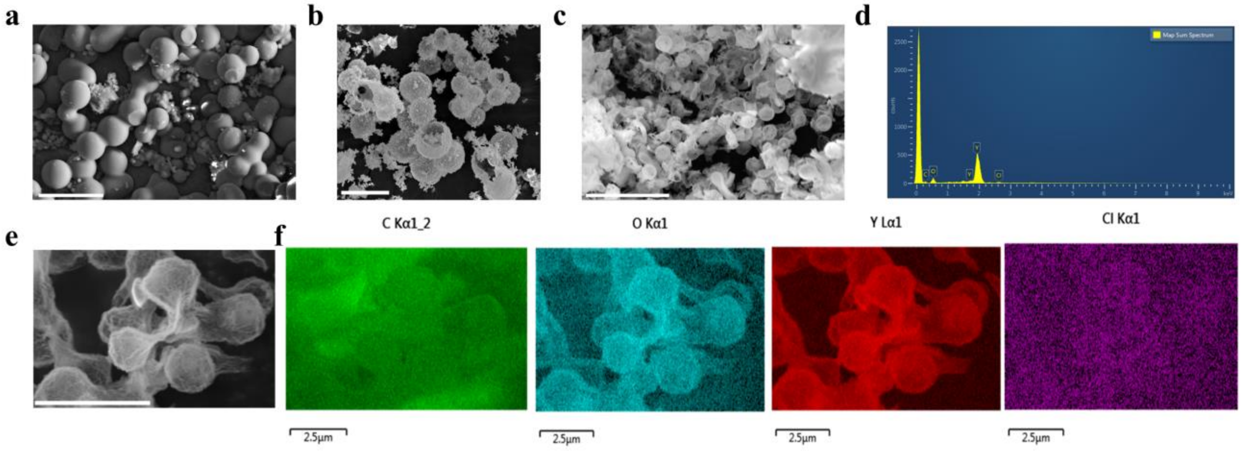

Figure 5.2 Characterization of Y_2O_3 hollow microspheres. (a) Top-view SEM image of carbon microspheres after hydrothermal reaction at 180°C for 8 hours. Scale bar: 20 µm; (b-c) Y_2O_3 hollow microspheres after calcination at 800°C for 6 hours. Scale bar: 10 µm; (d) EDS analysis on Y_2O_3 hollow microspheres showing the presence of Y and O elements; (e) Zoom-in SEM image of Y_2O_3 hollow microspheres and (f) corresponding EDS mapping of C, O, Y and Cl elements. Scale bar: 10 µm.

5.3 Preparation of Y_2O_3-based White Coatings

The successful fabrication of Y2O3 hollo microspheres makes white coating fabrication possible. We use potassium bromide (KBr) binder to integrate hollow microspheres together due to its solar transmittance in the whole solar region. Our previous measurements on spray coatings based on hollow glass microspheres show that KBr is almost 100% transparent in the entire solar region. **Fig. 5.3** is a simple schematic showing the white coating fabrication process. After ultrasonication of mixed hollow microspheres and KBr in the DI water, the solution is drop-casted onto any substrates such as wood, concrete and glass slide with various shapes and dimensions. The weight ratio of hollow microspheres is controlled as 40% so that they can be fully integrated by KBr binder.

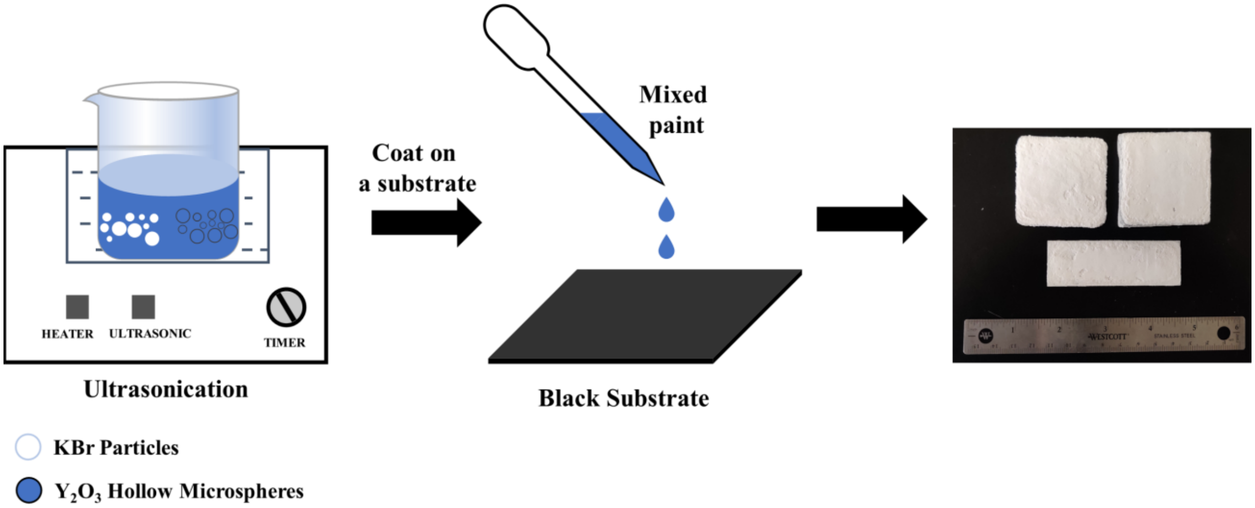

Figure 5.3 Fabrication process schematic of white coatings based on Y_2O_3 hollow microspheres and KBr binder. KBr particles are first dissolved in DI water and then Y_2O_3 hollow microspheres are dispersed in the solution. After ultrasonication for 10 mins, the mixed solution is drop-casted onto black substrates to make the white coating materials.

5.4 Optical Properties and Thermal Analysis of Y_2O_3-based White Coatings

Our previous numerical simulation results indicate that Y_2O_3 hollow microspheres could lead to ultrahigh reflectivity in the solar region and we perform optical measurements of white coatings after fabrications. The solar reflectivity of white coatings are measured using Ultraviolet-Visible-Near Infrared (UV-VIS-NIR) spectroscopic measurements in the wavelength region of 0.3-2.5 µm. The measured results show that white coatings based on Y_2O_3 hollow microspheres exhibit ultrahigh reflectivity across the UV, visible and near infrared region. We thus calculate weighted solar reflectivity using equation (5.1) below in the wavelength region of 0.3-2.4 µm. The weighted solar reflectivity of the 0.48-mm-thick white coating reaches 0.9632, while it increases to 0.9789 with a thickness of 0.92 mm (**Fig. 5.4a**).

$$R_{weighted} = \frac{\int_{0.3}^{2.5} R(\lambda) I_{AM1.5}(\lambda) d\lambda}{\int_{0.3}^{2.5} I_{AM1.5}(\lambda) d\lambda} \tag{5.1}$$

A clear thickness-dependence is observed from various samples with different thicknesses. The diffusion theory can be used to develop the thickness-dependence predictions of hollow-microspheres-based-composites, and it can be applied to spray coating samples after the input has been changed to the refractive index of KBr in the solar region. The diffusion theory relates transmissivity of the composite system (***T***) to its thickness (***L***) by the following equation:

$$T = \frac{l^*(1+s)}{L + 2l^*s} \tag{5.2}$$

In equation (5.2), ***s*** is the extrapolation length ratio that can be calculated using $s=2(1+R)/[3(1-R)]$, where ***R*** is the internal reflectance. The VAT model are used to estimate the value of ***s*** by using the refractive index of Y_2O_3 (n=1.9) and KBr (n=1.56). The spectral reflectivity (R_s) is calculated using $R_s=1-T$.

Fig. 5.4b indicate the thickness dependence on solar reflectivity of white coatings from a thickness of 20 μm (or 0.02 mm) to 2000 μm (or 2 mm) using the diffusion theory, which shows the agreement with measured weighted solar reflectivity values.

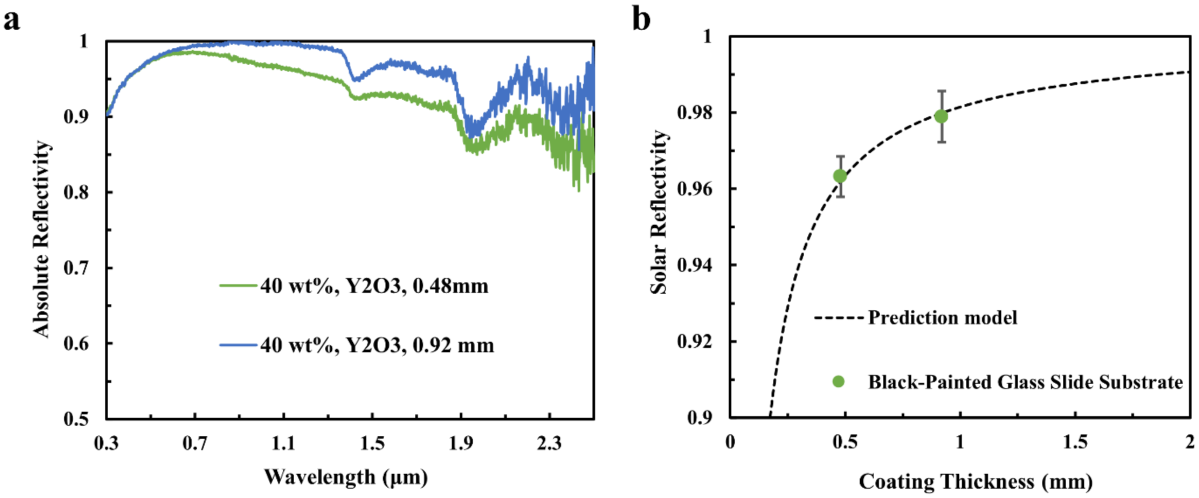

Figure 5.4 UV-VIS-NIR reflectivity of Y_2O_3 hollow microspheres based white coatings. (a) Absolute UV-VIS-NIR reflectivity of 0.48-mm-thick and 0.92-mm-thick white coating based on Y_2O_3 hollow microspheres on glass slide substrates; (b) Weighted solar reflectivity as a function of thickness in Y_2O_3 hollow-microspheres-based white coatings and reflectivity predictions based on the diffusion theory with transport mean free path calculations for a thickness of 0-2 mm. The weighted solar reflectivity $\boldsymbol{R}_{weighted}$ is calculated using equation (5.1) in the main text.

5.5 Conclusions

To sum up, we synthesize Y_2O_3 hollow microspheres using carbon microspheres templated hydrothermal approach. The approach involves the formation of carbonaceous microspheres using hydrothermal reaction, the homogeneous precipitation of precursor materials on the surface of carbonaceous microspheres with the assistance of urea, and the removal of carbon cores with high temperature calcination. White coatings based on Y_2O_3 hollow microspheres have been fabricated on various substrates using a common casting method. Our reflectivity measurements indicate that Y_2O_3 hollow microspheres lead to ultrahigh solar reflectivity of 0.9789 with a thickness of 0.92 mm. Solar reflectivity of white coatings presents strong relationship with their thicknesses, which can be predicted using the diffusion theory. This work demonstrate the ultrahigh solar reflectivity and provides promising solutions for near-perfect solar reflectors with scalable and easy fabrications.

5.6 Materials and Methods

5.6.1 Synthesis of Y_2O_3 hollow microspheres

Preparation of Carbonaceous Microspheres. In a typical preparation, 28 g of glucose is dissolved in 240 mL of DI water to form a clear solution. The solution is then sealed in a 500 mL PTFE-lined stainless steel autoclave and maintained at 180°C for 8 hours. After naturally cooling the autoclave to room temperature, the resulting solution is washed with DI water several times and then dried at 100°C in the oven for 12 hours.

Synthesis of Y_2O_3 Hollow Microspheres. 1.6 g of YCl_3 precursor is dissolved in 150 mL DI water to form a clear solution. 8 g of urea and 5 g of carbonaceous microsphere from the last procedure is added into the solution. The solution is ultrasonicated for 20 mins and then transferred to a water bath at 90°C for 3 hours with vigorous stirring. Then the resulting solution is vacuum filtered and the precursors are washed by DI water several times before dried in the oven. The final hollow microspheres are obtained by calcination in the tube furnace at 800°C for 6 hours with a heating rate of 2°C/min.

5.6.2 Optical spectroscopy

The optical properties in the visible and NIR region are characterized by Ultraviolet-Visible-NIR (UV-VIS-NIR) spectrometer (Jasco V670 coupled with a 60 mm integrating sphere, Jasco Technology) in the wavelength range from 0.3 μm to 2.5 μm. The diffuse reflectivity measurements are calibrated with a standard white Spectralon standard. The optical properties in mid-IR region are characterized by Fourier-transform infrared (FTIR) spectrometer (Nicolet 6700, Thermo Scientific) with an integrating sphere (Mid-IR IntegratIR^{TM}, Pike Technologies). The emissivity is calculated based on the sum of the transmissivity, reflectivity and absorptivity being unity and Kirchhoff’s Law assuming that emissivity is considered equal to absorptivity. The optical measurements have an inherent uncertainty of ±0.003 for the properties ranging from 0 to 1 and the wavelength uncertainty of the spectrometers is ±0.3 nm at a standard room temperature of 25°C.

5.6.3 Scanning electron microscopy

Scanning electron microscopy images of Y_2O_3 hollow microspheres are taken using a Magellan 400 scanning electron microscope (SEM). The composition of the samples are inspected using the Magellan 400 SEM equipped with an energy-dispersive X-ray spectrum and mapping.

Chapter 6 Energy and Cost Saving Analysis of White Coatings for Residential Buildings

Although white coatings have been demonstrated as promising materials for radiative cooling, energy, and cost savings of white coating in buildings have not been fully evaluated. In this chapter, we calculate the energy and cost savings of ideal white coatings with unity solar reflectivity and infrared emissivity and polymer coatings based on hollow glass microspheres for midrise apartments building models in various climate zones across the United States. We demonstrate both positive and negative effects of white coatings including cooling peak load reduction, heating energy increase, carbon emission savings and utility cost savings, and analyze thermal comfort improvements of white coatings in buildings without cooling systems. Additionally, we examine the statistical relationships between critical performance metrics and general weather and location parameters using the analysis of variables (ANOVA) coupled with linear regression. The findings in this dissertation will guide the material selection for ultrahigh solar reflectivity and fabrication of future white coatings for thermal management in building applications.

6.1 Introduction

Both rapid urbanization and climate change are leading to skyrocketing cooling energy demand[5]. The building sector consumes 40% of total worldwide energy[94]. Building space conditioning is usually addressed with conventional heating, ventilation, and air-conditioning (HVAC) systems, which accounts for more than half of the total building energy[95]. Conventional active cooling technologies can increase greenhouse gas emissions while exacerbating urban heat island effects[2,8,95]. Radiative cooling technology is arousing great attention as it can passively cool surfaces without any energy input[8,96].

Recent theoretical and experimental demonstrations of radiative cooling materials represent a breakthrough in achieving passive daytime cooling for buildings. These passive radiators utilize the atmospheric transmission window in the mid-infrared (mid-IR) wavelength of 8-13 μm to emit thermal radiation to the cold outer space at a temperature of 3K[8,96]. These radiators can be either used as low-temperature heat exchangers[97], integrated into roof structures[98,99], integrated with solar heating to provide thermal management towards net-zero buildings[36,100], or directly engineered into building siding and structural[35]. Among various radiative cooling materials, white coatings[22,50,78,94,95,98,101,102] have been proposed and demonstrated as effective surface cooling materials for building applications. White coatings are developed to reflect most of the sunlight in the wavelength region of 0.3-2.5 μm such that the heat absorption from the sun is minimized. Thus, surface temperatures are reduced by white coatings and less cooling energy is consumed for buildings.

Initially white paints based on titanium oxide (TiO_2) or barium sulfate ($BaSO_4$) were used as white roofs to cool residential or commercial buildings in California and Florida[103–105]. Results show large cooling energy and electricity savings. New coatings have been developed and brought to market with exceptionally high solar reflectivity and thermal emissivity properties[106]. Different white paint products have been tested in different areas[107–113] around the world to demonstrate their energy saving possibility when painted on roof. In recent years, white coatings were further studied to enhance their solar reflection. Materials based on porous structures[50], nanoparticles[22,24,30], and hollow microspheres as hollow glass microspheres[29,44], glass microspheres[27], $BaSO_4$[24] and calcium carbonate ($CaCO_3$) nanoparticles[30] have been developed. These state-of-the-art white coatings usually have a solar reflectivity of around 0.95 and an infrared emissivity above 0.9 for surface cooling.

White coatings demonstrate a large amount of cooling energy and electricity savings for various commercial and residential buildings in different locations[29,50,98]. Historical modeling efforts have focused on examining the application of white coatings on building roofs and walls. Recent work has examined the effect of various white coatings with different emissivity when applied to an office building in a cold climate[114], how white coatings paired with different roof configurations improve interior comfort and reduce energy demand for buildings in Cairo, Egypt[115], compared white coatings with dynamic emissivity versus green roofs for different climate zones in Iran[116], the application of a white coating to a roof with adjustable geometry in China[117], and direct examination of white coating effectiveness when applied to a simple building structure in different climate zones in China[118]. All of these studies utilize the EnergyPlus building energy simulator engine[119].

white coatings also have the potential to support disadvantaged and low-income communities. Reduced cooling loads can shrink utility bill burdens for low-income households who tend to use a higher fraction of income on energy[120,121]. White coatings can also make buildings without active space cooling more comfortable. Recent work examined the impact of various building envelope improvements, including a commercially available white coating, on interior temperature and occupant comfort[122]. This work shows that white coatings on roofs and walls improve comfort when applied to residential buildings in a warm climate.

Prior studies have typically focused on a limited number of climate zones and considering coatings with radiative properties below best-in-class commercial or experimental coatings. Analyses of white coatings are typically presented versus other white coatings and conventional building materials, but do not determine performance versus an ideal white coating. Finally, extensibility of results to other regions is addressed qualitatively by examining multiple climate zones or is not examined at all. The goal of the current work is to add to this literature by developing custom residential building energy models to:

- Evaluate changes in building energy use and thermal comfort of an ideal white coating with perfect solar reflectivity and infrared emissivity and the resulting change in utility cost and carbon emissions across 32 climate zones in the United States
- Examine same performance metrics with a new white coating material using hollow glass microspheres developed in for the same 32 climate zones
- Develop quantitative methods to extend simulation results to other regions not addressed in the current work

Simulations are carried out using the building energy model simulator EnergyPlus with the U.S. Department of Energy mid-rise apartment building energy model[89]. The energy model is simulated for reference cities for climate zones designated by the American Society of Heating, Refrigeration and Air-Conditioning Engineers (ASHRAE) and by the California Energy Commission (CEC). Results from the different climate zones are analyzed using analysis of variance (ANOVA) to reveal relationships between climate and location factors, and energy savings and interior comfort metrics. Linear regression is then used to develop quantitative descriptions of the relationships. This use of ANOVA and linear regression has been previously used in building energy simulation to optimize simulation parameters[123–125], or to consider the effect of different building designs[126].

6.2 Approach and Methods

The goal of the current work is to determine the effects caused by the application of ideal white coating to the opaque sections of a building exterior, and to examine the performance of a state-of-the-art white coating relative to the ideal white coating. The approach of the current work was extremely straightforward. Existing midrise apartment building energy models (BEM) for different climate zones across the United States were used to analyze the performance of an ideal and our white coating material. Each BEM was first simulated without modification to establish baseline energy use in each climate zone. Opaque exterior surfaces were then adjusted to match white coating experimental properties, and each BEM was re-simulated to determine the effect of white coatings. The financial and environmental impact of white coatings were estimated using BEM outputs combined with average cost of energy and carbon emission factors associated with each climate zone. Finally, the statistical analysis used analysis of variance to select critical factors that could be used to extend our results to different climate zones not directly captured in our work.

Two BEM scenarios were tested for each climate zone: with and without active space cooling systems. Critical outputs from each BEM include electricity and fuel energy use, peak electricity demand, and interior temperatures. Cost of energy and total carbon emissions were then calculated using these BEM outputs.

6.2.1 Building Energy Modeling

The purpose of the BEM is to resolve the physics associated with building operation such that we can predict how the thermal effect of a white coating will affect overall building energy use and comfort. We use EnergyPlus 9.3.0[119] to model the energy savings of polymer coatings and ideal coatings on exterior surfaces of buildings, including wall siding and roofing membranes. EnergyPlus is the U.S. Department of Energy (DOE) flagship whole-building energy simulation platform[127]. Among numerous features and capabilities, three critical components of the EnergyPlus tool relevant to the current work are:

- Detailed physical descriptions of building construction materials (e.g., the radiative properties of roof and opaque wall materials).

- Physical resolution of energy and mass transfers between the building exterior and different interior zones.
- Existing building energy model (BEM) templates capturing typical building types, construction sets, and occupant behavior patterns[89] tailored to 16 different climate zones across the United States, defined by the American Society of Heating, Refrigerating, and Air-Conditioning Engineers (ASHRAE).

The 2004 reference midrise apartment BEMs associated with these 16 climate zones were used for this work. The basic geometry of this BEM is shown in Figure 6.2. Building construction sets and systems were taken as-is from the reference model. To maintain consistency across climate zones, it was assumed that all buildings were heated using natural gas. Cooling and heating thermostat targets were set to 24^{o}C and 20^{o}C respectively. Instead of modifying the space conditioning system, BEM thermostat cooling setpoints were increased to simulate a scenario where space cooling is not available. **Table 6.1** lists the additional BEM information[89].

Building Model	**Total Floor Area (m^2)**	**Number of Floors**	**Aspect Ratio**	**Cooling Systems**	**Heating Systems**
Midrise Apartment	3134.59	4	2.74	Packaged Air-Conditioning Unit- Split System	Gas Furnace

Table 6.1 Detailed dimensional and system information of prototype midrise apartment building model developed by DOE.

In addition to examining the 16 ASHRAE climate zones, 16 climate zones specific to California were included for analysis. These climate zones are specified according to the California Energy Commission (CEC)[128,129]. **Table 6.2** lists the reference city for each ASHRAE and CEC climate zone. TMY3 weather data for ASHRAE and CEC climate zone reference cities were used for each BEM[91].

City	Nation-Level Climate Zones	City	State-Level Climate Zones
Miami, FL	1	Eureka, CA	1
Houston, TX	2A	Napa, CA	2
Phoenix, AZ	2B	San Francisco, CA	3
Atlanta, GA	3A	San Jose, CA	4
Los Angeles, CA	3B-Coast	Santa Maria, CA	5
Las Vegas, NV	3B-Coast	Los Angeles (LAX), CA	6
San Francisco, CA	3C	San Diego, CA	7
Baltimore, MD	4A	Long Beach, CA	8
Albuquerque, NM	4B	L. A. Civic Center, CA	9
Seattle, WA	4C	Riverside, CA	10
Chicago, IL	5A	Red Bluff, CA	11
Boulder, CO	5B	Stockton, CA	12
Minneapolis, MN	6A	Fresno, CA	13
Helena, MT	6B	Barstow, CA	14
Duluth, MN	7	Brawley, CA	15
Fairbanks, AK	8	Bishop, CA	16

Table 6.2 16 representative cities in 8 ASHRAE climate zones across US and 16 representative cities in 16 CEC climate zones in California.

6.2.2 White Coating Model

In this study, we consider two white coatings: white coatings with a solar reflectivity of 1 and an infrared emissivity of 1 (labeled as “ideal cooling”), and state-of-the-art white coating based on hollow glass microspheres and PDMS (labeled as “polymer coating”) with a solar reflectivity of 0.92 and infrared emissivity of 0.9. The prototype midrise apartment building model from the DOE database is directly utilized to generate reference energy use pattern and it is modified by adding a 2-mm-thick layer of white coating (both ideal cooling and polymer coating) onto the exterior surfaces of roofs and walls to generate the modified energy use patterns.

6.2.3 Post-BEM Analysis – Cost, Emissions, and Comfort

BEM outputs include building wide electricity and natural gas demand, and interior temperatures. These values are used to develop a first estimate on cost and emission savings, and improvements to occupant comfort. Due to the wide number of electrical and natural gas utilities captured across the combined 32 climate zones, cost and carbon emission calculations are based on average quantities provided through the U.S. Energy Information Administration (EIA) and Environmental Protection Agency (EPA). State average retail electricity and natural gas rates were taken from the 2020 values reported by EIA[130,131]. Electricity carbon emissions are based on the applicable 2020 eGrid subregion average carbon emission factor while natural gas emission factors are based on EPA natural gas combustion emissions[132,133].

Occupant comfort is estimated through the calculation of cooling degree days (CDD) for the building interior, which is described by Equation (1). This equation shows the CDD calculation for a single day where T_{max} and T_{min} are the maximum and minimum temperature experienced during a single day. The average of these values are compared to the reference temperature T_{ref}, which is set to 26.67°C, or 80°F. Annual CDD for the entire year is found by summing CDD for each day. CDD was selected as the comfort metric due to simplicity of use and widespread understanding across building energy practitioners. Recent work examining the impact of energy efficiency of occupant comfort [122] presented multiple methods for quantifying comfort. A common feature of these metrics is the summation of temperature exceedance or heat event occurrence only when a reference temperature has been exceeded. Since the CDD and other interior comfort metrics require this exceedance, we hypothesize that CDD will provide a sufficient first estimate towards the impact of a white coating towards occupant comfort.

$$CDD = max\left(\frac{T_{max} - T_{min}}{2} - T_{ref}, 0\right) \tag{6.1}$$

6.2.4 Statistical Analysis

The purpose of the statistical analysis is to generate high quality relationships between critical BEM outputs (energy use, comfort, etc.) and general model inputs. These types of relationships are immediately useful for rapidly estimating the efficacy of a white coating material in a climate with different properties other than what is captured in this work. The two processes used in this work to support this purpose are analysis is analysis of variance (ANOVA) coupled with linear regression.

For the purpose of this work, ANOVA was used to evaluate the null hypothesis between relevant factors (weather or building characteristics) and responses (electricity and gas load changes). The null hypothesis predicts that any correlation between a factor and response is purely due to coincidence, and no causal relation truly exists[134]. This is determined through calculation of the probability value (or p-value). Achieving a p-value of 0.05 or less suggests that there is a 5% chance that the null hypothesis is true. Once a series of factors have been found to have satisfactory p-values, linear regression is applied to develop the statistical relationship. A final qualitative filter was applied where engineering intuition was applied to ensure that any relationship could be physically explained.

The factors included in this analysis are average temperature values (whole year, winter, and summer), average relative and absolute humidity, average wind speed, average solar intensity during solar hours, climate zone, and climate letter. Response factors are electric energy and peak power savings, change in gas loads, and CDD reduction in buildings without space cooling. ANOVA and regression analyses were carried out using the Stat-Ease Design-Expert 12 software[135].

6.3 Building Energy Savings Analysis of White Coatings

The surface cooling capability of white coatings comes from its large solar reflectivity to reflect most of the sunlight, and high infrared emissivity to emit thermal radiation through atmospheric transmission window, as **Fig. 6.1a** shows. To investigate how much cooling white coatings could achieve if coated on building roofs, we apply the polymer coating based on hollow glass microspheres we developed in the previous work (labelled as "polymer coating") and the ideal coating with unity solar reflectivity and infrared emissivity (labelled as "ideal colling") to the roof of the midrise apartment reference model. Temperatures of the uncoated midrise apartment roof and coated roof are calculated. We select Los Angeles as the location since it is a representative city with a hot climate and large population. The hourly Typical Meteorological Year (TMY3) weather data[86] is used to obtain the hourly air temperature and solar intensity information. Uncoated and coated roof temperatures are compared with the air temperatures in winter (**Fig. 6.1b**) and summer (**Fig. 6.1c**). January 8th and July 1st is selected as the representative day in winter and in summer, respectively. A constant heat transfer coefficient of h=10 W/m^{2}K is assumed in the temperature predictions. Results show that roof temperature drops in both winter and summer.

The theoretical temperature reduction of polymer coatings is similar to the experimental findings we reported in our previous work. Ideal coatings lead to even larger surface cooling compared to polymer coatings since polymer coatings exhibit a small absorption in the solar region and less-than-unity emissivity in the infrared region.

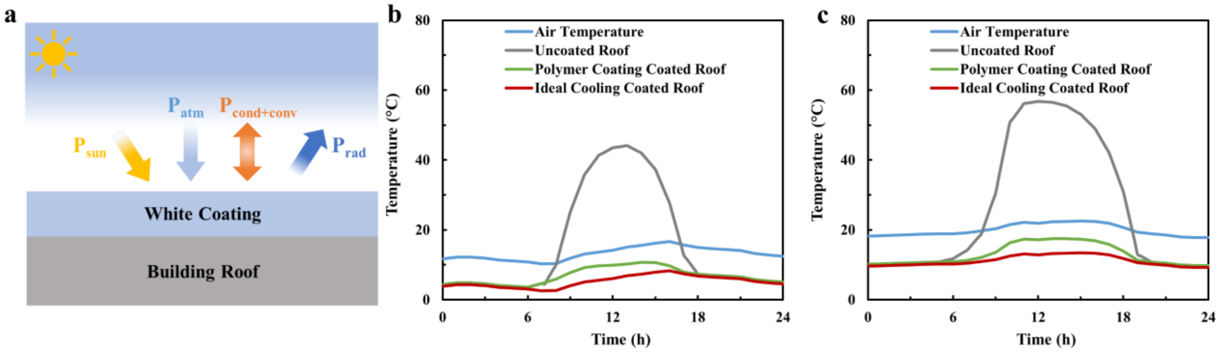

Figure 6.1 Cooling performance of white coatings on building roofs. (a) The schematic of heat transfer terms in the building roof with a layer of white coating on top; 24-hour temperature predictions between uncoated and coated roof by polymer coatings based on hollow glass microspheres and ideal cooler with unity solar reflectivity and infrared emissivity (b) on a normal winter day (January 8th is selected as the example) and (c) a normal summer day (July 1st is selected as the example) in Los Angeles. In the temperature prediction, the hourly ambient temperature and solar intensity information is from Typical Meteorological Year (TMY3) data in Los Angeles and a constant heat transfer coefficient of 10 W/m^2K is assumed.

Since roof temperatures are reduced significantly when white coatings are applied on building surfaces, cooling energy demand is reduced as well. We thus investigate annual cooling energy savings for midrise apartment model.

The prototype midrise apartment model is used to establish reference energy patterns and modified by adding white coatings onto exterior surfaces of models to generate modified energy patterns.

Fig. 6.2 provides results to characterized baseline BEM performance prior to white coating application for the 16 ASHARE and 16 CEC climate zone models. **Fig. 6.2a** and **Fig. 6.2b** presents the annual electricity use and annual natural gas use. We can see from the figures that there is a large variation for either electricity use or natural gas use across different cities in the US. Electricity is used for cooling, interior lightning, exterior lightning, interior equipment, and fan, while natural gas is mainly used for heating and water systems. **Fig. 6.2c** exemplifies the energy composition of electricity and natural gas for prototype midrise apartment building model in Los Angeles. The annual electricity use for cooling is 8.63 kWh/m^2 while the annual natural gas use for heating is 4.10 kBTU/m^2. In other cities, the electricity use for cooling and the natural gas use for heating varies significantly with different cooling and heating demand, resulting in large variations in annual electricity use and annual natural gas use.

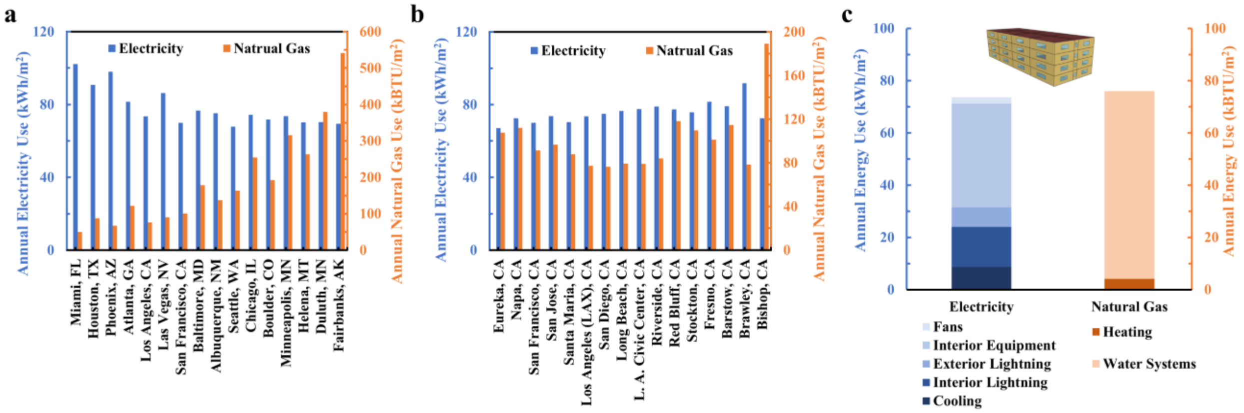

Figure 6.2 Energy use patterns of prototype midrise apartment building model. Annual electricity use and annual natural gas use for DOE prototype midrise apartment building model in (a) 16 representative cities in 8 ASHRAE climate zones and (b) 16 cities in 16 CEC climate zones in California; (c) Energy composition of electricity and natural gas for DOE prototype midrise apartment building model in Los Angeles. Inset is the façade of the DOE prototype midrise apartment building model. The annual electricity

use is presented in kWh/m^2 to the left y-axis while the annual natural gas use is presented in kBTU/m^2 corresponding to the right y-axis.

Annual cooling energy savings per area in ASHRAE (**Fig. 6.3a**) and CEC climate zones (**Fig. 6.3c**) for midrise apartment model are calculated and presented in **Fig. 6.3b** and **Fig. 6.3d** by comparing BEM annual cooling loads due to white coating application. The results indicate that annual cooling energy savings in national level climate zones range from 0.69-6.64 kWh/m^2 for ideal cooling and 0.62-5.79 kWh/m^2 for polymer coating, peaking in Phoenix, AZ. Considering CEC climate zones, electricity savings range from 1.38-5.80 kWh/m^2 for ideal cooling and 1.26-5.26 kWh/m^2 for polymer coating, peaking in Brawley. If we evaluate cooling energy savings in percentage, cooling loads are reduced by 17.71%-47.24% with the ideal coating, and 15.42%-43.26% using the polymer coating. Based on this current state-of-the-art polymer coatings can achieve 88.3%-91.7% of theoretical cooling energy savings.

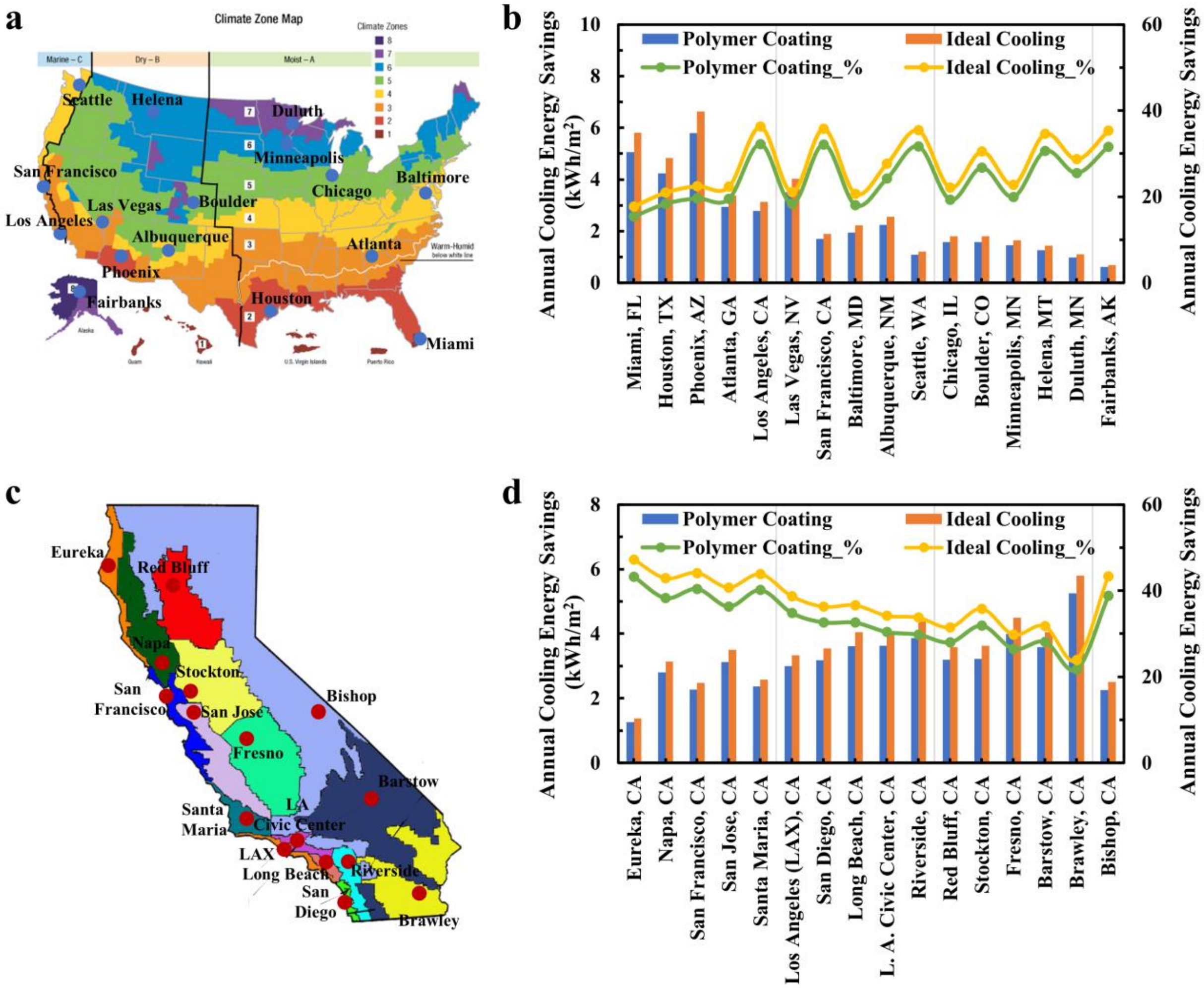

Figure 6.3 The annual cooling energy savings by white coatings for the midrise apartment in different locations. (a) Distribution map of 8 ASHRAE nation-level climate zones with 16 representative cities in the US and (b) annual cooling energy savings by polymer coating based on glass bubbles and ideal cooler for the midrise apartment in 16 cities. (c) Distribution map of 16 CEC climate zones with 16 representative cities in California and (d) annual cooling energy savings by polymer coating based on glass bubbles and ideal cooler for the midrise apartment in 16 cities. Annual cooling energy savings in percentage is also plotted to the right y-axis.

In addition to savings in cooling energy, the application of white coatings on exterior surfaces of buildings also lead to reduction in cooling peak load. Our calculations indicate a cooling peak load reduction of 3.80-6.84 kW (or 21.6%-50.0% peak cooling load) with ideal cooling and 3.29-6.47 kW (or 18.7%-42.7%) with polymer (**Fig. 6.4a** and **Fig. 6.4b**).

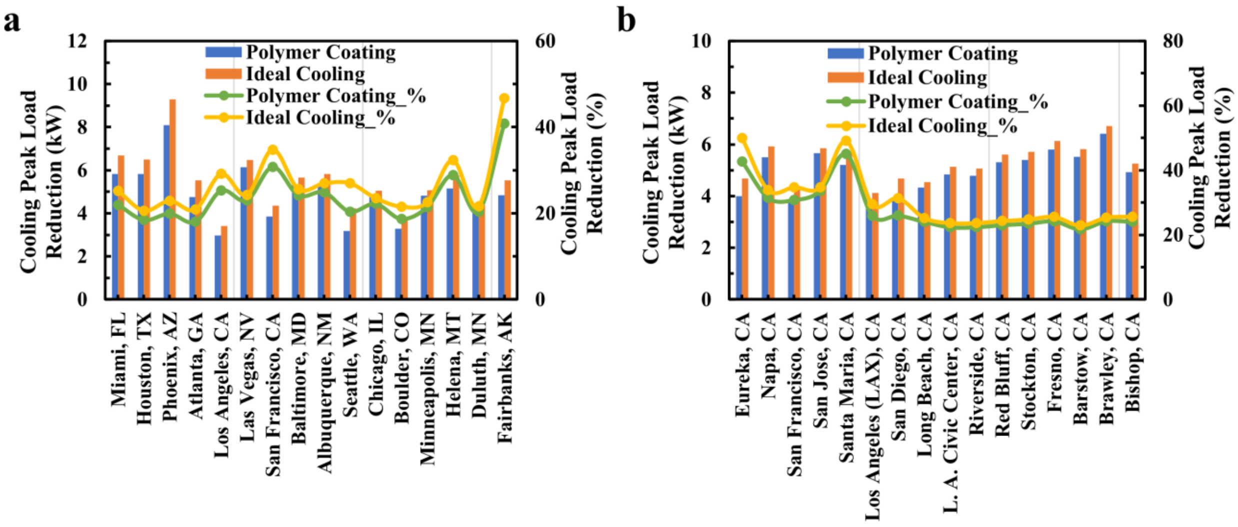

Figure 6.4 Cooling peak load reductions by white coatings in different locations. Cooling peak load reductions by polymer coating based on glass bubbles and ideal cooler for the midrise apartment in (a) 16 representative cities of 8 ASHRAE climate zones in the US and (b) 16 representative cities in 16 CEC climate zones in California. Cooling peak load reductions in percentage is also plotted to the right y-axis in both plots.

White coatings reduce surface temperatures and result in savings in cooling energy and electricity use. During the winter, however, white coatings lower exterior surface temperatures, resulting in higher interior heating loads. To investigate the negative effect brought by white coatings, we calculate the annual heating energy increase for ideal cooling and polymer coating. Ideal cooling leads to negative annual heating energy savings of 0.62-42.96 kBTU/m^2 for midrise apartment (**Fig. 6.5a** and **Fig. 6.5b**), while polymer coating results in negative annual heating energy savings of 0.47-36.90 kBTU/m^2. These results indicate that white coatings can bring more than double heating loads in warmer climates.

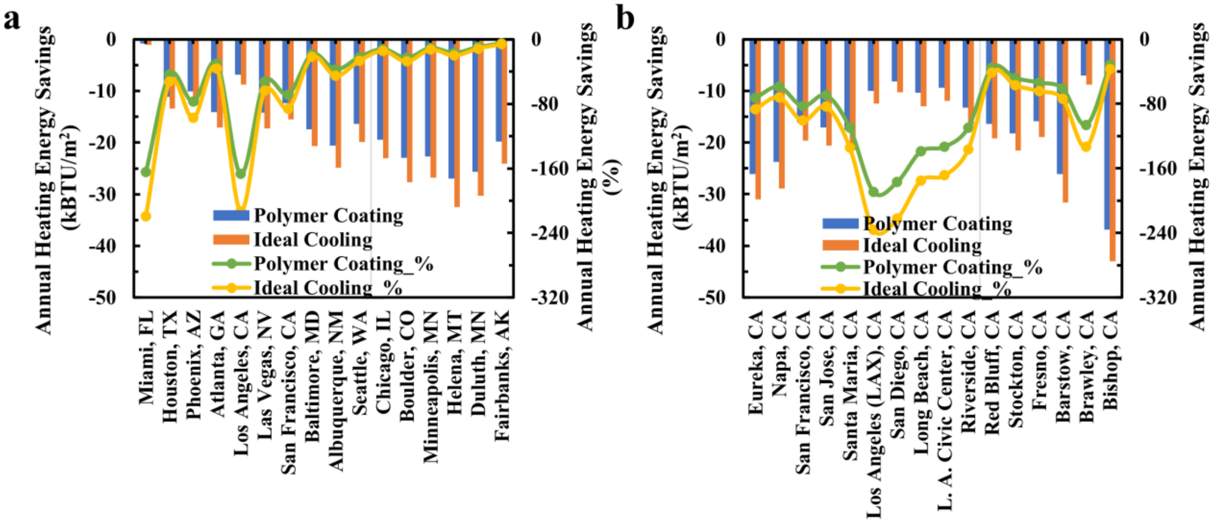

Figure 6.5 Annual heating energy savings by white coatings in different locations. Annual heating energy savings per area by polymer coating based on glass bubbles and ideal cooler for the midrise apartment in (a) 16 representative cities of 8 ASHRAE climate zones in the US and (b) 16 representative cities in 16 CEC climate zones in California. Annual heating energy savings in percentage is also plotted to the right y-axis in both plots.

6.4 Carbon Emission Savings and Utility Cost Savings by White Coatings

To better demonstrate the combination of net benefit of an ideal and a polymer white coating, we calculate total carbon dioxide (CO_2) emission including emission from electricity use and natural gas use. Since the white coating reduces electricity while increasing natural gas use, CO_2 emission savings from electricity use will be positive while emission savings from natural gas use will be negative. Total CO_2 emission savings will depend on local resource mix and can be viewed as an estimate towards the environmental benefit of the white coating used on apartment buildings.

According to our calculations, ideal cooling leads to an electricity CO_2 emission savings of 1309.92-15006.38 kg/year (**Fig. 6.6a**) and a natural gas CO_2 emission savings of -49.78 kg to -1467.82 kg year (**Fig. 6.6b**) for the 16 ASHRAE climate zones. For total CO_2 emission savings, Phoenix exhibits highest savings of 14428.11 kg while Fairbanks has the minimum savings of 219.59 kg (**Fig. 6.6c**). For the 16 CEC climate zones, Brawley has the maximum total CO_2 emission savings of 8835.51 kg and Eureka shows the minimum total CO_2 emission savings of 1061.91 kg (**Fig. 6.6d** to **Fig. 6.6f**). The result indicates that all cities we study have net positive CO_2 emission savings despite increasing natural gas use due to overcooling and corresponding additional heating energy demands.

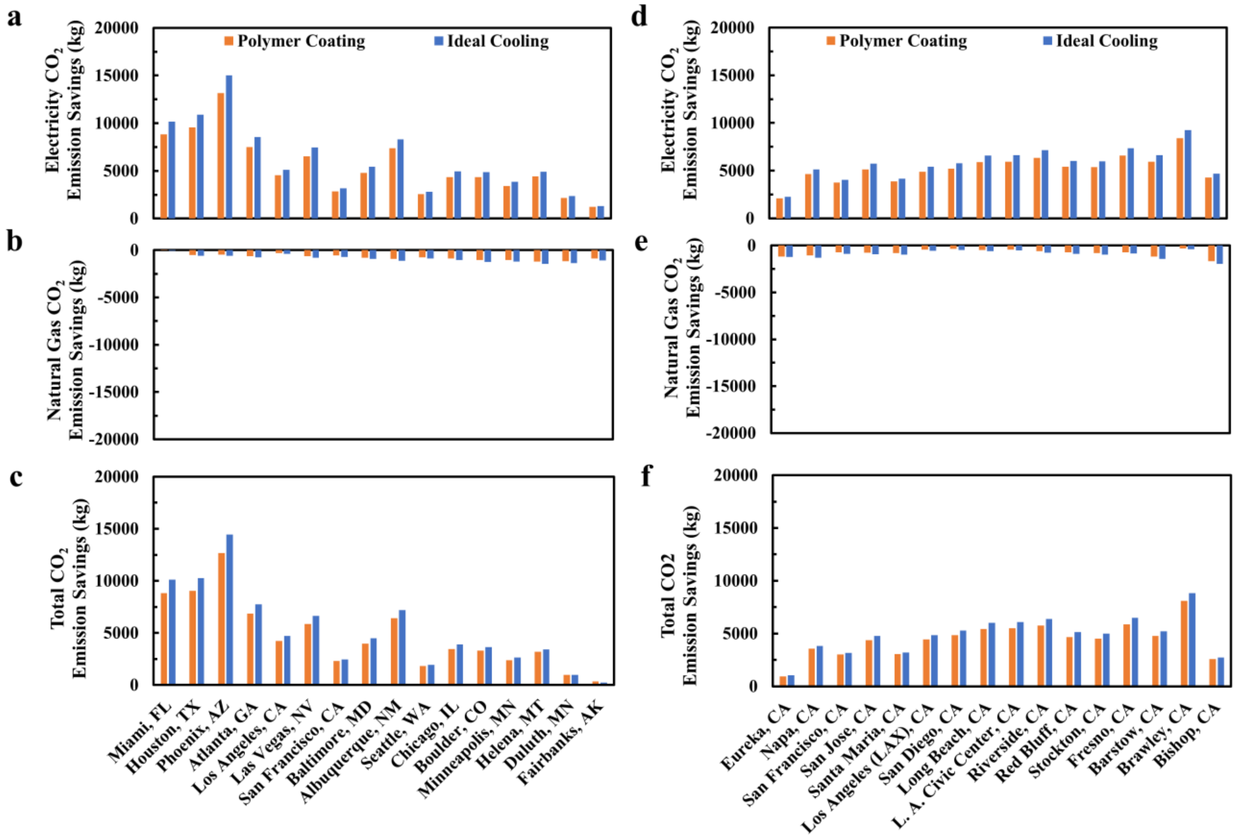

Figure 6.6 Annual carbon dioxide (CO_2) emission savings by white coatings in different locations. (a) Annual electricity CO_2 emission savings, (b) annual natural gas CO_2 emission savings and (c) total CO_2 emission savings for white coating modified midrise apartment in 16 representative cities in 8 ASHRAE climate zones in the US; (d) Annual electricity CO_2 emission savings, (e) annual natural gas CO_2 emission savings and (f) total CO_2 emission savings for white coating modified midrise apartment in 16

representative cities in 16 CEC climate zones in California. Total CO_2 emission is composed of CO_2 emission from electricity and natural gas. Fuel factors from previous publications are used to calculate CO_2 emissions from electricity use and natural gas use.

In addition to annual CO_2 emission savings calculations, we also conduct calculations of annual utility electricity and natural gas cost savings. **Fig. 6.7a** to **Fig. 6.7c** summarizes the annual electricity cost savings, annual natural gas cost savings, and annual utility cost savings in 16 ASHRAE climate zones. It is found that ideal cooling leads to annual electricity cost savings of 0.11 $\$/m^2$-0.84 $\$/m^2$ and annual natural gas cost savings of -0.02 $\$/m^2$ to -0.27 $\$/m^2$. If we sum up the electricity cost savings and natural gas cost savings, we can observe that some cities show positive annual utility cost savings while some cities have negative utility cost savings. For example, Miami and Phoenix both show high annual cost savings of 0.68 $\$/m^2$ and 0.67 $\$/m^2$, respectively. However, Duluth and Fairbanks both exhibit annual cost savings of -0.13 $\$/m^2$, indicating white coatings are not economically preferred in these cities since the increased heating loads offset any electricity savings. **Fig. 6.7d** to **Fig. 6.7f** lists annual electricity savings, annual natural gas cost savings and annual utility cost savings in 16 CEC climate zones and we find that most of the cities exhibit positive annual utility cost savings except for Eureka. Ideal cooling leads to an annual utility cost saving of -0.06 $\$/m^2$ in Eureka while it results in positive annual cost savings in other 15 cities, peaking in Brawley (1.16 $\$/m^2$). These results indicate that white coatings are preferred on building surfaces in hot climates to save CO_2 emissions and utility cost despite the negative effect of increased natural gas use.

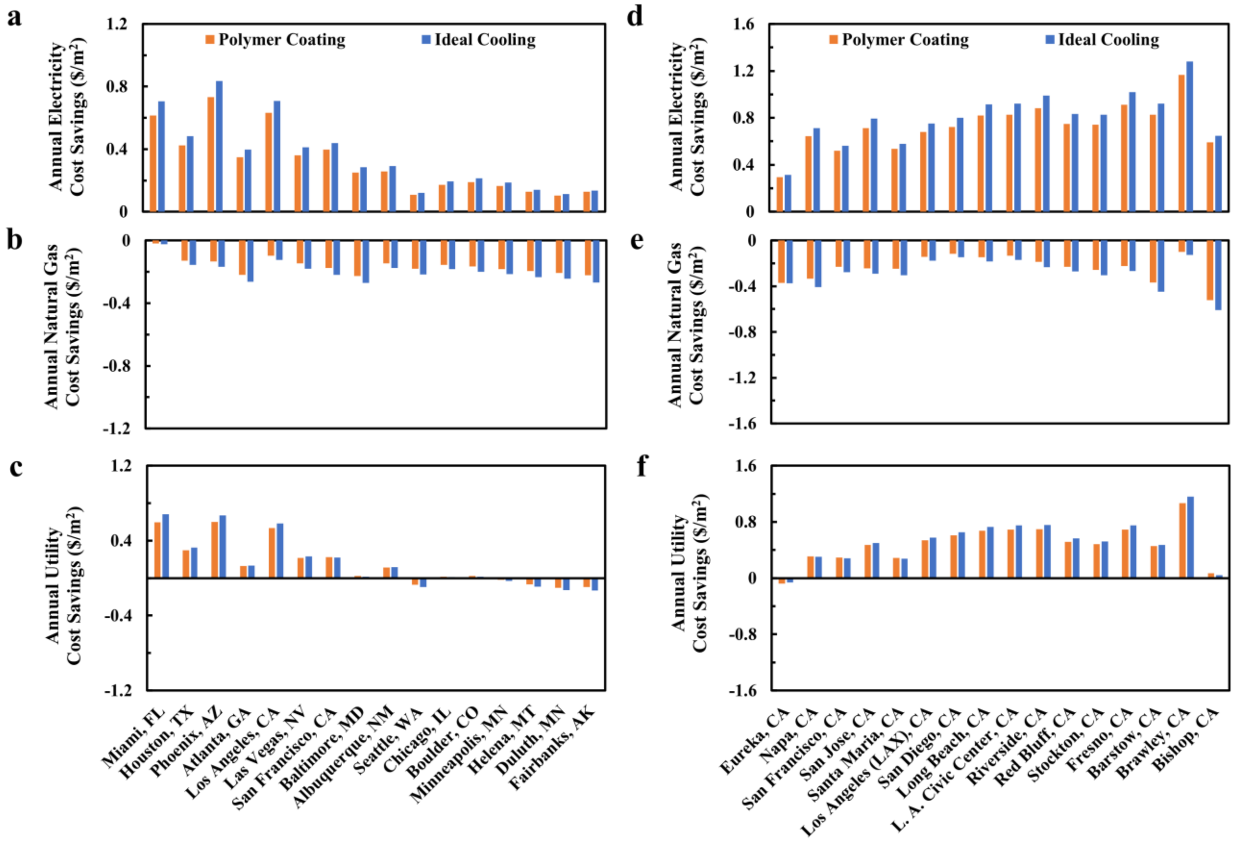

Figure 6.7 Annual utility cost savings by white coatings in different locations. (a) Annual electricity cost savings, (b) annual natural gas cost savings and (c) annual utility cost savings for white coating modified midrise apartment in 16 representative cities in 8 ASHRAE climate zones in the US; (d) Annual electricity cost savings, (e) annual natural gas cost savings and (f) annual utility cost savings for white coating modified midrise apartment in 16 representative cities in 16 CEC climate zones in California. Annual utility cost is composed of electricity cost and natural gas cost. Electricity price and natural gas price information is obtained from the US Energy Information Administration website.

Considering the calculation results that total carbon emission savings by both ideal cooling and polymer coating are positive in all ASHRAE and CEC climate zones, white coatings shows great capability to reduce carbon emissions if applied to building surface. White coatings also lead to positive utility cost savings in climate zones with high ambient temperatures while the cost of white coating materials are relatively low (0.39 \$/m^2) compared to its cost savings for buildings. Despite the negative effects of heating demand increase, white coatings present very promising carbon emission and cost savings for building sections especially in areas with hot climates.

6.5 Cooling Degree Days Reduction for Buildings with Limited Cooling Systems

Since white coatings shows significant temperature reduction when coated on building roofs, one of the most promising applications for white coatings is the surface cooling in buildings with limited or no air-conditional systems. To evaluate how much cooling ideal cooling or state-of-the-art white coatings can achieve in buildings with no air-conditioning or cooling systems, we modify the prototype midrise apartment model by disabling its cooling system and simulate interior temperatures before and after white coating applied on the roof.

The interior temperature comparison before and after ideal cooling and polymer coating in Phoenix in the first week of July is shown in **Fig. 6.8a** below. The interior temperature reaches 42°C at noon before the application of white coatings. The application of the ideal cooling and polymer coating reduces peak interior temperatures by 5°C and 4°C, respectively. The same method is applied to other 29 cities as well and we investigate the cooling effect of white coatings by calculating the cooling degree days reductions. We find that ideal cooling results in a cooling degree days reduction of 9.38-630.43 CDD in all cities we study and polymer coating leads to a cooling degree days reduction of 9.38-554.75 CDD (**Fig. 6.8b**). For example, the cooling degree days in Brawley decreases from 1879.49 CDD to 1249.06 CDD with ideal cooling applied to buildings without any cooling systems. Cooling degree days reductions in all cities are increased by applying ideal cooling or polymer coating compared to calculations using average interior temperature. For instance, the cooling degree days in Brawley decreases from 2313.56 CDD to

1521.29 CDD, with a reduction of 792.27 CDD with ideal cooling. White coatings can improve the thermal comfort of building interiors.

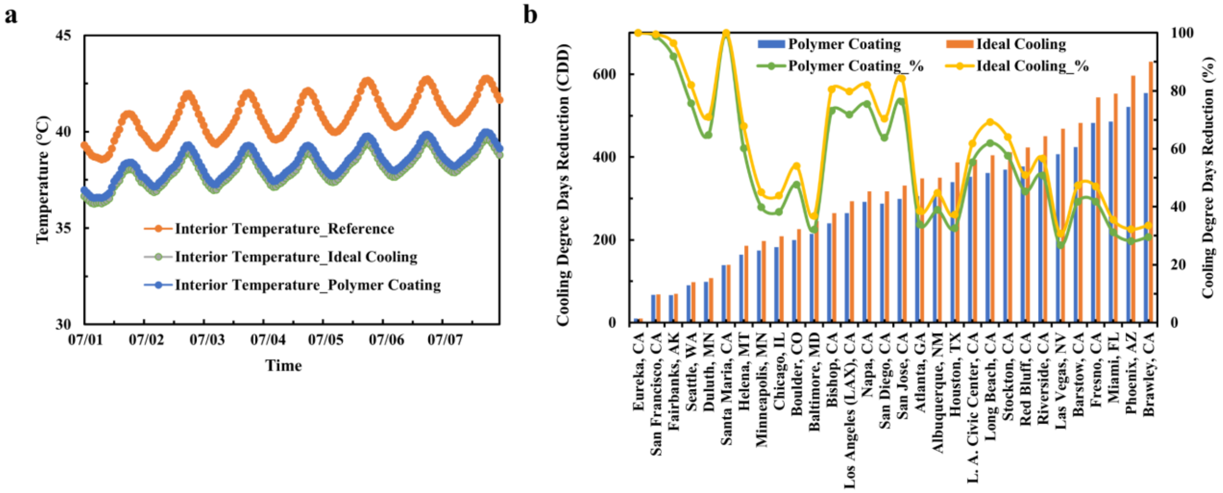

Figure 6.8 Thermal comfort benefits of white coatings for buildings without cooling systems. (a) Interior temperature reduction by white coatings for midrise apartment without cooling systems in the first week of July in Phoenix; (b) Cooling degree days reduction based on average interior temperatures by polymer coating and ideal cooling for midrise apartment without cooling systems in 16 representative cities in 16 CEC climate zones in California and 14 representative cities across 8 ASHRAE climate zones in the US. Cooling degree days is the summation of degrees of the average interior temperature per day above 80F for the year. Cooling degree days reduction in percentage is also plotted to the right y-axis for each city.

6.6 Statistical Analysis

BEM simulation and post-processing results used in ANOVA were used “as is” without any type of data transformation or mapping. The most significant and statistically strong relationship was found between cooling energy savings and a linear combination of climate zone, average summer temperature, and average wind speed. The linear regression using these three factors is shown in Equation (6.2). Since climate zone is a categorical factor, individual correlations were developed for each individual climate zone. The climate zone is captured through the equation scalar, which decreases as climate zones get colder. For all equations, a higher summer temperature increases and wind speed decrease electricity savings potential.

$$e_{Cooling\ Savings} = \begin{cases} 3.280 + 0.1410 \cdot T_{Summer\ Avg.} - 0.3418 \cdot \bar{U}_{wind}, if\ CZ = 1 \\ 2.374 + 0.1410 \cdot T_{Summer\ Avg.} - 0.3418 \cdot \bar{U}_{wind}, if\ CZ = 2 \\ 1.514 + 0.1410 \cdot T_{Summer\ Avg.} - 0.3418 \cdot \bar{U}_{wind}, if\ CZ = 3 \\ 0.409 + 0.1410 \cdot T_{Summer\ Avg.} - 0.3418 \cdot \bar{U}_{wind}, if\ CZ = 4 \\ 0.152 + 0.1410 \cdot T_{Summer\ Avg.} - 0.3418 \cdot \bar{U}_{wind}, if\ CZ = 5 \\ 0.0335 + 0.1410 \cdot T_{Summer\ Avg.} - 0.3418 \cdot \bar{U}_{wind}, if\ CZ = 6 \\ -0.204 + 0.1410 \cdot T_{Summer\ Avg.} - 0.3418 \cdot \bar{U}_{wind}, if\ CZ > 6 \end{cases} \quad \left(\frac{kWh}{m^2 year}\right) \qquad (2)$$

This curve fit is demonstrated in detail in Figure 9. This figure shows the application of Equation (6.2) across difference climate zones (**Fig. 6.9a**) for a high and low average summer temperature, the application of the equation for two different climate zones versus varying average summer temperature (**Fig. 6.9b**), and the actual versus predicted electric energy savings based on Equation (6.2) (**Fig. 6.9c**). In total, the description of cooling savings using a linear combination of these two factors achieves a high R^2 value over 0.9. Additional analysis shows that average solar intensity has a significant relationship with electricity savings. However, this factor was excluded since inclusion of solar intensity provides minimal model accuracy benefits – addition of solar intensity boosts R^2 from 0.9575 to 0.9671.

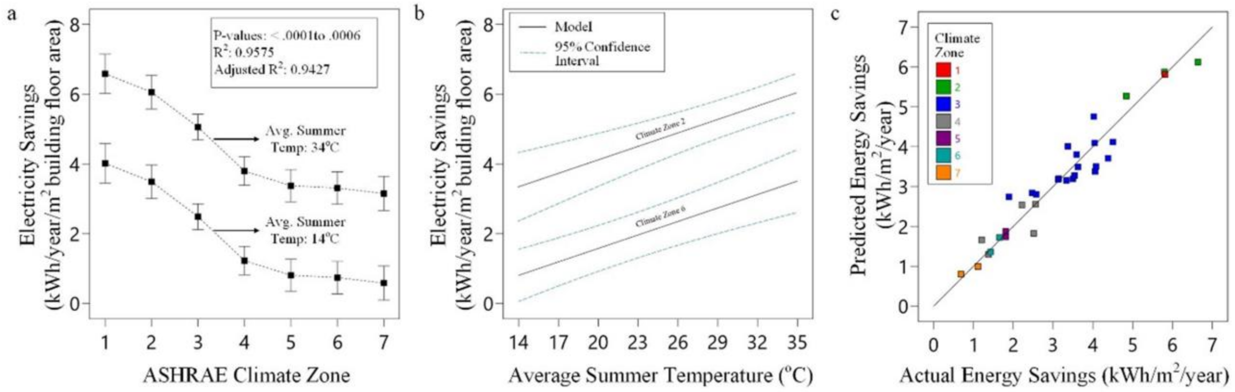

Figure 6.9 Details of the ANOVA analysis examining the relationships between general model inputs and annual electricity savings due to the application of the white coating. ANOVA analysis shows that climate zone, average summer temperature, and average wind speed data are significant factors and can be used to generate a predictive equation that matches simulation results with an R^2 of 0.9575. All subplots show model results using an average wind speed of 3 m/s (a) The predictive equation applied to seven different climate zones for an average summer temperature of 14^{o}C and 34^{o}C. As expected, the equation predicts much higher electricity savings in warmer climate zones. (b) The predictive equation as a function of average summer temperature for Climate Zones 2 and 6. (c) Average versus predicted energy savings based on the input data, confirming the strong correlation based on the climate zone and average summer temperature factors.

For peak electric load reduction, only average summer temperature has a p-value less than 0.05. The curve fit for this response-factor pair is shown in Equation (6.3). This fit is plotted in **Fig. 6.10a**. The comparison of actual versus predicted load reduction for this model is shown in **Fig. 6.10b**. In total, using average summer temperature achieves a relatively low R^2 correlation of 0.5375, indicating that the current best curve fit is insufficient for predicting peak cooling load. This is apparent in Fig. 10b, which shows a nearly equal spread of over- and underestimated data. We believe that this result is primarily due to the complex physical interaction between building energy systems and occupants captured in complete BEMs. Peak load depends on the coincidence use of multiple building energy systems, many of which depend on occupant behavior. If this behavior does not line up with peak cooling demand, then weather and climate zone information are insufficient for predicting peak load reduction.

$$P_{Peak\ Reduction} = 1.808 + 0.1622 \cdot T_{Summer\ Avg.} \quad (kW) \tag{6.3}$$

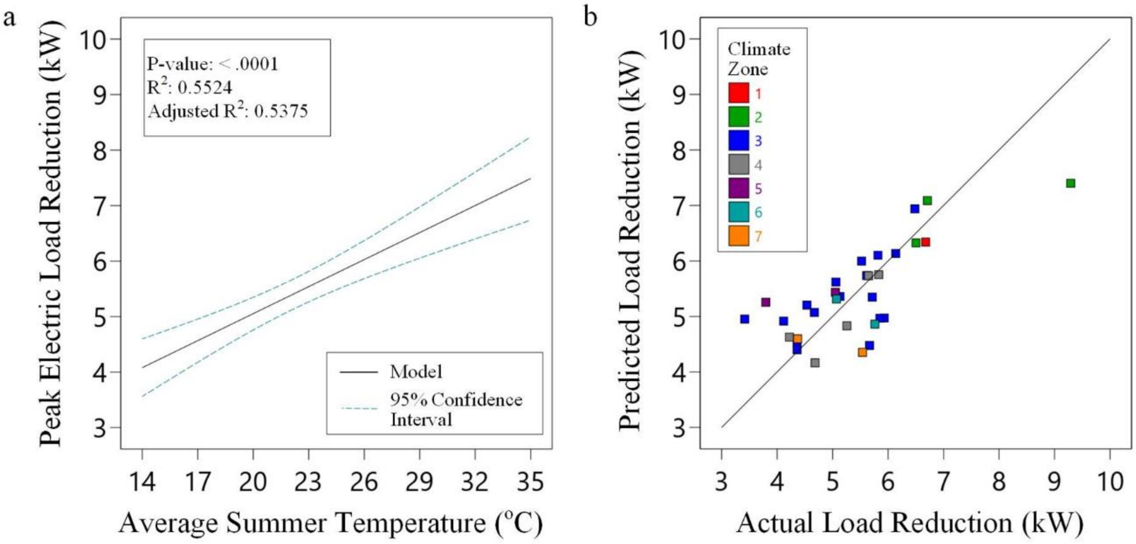

Figure 6.10 Details of the ANOVA analysis on the relationship between average summer temperature and peak load reduction. The overall quality of fit is relatively low at an R^2 of 0.5524. Since inclusion of other factors result in p-values exceeding 0.005, other factors are required to improve the current model. (a) The predictive load reduction equation as a function of average summer temperature. (b) Actual versus predicted load reduction classified by climate zone type. Results indicate that over and underestimations of actual load reductions occur within similar climate zone types.

In contrast with prior results, gas load increase was found to correlate best and hold a significant relationship with a 2nd order curve fit. The equation, shown with Equation (6.4), shows a relationship between average summer temperature, winter temperature, and solar intensity. The

2nd order is achieved through the multiplication of average winter temperature and solar intensity. This curve fit is shown in Figure 11 where **Fig. 6.11a** shows the curve fit at a constant winter temperature of 1.23^{o}C, **Fig. 6.11b** shows the curve fit at a constant summer temperature of 24.2^{o}C, and a comparison of actual versus predicted gas load increases in **Fig. 6.11c**.

$$e_{Gas\ Heating\ Increase} = -3.428 + 0.584 \cdot T_{Summer\ Avg.} - 1.658 \cdot T_{Winter\ Avg.} + 0.070 \cdot P_{Avg\ Solar\ Intensity} + 0.0051 \cdot T_{Winter\ Avg.} \cdot P_{Avg\ Solar\ Intensity} \quad \left(\frac{kBtu}{m^2 year}\right) \tag{6.4}$$

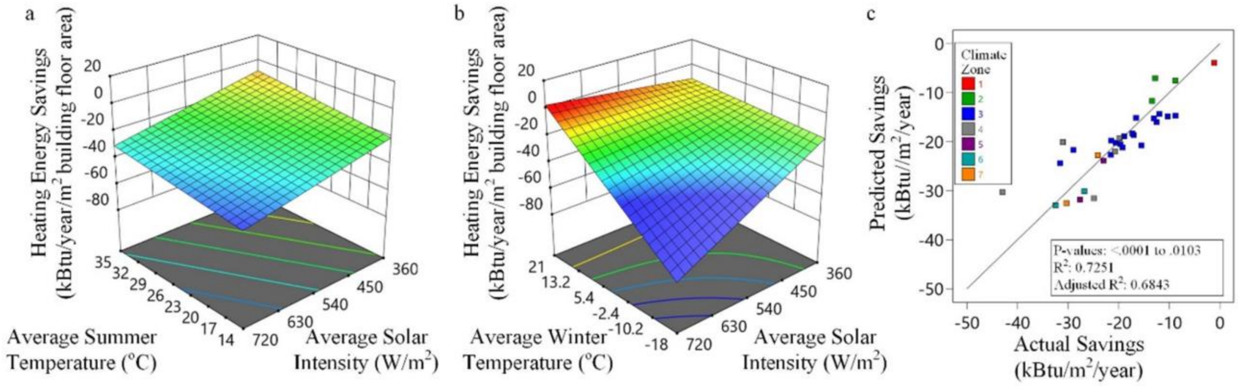

Figure 6.11 Details of the ANOVA analysis on predicting heating load increase. Testing parameters showed that a second order model that considers the interaction between winter temperature and average solar intensity achieves the highest level of accuracy while maintaining acceptable p-values. The resulting function combines impacts from both summer and winter weather patterns, and level of solar intensity and achieves an R^2 of 0.7251. (a) The predicted gas load increase as a function of average summer temperature and solar intensity when average winter temperature is held at 1.23^{o}C. (b) The predicted gas load when average summer temperature is set to 24.2^{o}C. (c) Predicted versus actual gas load increases.

The various factors included in this curve fit all have reasonable physical interpretations. Average summer temperature appears as a significant term in part due to the structure of the building energy models. These models tend to have consistent thermostat settings throughout a year, resulting in potential heating operation in the summer if interior temperatures fall below a heating setpoint. In practical buildings, this heating operation may be disabled by building operators or occupants who wish to avoid heating their building or residence prior to a warm summer day. Average winter temperature has an obvious relationship with heating loads where buildings in colder climates require more heating. Solar intensity has a similar relationship with building heating loads. Solar gain across a building can reduce heating load, meaning that the white coating has a stronger effect on increasing building heating in regions with higher solar intensity. This relationship suggested that the combination of average winter temperature and solar intensity have compounding effects on building heating loads.

In total, this correlation achieves an R^2 value of 0.7251, meaning that other excluded factors are needed to further improve the correlation. This relationship also has the highest p-values of all factor-response sets, in part due to the inclusion of higher order terms. Excluding the 2nd order term reduces p-value terms, but at the expense of a drop in R^2 value down to approximately 0.5.

CDD reduction in buildings without space cooling equipment is described in Equation (6.5). ANOVA shows that CDD reduction has causal relations with average summer temperature, solar intensity, and wind speed. In concept, CDD reduction is driven by the same physical factors as electricity reduction captured in Equation (6.2). However, the p-value associated with climate zone is 0.07 or higher, decreasing the reliability of any associated curve fit.

$$\begin{aligned} CDD_{Reduction} &= 339 - 24.1 \cdot T_{Summer\ Avg.} - 0.476 \cdot P_{Avg\ Solar\ Intensity} \\ &\quad + 45.45\ 0.0051\ \cdot \overline{U}_{wind} \qquad (CDD) \end{aligned} \tag{6.5}$$

Regardless, the factors included in Equation (6.5) have strong physical connections with CDD reduction and combine to achieve a high R^2 value. First, buildings in warm climates have the highest interior temperatures, increasing the number of CDD that can be reduced. Second, the white coating reflects incoming solar radiation, reducing CDD by reducing solar gain across opaque building surfaces. Third, experimental results have shown the white coating can reduce surface temperature below ambient temperatures. Higher wind speed results in enhanced convection to the white coating surface. Instead of continued rejection of building thermal energy, the net energy flow is reversed and the white coating surface is warmed.

The model described in Equation (6.5) is shown in Figure 12. **Fig. 6.12a** shows the change in CDD versus average summer temperature and solar intensity at an average wind speed of 3 m/s. **Fig. 6.12b** shows change in CDD versus average summer temperature and wind speed for an average solar intensity of 540 W/m^2. **Fig. 6.12c** shows the general performance of the curve fit by showing the predicted change in CDD versus actual.

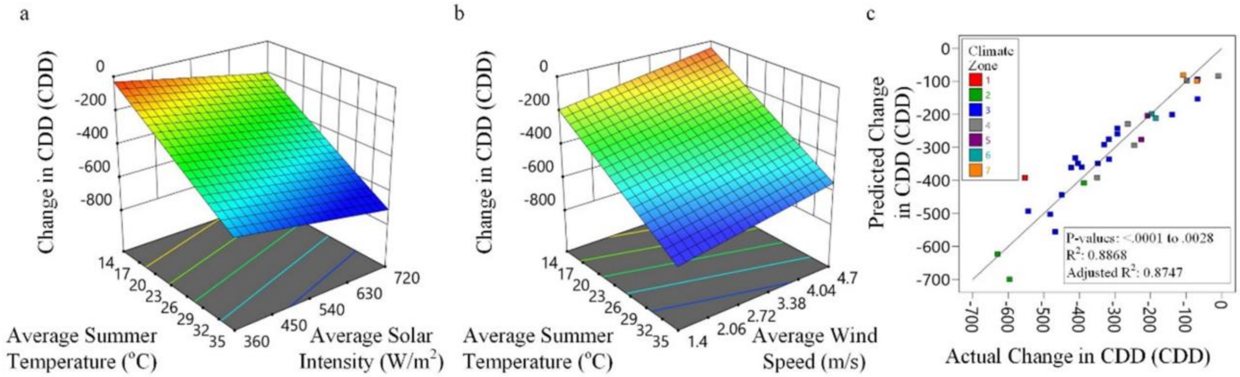

Figure 6.12 Details of the ANOVA analysis on CDD reduction in buildings without space cooling equipment. Critical parameters were found to be average summer temperature, solar intensity, and wind speed. The resulting linear regression produced a model that matches simulation results with an R^2 of 0.8868. (a) The modeled CDD reduction versus average summer temperature and solar intensity when average wind speed is 3 m/s. (b) The modeled CDD reduction versus average summer temperature and wind speed when solar intensity is 540 W/m^2. (c) The predicted versus actual CDD reduction.

6.7 Conclusions

To sum up, we evaluate the energy saving performance, corresponding CO_2 emission savings and utility cost savings of ideal white coatings with assumed unity solar reflectivity and infrared emissivity and state-of-the-art white coatings based on hollow glass microspheres using the prototype midrise apartment building model. With around 40°C and 20°C roof temperature reduction at noon in summer and in winter, respectively, ideal cooling results in annual cooling energy savings of 0.69-6.64 kWh/m^2 in 16 cities across ASHRAE climate zones across the US and 16 cities in CEC climate zones in California. It also offers a cooling peak load reduction of 3.80-9.29 kW in different cities and a negative effect of annual heating energy increase of 1.10-42.96 kBTU/m^2. To evaluate both positive effect of cooling energy savings and negative effect of heating energy increase, we calculate annual total CO_2 emission savings and annual utility cost savings and find that ideal cooling result in positive annual CO_2 emission savings in all cities in this study. The annual utility cost savings are positive in some cities with hot climates while they are negative in some cities with cold climates, indicating that white coatings are preferred on building surfaces with hot climates. Our calculation shows that ideal cooling leads to an interior temperature reduction of 5°C at noon in summer of Phoenix for buildings with no cooling systems, addressing cooling issues for buildings with limited or no reliable space cooling. The application of ideal cooling could result in a cooling degree days reduction of up to 630 CDD for buildings without cooling systems, bringing much thermal comfort to people living inside. The benefits of white coatings on carbon emission savings, utility cost savings and CDD reductions in many cities especially in hot climates can motivate us to apply such white coatings in buildings to address the cooling issues and save worldwide energy consumption.

We also use ANOVA approach to evaluate the contributions of ambient variables to different energy saving performance with ideal white coatings. The annual electricity savings in different climate zones can be mostly explained by average summer temperature and average wind speed, which gives a high correlation of coefficient R^2 of 0.9575. For cooling peak load reduction, average summer temperature gives a R^2 of 0.5375, indicating the current variables are insufficient to predict the reduction in peak cooling load in different locations. We found that the heating energy increase correlates with average summer temperature, winter temperature and solar intensity with a 2nd order curve fit and a R^2 of 0.6843, indicating the combination of average summer/winter temperature and solar intensity have compounding effects on building heating loads. As for buildings without cooling systems, the combination of average summer temperature, solar intensity and wind speed gives a R^2 of 0.8747 and shows strong physical connections with CDD reductions. believe this study helps people to understand the energy savings, carbon emission savings, and cost savings potential of white coatings and benefit future radiative cooling study in building thermal management applications.

Chapter 7 Conclusions and Suggestions

7.1 Summary

In this dissertation, we describe the use of hollow microspheres in white coatings for the surface cooling application in buildings. Hollow glass microspheres and Y_2O_3 hollow microspheres are studied and integrated with different binders for white coatings with high solar reflectivity and infrared emissivity to reduce surface temperature, thus leading to passive cooling and significant energy savings in buildings.

The solar reflectivity of solid and hollow microspheres are studied with 2D FDTD simulations. Our analysis shows that hollow microspheres with a thinner shell are more effective in scattering light compared solid microspheres. The high scattering efficiency, owing to the refractive-index contrast and large interface density, in hollow microspheres allows low-refractive-index materials to have a high solar reflectivity. When the diameter is varying, the random distributed 0.5-1 µm SiO_2 hollow microspheres provide the largest solar reflectivity. The weighted solar reflectivity increases with increasing refractive index and enlarges with a smaller extinction coefficient because of weaker solar absorption, which provide the guideline for material selections for broadband perfect solar reflectivity. Our study indicates ceramic materials with the combination of high refractive index and low extinction coefficient values such as Y_2O_3 are promising candidates. This work helps to identify the desired optical constants to achieve a broadband perfect solar reflectivity when combined with the hierarchical hollow microsphere designs and provides a material selection guidance for pigment-embedded polymeric materials. (chapter 2)

The low-cost and scalable cool white polymer coating with a controlled concentration of hollow glass microspheres can have the solar reflectivity of 0.92 and the mid-IR emissivity of 0.85, which leads to significant radiative cooling. The outdoor temperature measurement shows that 70 vol% polymer coating on a concrete surface helps to achieve a maximum temperature drop of 25 °C compared to the bare concrete block and exhibits a maximum sub-ambient cooling of 9 °C during the daytime with limited convective and conductive heat transfer. The building energy consumption analysis based on seven common building models in Los Angeles indicates that the annual cooling energy savings could be achieved from 2 MJ/m^2 to 12 MJ/m^2 by using the 70 vol% polymer coating on the exterior surface and the savings are more significant for higher surface area-to-volume buildings. The associated annual cost savings and annual CO_2 emission savings for representative buildings in Los Angeles are predicted to range from \$0.05/m^2 to \$0.58/m^2 and 0.26kg/m^2 to 1.45kg/m^2, respectively. The techno-economic analysis shows that the material costs for our cool white polymer coatings is estimated to be \$0.39/m^2 and \$0.005/W. This work opens the possibility of using such polymer-based coatings in large-scale surface cooling for modern buildings and pave the way towards energy-efficient buildings to reduce energy consumption. (chapter 3)

We have already successfully prepared the sprayable white coating samples using the KBr binder and hollow glass microspheres, with a simple spray coating method. The white coating samples can be fabricated with various substrates, different shapes, or dimensions. Our optical measurements show that the spray coating samples with KBr binders exhibits high reflectivity throughout the whole solar region due to high solar transparency of KBr, and high emissivity in the infrared region. Solar reflectivity of white coating increases from 0.92 to 0.96 when replacing Polydimethylsiloxane (PDMS) with KBr as the binder since reflectivity in the near-infrared region is much enhanced. The net cooling power of the sprayable white coating is calculated to be 96 W/m^2 when assuming a solar intensity of 1000 W/m^2 and a constant ambient temperature of 25°C.

The solar reflectivity increases from 0.90 to 0.97 with increasing thickness from 1 mm to 4 mm. Our temperature measurement results shows that the spray coating leads to lower surface temperature compared to commercial white paint when coated on commercial wood substrate. The inexpensive sprayable white coating with solar transparent binders provides a promising solution to improve reflectivity of white paints across the whole solar region and helps to resolve cooling issues for buildings with insufficient cooling systems. (chapter 4)

We evaluate the energy saving performance, corresponding CO_2 emission savings and utility cost savings of ideal white coatings with assumed unity solar reflectivity and infrared emissivity and state-of-the-art white coatings based on hollow glass microspheres using the prototype midrise apartment building model. To evaluate both positive effect of cooling energy savings and negative effect of heating energy increase, we calculate annual total CO_2 emission savings and annual utility cost savings and find that ideal cooling result in positive annual CO_2 emission savings in all cities in this study. The annual utility cost savings are positive in some cities with hot climates while they are negative in some cities with cold climates, indicating that white coatings are preferred on building surfaces with hot climates. The application of ideal cooling could result in a cooling degree days reduction of up to 630 CDD for buildings without cooling systems, bringing much thermal comfort to people living inside. The ANOVA approach is used to evaluate the contributions of ambient variables to different energy saving performance with ideal white coatings. This work helps people to understand the energy savings, carbon emission savings, and cost savings potential of white coatings and benefit future radiative cooling study in building thermal management applications. (chapter 6)

7.2 Suggestions for Future Work

7.2.1 Optical Property Modulation using Stretchable PDMS/Glass Composites

Although several white coatings based on hollow glass microspheres and Y_2O_3 hollow microspheres to achieve high solar reflectivity and infrared emissivity has been investigated or proposed, they exhibit unchanged optical properties under any circumstances. From the building energy savings analysis, we notice that high solar reflectivity in white coatings is not desired in winter days since they decreases the temperatures and thus increase the heating energy consumption. It makes us believe that white coatings with tunable optical properties might be an interest, which can also be called smart windows. Here we propose the stretchable selective emitter using PDMS and glass microspheres.

Fig. 7.1 is a schematic showing how the PDMS/Glass microsphere composite is fabricated. Glass microspheres are dispersed in isopropyl alcohol (IPA) solutions and supersonic is used to make the dispersion more uniform. The mixture is poured into a container such as a petri dish to let IPA evaporate under the ambient temperature. The silicone elastomer base and curing agent (Sylgard 184, from Dow Corning) is mixed with a 10:1 weight ratio in a vial to make polydimethylsiloxane (PDMS), with a weight ratio of 0.32% Triton-X100 added to make PDMS more stretchable. After thorough stirring and degassing, the prepared PDMS is added into the petri dish with glass microspheres in the bottom. The composite can be peeled off from the petri dish after curing for 24 hours in the ambient environment.

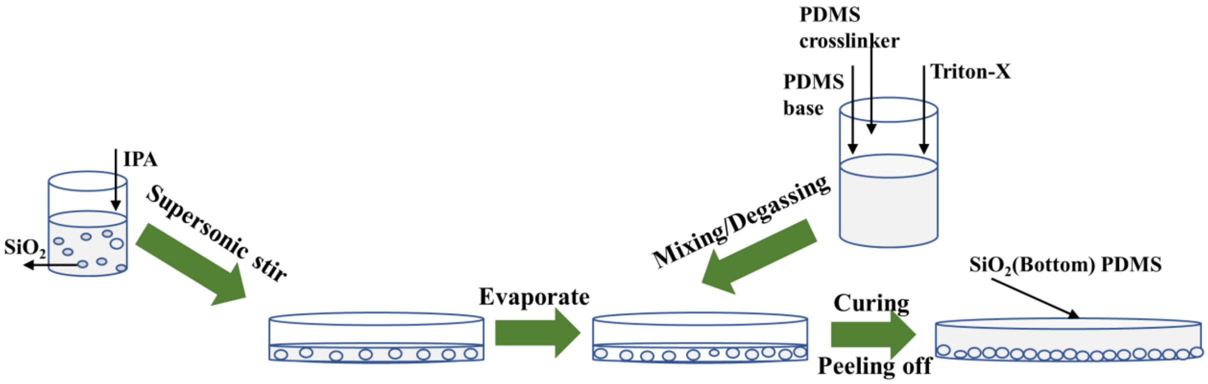

Figure 7.1 The schematic of the fabrication process of stretchable selective emitters based on PDMS and glass microspheres.

7.2.2 Surface Textured Polymer Coating for Infrared Emissivity Enhancement

Previously demonstrated optical properties of polymer coatings based on hollow glass microspheres and PDMS indicate an average mid-infrared emissivity of 0.85, which contributes to a significant temperature reduction of around 20 °C when coated on the concrete surface and a cooling power of 78.2 W/m^2. However, the infrared emissivity limits the further enhancement of the cooling power of the material. It is reported that surface texturing helps to enhance the mid-infrared emissivity of PDMS and opens up the possibility to enhance the cooling performance of polymer coatings based on PDMS.

As an example, we first introduce micro-pyramid-like structures on the surface of PDMS or polymer coatings with hollow glass microspheres as shown in the inset in **Fig. 7.2a** and use numerical simulations to find out its effect in mid-infrared emissivity enhancement. We use the FDTD simulations with various X_{span} and Z_{span} values. It is found that the mid-infrared emissivity increases as the aspect ratio increases, for different X_{span} values (**Fig. 7.2a**). The optimized textured polymer coating with hollow glass microspheres indicate a near-unity emissivity in the wavelength region of 6-16 μm (**Fig. 7.2b**). We further fabricate surface textured PDMS and polymer coatings with hollow glass microspheres using surface textured silicon wafer as the mold, with an average X_{span} of 13 μm. Optical measurements in the infrared region show that surface textured polymer coating with hollow glass microspheres has a higher averaged emissivity in the infrared wavelength region between 6-16 μm, compared to the flat polymer coating. Temperature predictions using a constant heat transfer coefficient of 10 W/m^2K indicate a temperature reduction of 0.2°C in the surface textured polymer coating and a temperature reduction of 1.5°C in the optimized textured polymer coating, compared to the flat polymer coating (**Fig. 7.2c**). The temperature reduction effect is also validated using the outdoor temperature measurement to compare temperatures of the bare concrete, the flat-polymer-coating-coated concrete, and the textured-polymer-coating-coated concrete under solar irradiations. It is noticed that the temperature of the textured-polymer-coating-coated concrete is 0.32°C lower than that of the flat-polymer-coating-coated concrete, under the peak solar intensity of 700 W/m^2 at noon. The results exemplify the potential of such surface textured polymer coatings in surface cooling for building applications.

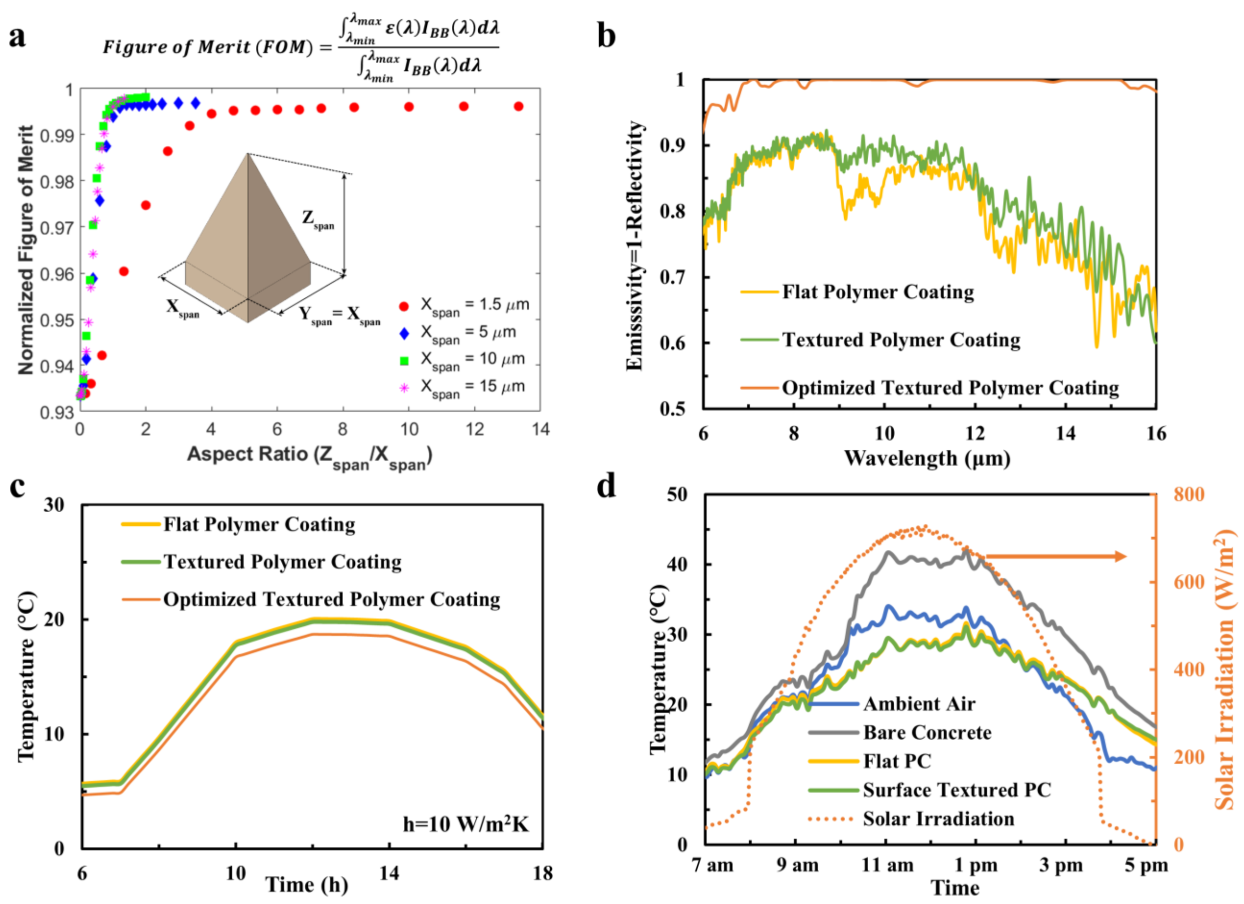

Figure 7.2 Surface textured polymer coating based on micro-pyramid-like surface textures. (a) FDTD simulation results of mid-infrared emissivity in micro-pyramid-textured polymer coatings. A figure of merit is defined to calculate the capability of the surface to emit thermal radiation. The inset shows the schematic of the micro-pyramid structure on the surface; (b) FTIR optical measurements of the flat polymer coating and the textured polymer coating, along with numerically optimized textured polymer coating in the wavelength region of 6-16 μm; (c) Temperature predictions of the flat polymer coating, the textured polymer coating and the optimized textured polymer coating, assuming a constant heat transfer coefficient h=10 W/m^{2}K and a peak solar intensity of 832 W/m^2 at 12 pm; (d) Thermal performance of the flat polymer coating, surface textured polymer coating and the bare concrete, with an infrared-transparent wind-shield LDPE covered to limit the convection.

7.2.3 Water Harvest of White Coatings based on Hollow Glass Microspheres

White coatings based on hollow glass microspheres exhibits high solar reflectivity and infrared emissivity, which enables significant radiative cooling capability. This radiative cooling capability not only reduces surface temperatures for building applications, but also makes water harvest from the ambient air promising since the surface temperature is lower than the ambient temperature. When the surface temperature drops below the dew point temperature, water vapor from the air starts to condense on the surface. The dew point temperature is related to the ambient temperature and relative humidity. High preferential condensation can occur on radiative cooling surfaces since such surfaces usually have a high infrared emissivity especially in the wavelength region of 8-13 μm. This phenomenon was observed already in ancient times and was studied with radiative cooling materials by some other groups recently as well. We also study the water harvest possibility of white coatings based on hollow glass microspheres in different locations by conducting thermodynamic analysis and calculations. The white coating is assumed to be insulated at the back and to experience a net thermal radiation power loss (**P**) so that it cools down below the ambient temperature, $\mathbf{T_{amb}}$. Water condensation happens when the surface temperature ($\mathbf{T_{sur}}$) fall below the dew point temperature ($\mathbf{T_{dew}}$). During the condensation the latent heat (**L**=2.26 MJ/kg) times the condensation rate (**E**), is transferred to the surface per unit time. Heat is also transported to the radiator both from the air by convection and conduction ($\mathbf{Q_{air}}$). In equilibrium the power balance is given by

$$P = LE + Q_{air} \tag{7.1}$$

The power transferred to the surface from the surroundings is given by

$$Q_{air} = h_{air}(T_{amb} - T_{sur}) \tag{7.2}$$

Where **h_{air}** is the heat transfer coefficient. The product LE is proportional to the transport of water vapor which is described by a transfer coefficient **h_v**:

$$LE = \frac{h_v(e_{amb} - e_{sur})}{\xi} \tag{7.3}$$

Where **e_{amb}** is the ambient vapor pressure, **e_{sur}** is the water vapor pressure close to the surface and ξ=66 Pa/K is the so called psychrometer constant. The water vapor transfer coefficient **h_v** is approximately equal to **h_{air}**. When condensation occurs, **e_{amb}** and **e_{sur}** is equal to the saturation pressure at temperature **T_{amb}** and **T_{sur}**. They can be expressed by Tetens equation as

$$P = 0.61078 \exp\left(\frac{17.27T}{T + 237.3}\right) \tag{7.4}$$

The heat transfer coefficient **h_{air}** can be expressed as

$$h_{air} = 2.8 + 3.0U \tag{7.5}$$

Where **U** is the wind speed. The condensation rate **E** and the surface temperature **T_{sur}** are obtained from the requirement that equation (7.1) and (7.3) must be satisfied simultaneously.

If using the ambient conditions in Irvine, we can easily calculate the condensation rate of the white coating assuming a solar reflectivity of 0.92 and an infrared emissivity of 0.9. For example, **Fig. 7.3a** shows the water condensation rate as a function of time on 12/09/19 using the ambient conditions (including ambient air, relative humidity, dew point temperature, wind speed and solar intensity) from a local weather station in Irvine. We also study the ambient requirements when the water condensation would be possible which means the condensation rate **E** is positive. By assuming that, **Fig. 7.3b** shows that the relative humidity needs to be larger than 60% and the condensation would be enhanced when the wind speed is in the range of around 1-10 m/s.

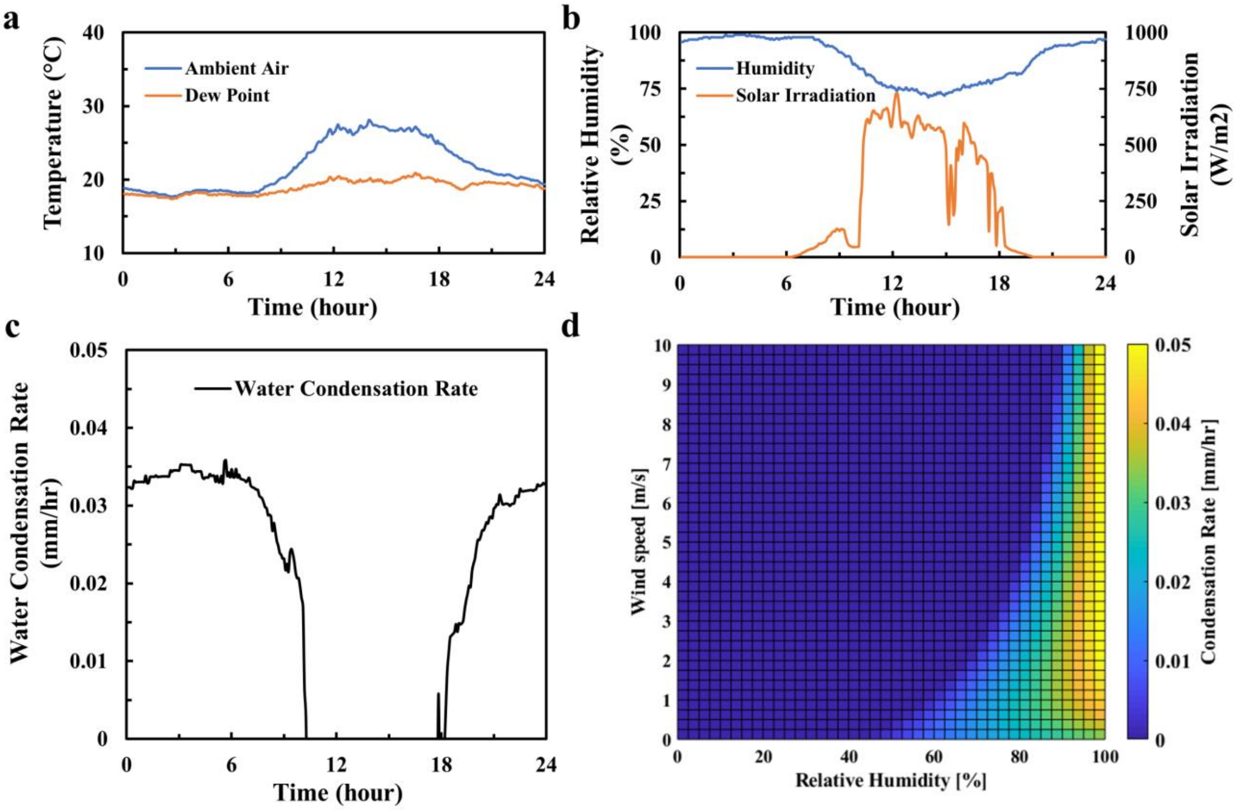

Figure 7.3 Water condensation of white coatings based on hollow glass microspheres. (**a**) The ambient air temperature, the dew point temperature, (**b**) the humidity and the solar irradiation as a function of time on 12/09/19 in Irvine; (**c**) The calculated water condensation rate as a function of time using ambient conditions in Irvine; (**d**) The water condensation rate as functions of relative humidity and wind speed, assuming an ambient temperature of 15°C, an infrared emissivity of 0.85, no solar irradiation and clear sky.

Using the same model, we explore the water condensation per year in different locations in California and across the US. The results are summarized in **Table 7.1** below.

US Climate Zone	Location	TMY3 Weather Station #	Annual Water Condensation (mm)
2A	Mobile, AL	722230	115.9927
	Daytona Beach, FL	722056	112.3888
	Fort Myers, FL	722106	111.5087
	Gainesville, FL	722146	143.7108
	Jacksonville, FL	722060	146.6639
	Orlando, FL	722057	82.3048
	Pensacola, FL	722223	135.2773
	Sarasota, FL	722115	119.1426
	Tallahassee, FL	722140	137.0447
	Tampa, FL	722110	104.5538
	Baton, LA	722317	128.6312
	Lafayette, LA	722405	107.9389
	New Orleans, LA	722315	71.8954
	Biloxi, MS	747686	103.5424
	Jackson, MS	722350	128.5949
	Austin, TX	722540	104.083
	Dallas, TX	722590	52.4865
	Galveston, TX	722420	76.5641
	Houston, TX	722430	103.8632
	San Antonio, TX	722530	82.7933
3B	Los Angeles	722950	115.5496
	San Diego	722900	87.2321
	Chula Vista	722904	141.997
	Long Beach	722970	106.0157
	Santa Ana	722977	140.5249
	Santa Barbara	723925	159.5312

3C	San Francisco	724940	114.9476
	Oakland	724930	145.4491
	San Jose	724945	103.9277
	Paso Robles	723965	103.6515
	Santa Maria	723940	176.0036
	Lompoc	722895	111.3628

Table 7.1 Annual water condensation calculation of white coatings based on hollow glass microspheres in different locations in California and across the United States.

From the table we can see that the water condensation varies a lot among different locations and it is usually high in coastal areas where the relative humidity is generally high throughout the whole year. However, it is very small in hot and dry areas such as Brawley and Barstow.

The possible water condensation of white coating materials opens the possibility of harvesting water from the ambient air using radiative cooling materials, which can be a great source of clean water to address the water crisis nowadays. It is also possible to produce hydrogen from the harvested water if combined with electrolysis instruments properly.

References

1. Richard C. Keller. Europe’s killer heat waves are a new norm. The death rates shouldn’t be. *The Washington Post Online* (2019). Available at: https://www.washingtonpost.com/outlook/2019/07/26/europes-killer-heat-waves-are-new-norm-death-rates-shouldnt-be/. (Accessed: 20th September 2019)

2. Salamanca, F., Georgescu, M., Mahalov, A., Moustaoui, M. & Wang, M. Anthropogenic heating of the urban environment due to air conditioning. *J. Geophys. Res. Atmos.* **119**, 5949–5965 (2014).

3. Family, R. & Mengüç, M. P. Materials for Radiative Cooling: A Review. *Procedia Environ. Sci.* **38**, 752–759 (2017).

4. Santamouris, M. Cooling the buildings – past, present and future. *Energy Build.* **128**, 617–638 (2016).

5. Isaac, M. & van Vuuren, D. P. Modeling global residential sector energy demand for heating and air conditioning in the context of climate change. *Energy Policy* **37**, 507–521 (2009).

6. Crossley, S., Mathur, N. D. & Moya, X. New developments in caloric materials for cooling applications. *AIP Adv.* **5**, (2015).

7. Hossain, M. M. & Gu, M. Radiative cooling: Principles, progress, and potentials. *Adv. Sci.* **3**, 1–10 (2016).

8. Santamouris, M. & Feng, J. Recent Progress in Daytime Radiative Cooling: Is It the Air Conditioner of the Future? *Buildings* **8**, 168 (2018).

9. Lord, S. D. A New Software Tool for Computing Earth’s Atmospheric Transmission of

Near-and Far-Infrared Radiation. *NASA Tech. Memo.* (1992).

10. Harrison, A. W. & Walton, M. R. Radiative cooling of TiO2 white paint. *Sol. Energy* **20**, 185–188 (1978).

11. Orel, B., Gunde, M. K. & Krainer, A. Radiative cooling efficiency of white pigmented paints. *Sol. Energy* **50**, 477–482 (1993).

12. Catalanotti, S. *et al.* The radiative cooling of selective surfaces. *Sol. Energy* **17**, 83–89 (1975).

13. Granqvist, C. G. & Hjortsberg, A. Surfaces for radiative cooling: Silicon monoxide films on aluminum. *Appl. Phys. Lett.* **36**, 139–141 (1980).

14. Granqvist, C. G., Hjortsberg, A. & Eriksson, T. S. Radiative cooling to low temperatures with selectivity IR-emitting surfaces. *Thin Solid Films* **90**, 187–190 (1982).

15. SURFACE COATINGS FOR RADIATIVE COOLING APPLICATIONS: SILICON DIOXIDE AND SILICON NITRIDE MADE BY REACTIVE d-SPUTrERING T.S. ERIKSSON, S.-J. JIANG and C.G. GRANQVIST. *Sol. Energy Mater.* **12**, 319–325 (1985).

16. Raman, A. P., Anoma, M. A., Zhu, L., Rephaeli, E. & Fan, S. Passive radiative cooling below ambient air temperature under direct sunlight. *Nature* **515**, 540–544 (2014).

17. Kou, J. long, Jurado, Z., Chen, Z., Fan, S. & Minnich, A. J. Daytime Radiative Cooling Using Near-Black Infrared Emitters. *ACS Photonics* **4**, 626–630 (2017).

18. Zhai, Y. *et al.* Scalable-manufactured randomized glass-polymer hybrid metamaterial for daytime radiative cooling. *Science.* **355**, 1062–1066 (2017).

19. Li, D. *et al.* Scalable and hierarchically designed polymer film as a selective thermal emitter for high-performance all-day radiative cooling. *Nat. Nanotechnol.* **16**, 153–158 (2020).

20. Rephaeli, E., Raman, A. & Fan, S. Untrabroadband Photonic Structures To Achieve High-Performance Daytime Radiative Cooling. *Nano Lett.* **13**, 1457–1461 (2013).

21. Bao, H. *et al.* Double-layer nanoparticle-based coatings for efficient terrestrial radiative cooling. *Sol. Energy Mater. Sol. Cells* **168**, 78–84 (2017).

22. Mandal, J., Yang, Y., Yu, N. & Raman, A. P. Paints as a Scalable and Effective Radiative Cooling Technology for Buildings. *Joule* **4**, 1350–1356 (2020).

23. Mandal, J. *et al.* Hierarchically porous polymer coatings for highly efficient passive daytime radiative cooling. *Science.* **362**, 315–319 (2018).

24. Li, X., Peoples, J., Yao, P. & Ruan, X. Ultrawhite BaSO4Paints and Films for Remarkable Daytime Subambient Radiative Cooling. *ACS Appl. Mater. Interfaces* **13**, 21733–21739 (2021).

25. Chen, Z., Zhu, L., Raman, A. & Fan, S. Radiative cooling to deep sub-freezing temperatures through a 24-h day–night cycle. *Nat. Commun.* **7**, 13729 (2016).

26. Huang, Z. & Ruan, X. Nanoparticle embedded double-layer coating for daytime radiative cooling. *Int. J. Heat Mass Transf.* **104**, 890–896 (2017).

27. Atiganyanun, S. *et al.* Effective Radiative Cooling by Paint-Format Microsphere-Based Photonic Random Media. *ACS Photonics* **5**, 1181–1187 (2018).

28. Peoples, J. *et al.* A strategy of hierarchical particle sizes in nanoparticle composite for enhancing solar reflection. *Int. J. Heat Mass Transf.* **131**, 487–494 (2019).

29. Nie, X. *et al.* Cool White Polymer Coatings based on Glass Bubbles for Buildings. *Sci. Rep.* **10**, 1–10 (2020).

30. Li, X. *et al.* Full Daytime sub-ambient radiative cooling with high figure of merit in commercial-like paints. *arXiv* (2020). doi:10.2139/ssrn.3652325

31. Felicelli, A. *et al.* Thin layer lightweight and ultrawhite hexagonal boron nitride nanoporous paints for daytime radiative cooling. *Cell Reports Phys. Sci.* **3**, 101058 (2022).

32. Ly, K. C. S. *et al.* A Dual-Mode Infrared Asymmetric Photonic Structure for All-Season Passive Radiative Cooling and Heating. *Adv. Funct. Mater.* **2203789**, 1–11 (2022).

33. Hsu, P. C. *et al.* Radiative human body cooling by nanoporous polyethylene textile. *Science.* **353**, 1019–1023 (2016).

34. Youngquist, R. C., Nurge, M. A., Johnson, W. L., Gibson, T. L. & Surma, J. M. Cryogenic deep space thermal control coating. *J. Spacecr. Rockets* **55**, 622–631 (2018).

35. Li, T. *et al.* A radiative cooling structural material. *Science.* **364**, 760–763 (2019).

36. Li, X. *et al.* Integration of daytime radiative cooling and solar heating for year-round energy saving in buildings. *Nat. Commun.* **11**, 1–9 (2020).

37. Marshall, K. N. & Breuch, R. A. Optical solar reflector: A highly stable, low αs∈spacecraft thermal control surface. *J. Spacecr. Rockets* **5**, 1051–1056 (1968).

38. Barlev, D., Vidu, R. & Stroeve, P. Innovation in concentrated solar power. *Sol. Energy Mater. Sol. Cells* **95**, 2703–2725 (2011).

39. Fernández-García, A. *et al.* Durability of solar reflector materials for secondary concentrators used in CSP systems. *Sol. Energy Mater. Sol. Cells* **130**, 51–63 (2014).

40. Moitra, P. *et al.* Large-Scale All-Dielectric Metamaterial Perfect Reflectors. *ACS Photonics* **2**, 692–698 (2015).

41. Slovick, B., Yu, Z. G., Berding, M. & Krishnamurthy, S. Perfect dielectric-metamaterial reflector. *Phys. Rev. B - Condens. Matter Mater. Phys.* **88**, 1–7 (2013).

42. Moitra, P., Slovick, B. A., Gang Yu, Z., Krishnamurthy, S. & Valentine, J. Experimental demonstration of a broadband all-dielectric metamaterial perfect reflector. *Appl. Phys. Lett.* **104**, 171102 (2014).

43. Xing, Z., Tay, S. W., Ng, Y. H. & Hong, L. Porous SiO2 Hollow Spheres as a Solar Reflective Pigment for Coatings. *ACS Appl. Mater. Interfaces* **9**, 15103–15113 (2017).

44. Xing, Z., Tay, S. W., Ng, Y. H. & Hong, L. Porous SiO2 Hollow Spheres as a Solar Reflective Pigment for Coatings. *ACS Appl. Mater. Interfaces* **9**, 15103–15113 (2017).

45. Alden, J. D. *et al.* Radiative cooling by silicone-based coating with randomly distributed microbubble inclusions. *J. Photonics Energy* **9**, 1 (2019).

46. Yu, Z., Nie, X., Yuksel, A. & Lee, J. Reflectivity of solid and hollow microsphere composites and the effects of uniform and varying diameters. *J. Appl. Phys.* **128**, 053103 (2020).

47. Jacucci, G., Bertolotti, J. & Vignolini, S. Role of Anisotropy and Refractive Index in Scattering and Whiteness Optimization. *Adv. Opt. Mater.* **7**, 1900980 (2019).

48. Yuksel, A., Yu, E. T., Cullinan, M. & Murthy, J. Effect of particle size distribution on near-field thermal energy transfer within the nanoparticle packings. *J. Photonics Energy* **9**, 1 (2019).

49. Tervo, E., Francoeur, M., Cola, B. & Zhang, Z. Thermal radiation in systems of many dipoles. *Phys. Rev. B* **100**, 1–11 (2019).

50. Li, T. *et al.* A radiative cooling structural material. *Science* **364**, 760–763 (2019).

51. Hsu, P. *et al.* A dual-mode textile for human body radiative heating and Cooling. *Sci. Adv.* **3**, e1700895 (2017).

52. Shang, G. *et al.* Highly selective photonic glass filter for saturated blue structural color. *APL Photonics* (2019). doi:10.1063/1.5084138

53. Palik, E. D. *Handbook of optical constants of solids*. *Academic Press* (1998). doi:10.1016/C2009-0-20920-2

54. Querry, M. *Optical Constants of Minerals and Other Materials from the Millimeter to the Ultraviolet*. *Chemical Research, Development & Engineering Center, US Army Armament Munitions Chemical Command* (1987).

55. Vera, M. U. & Durian, D. J. Angular distribution of diffusely transmitted light. *Phys. Rev. E - Stat. Physics, Plasmas, Fluids, Relat. Interdiscip. Top.* **53**, 3215–3224 (1996).

56. Hutchinson, N. J., Coquil, T., Navid, A. & Pilon, L. Effective optical properties of highly ordered mesoporous thin films. *Thin Solid Films* **518**, 2141–2146 (2010).

57. Garnett, J. C. M. & Larmor, J. Colours in metal glasses and in metallic films. *Proc. R. Soc. London* **203**, 385–420 (1904).

58. Judd, D. B. Fresnel reflection of diffusely incident light. *J. Res. Natl. Bur. Stand. (1934).* **29**, 329 (1942).

59. Del Río, J. A. & Whitaker, S. Maxwell's equations in two-phase systems I: Local

electrodynamic equilibrium. *Transp. Porous Media* **39**, 159–186 (2000).

60. Del Río, J. A. & Whitaker, S. Maxwell's equations in two-phase systems II: Two-equation model. *Transp. Porous Media* **39**, 259–287 (2000).

61. Bohren, C. F. *Absorption and scattering of light by small particles*. *John Wiley \& Sons* (1983). doi:10.1088/0031-9112/35/3/025

62. Demontis, V., Marini, A., Floris, F., Sorba, L. & Rossella, F. Engineering the optical reflectance of randomly arranged self-assembled semiconductor nanowires. *AIP Conf. Proc.* **2257**, 020009 (2020).

63. Schertel, L. *et al.* Tunable high-index photonic glasses. *Phys. Rev. Mater.* **3**, 015203 (2019).

64. Schertel, L. *et al.* The Structural Colors of Photonic Glasses. *Adv. Opt. Mater.* **7**, 1900442 (2019).

65. Tanev, S. *et al.* Advances in the FDTD design and modeling of nano- and bio-photonics applications. *Photonics Nanostructures - Fundam. Appl.* **9**, 315–327 (2011).

66. Tanev, S., Tuchin, V. V. & Paddon, P. Light scattering effects of gold nanoparticles in cells: FDTD modeling. *Laser Phys. Lett.* **3**, 594 (2006).

67. Rodríguez-de Marcos, L. V., Larruquert, J. I., Méndez, J. A. & Aznárez, J. A. Self-consistent optical constants of MgF_2, LaF_3, and CeF_3 films. *Opt. Mater. Express* **7**, 989 (2017).

68. Marcos, L. R. De *et al.* Optical constants of SrF2 thin films in the 25-780-eV spectral range. *J. Appl. Phys.* **113**, 143501 (2013).

69. Nigara, Y. Measurement of the Optical Constants of Yttrium Oxide. *Jpn. J. Appl. Phys.* **7**,

404–408 (1968).

70. Siefke, T. *et al.* Materials Pushing the Application Limits of Wire Grid Polarizers further into the Deep Ultraviolet Spectral Range. *Adv. Opt. Mater.* **4**, 1780–1786 (2016).

71. Kaplan, P. D., Dinsmore, A. D., Yodh, A. G. & Pine, D. J. Diffuse-transmission spectroscopy: A structural probe of opaque colloidal mixtures. *Phys. Rev. E* **50**, 4827 (1994).

72. De Boer, F. Y., Van Dijk-Moes, R. J. A., Imhof, A. & Velikov, K. P. Characterization of the Scattering and Absorption of Colored Zein Colloids in Optically Dense Dispersions. *Langmuir* **35**, 12091–12099 (2019).

73. Rydin, Y. *et al.* Shaping Cities for Health: the complexities of planning urban environments in the 21st century. *Lancet* **379**, 2079–2108 (2012).

74. Landrigan, P. J. *et al.* The Lancet Commission on pollution and health. *Lancet* **391**, 462–512 (2018).

75. Sobstyl, J. M., Emig, T., Qomi, M. J. A., Ulm, F. J. & Pellenq, R. J. M. Role of City Texture in Urban Heat Islands at Nighttime. *Phys. Rev. Lett.* **120**, 108701 (2018).

76. Krishna, A. & Lee, J. Morphology-Driven Emissivity of Microscale Tree-like Structures for Radiative Thermal Management. *Nanoscale Microscale Thermophys. Eng.* **22**, 124–136 (2018).

77. Gueymard, C. A., Myers, D. & Emery, K. Proposed Reference Irradiance Spectra for Solar Energy Systems Testing. *Sol. Ene* **73**, 443–467 (2003).

78. Synnefa, A., Santamouris, M. & Livada, I. A study of the thermal performance of reflective

coatings for the urban environment. *Sol. Energy* **80**, 968–981 (2006).

79. Zhao, D. *et al.* Subambient Cooling of Water: Toward Real-World Applications of Daytime Radiative Cooling. *Joule* **3**, 111–123 (2018).

80. Alden, J. D. *et al.* Radiative cooling by silicone-based coating with randomly distributed microbubble inclusions. *J. Photonics Energy* **9**, 1 (2019).

81. Zhang, X. A. *et al.* Dynamic gating of infrared radiation in a textile. *Science (80-.).* **623**, 1–15 (2019).

82. Howell, J. R., Mengüç, M. P. & Siegel, R. *Thermal radiation heat transfer, sixth edition*. *Thermal Radiation Heat Transfer, Sixth Edition* (2015).

83. Migahed, M. D. & Zidan, H. M. Influence of UV-irradiation on the structure and optical properties of polycarbonate films. *Curr. Appl. Phys.* **6**, 91–96 (2006).

84. Mahendia, S., Tomar, A. K., Goyal, P. K. & Kumar, S. Tuning of refractive index of poly(vinyl alcohol): Effect of embedding Cu and Ag nanoparticles. *J. Appl. Phys.* **131**, 073103 (2013).

85. Lalanne, P. & Jurek, M. P. Computation of the near-field pattern with the coupled-wave method for transverse magnetic polarization. *J. Mod. Opt.* (1998). doi:10.1080/09500349808230634

86. Typical Meteorological Year 3 Weather Data. Available at: http://climate.onebuilding.org/sources/default.html. (Accessed: 25th April 2021)

87. Team, E. W. ESRL Global Monitoring Division-Global Radiation Group. (2005).

88. Lee, T., Henyey, T. L. & Damiata, B. N. A simple method for the absolute measurement of

thermal conductivity of drill cuttings. *Geophysics* **51**, 1580–1584 (2002).

89. Deru, M. *et al.* U.S. Department of Energy Commercial Reference Building Models of the National Building Stock. (2011). doi:10.2172/1009264

90. Energy standard for buildings except low-rise residential buildings. *ASHRAE Standard* (2004).

91. Wilcox, S. & Marion, W. *Users manual for TMY3 data sets*. (National Renewable Energy Laboratory Golden, CO, 2008).

92. Jones, M. . Effects of UV Radiation on Building Materials. in *Building Research Association of New Zealand (BRANZ)* (2002).

93. Tsuda, S., Yamaguchi, S., Kanamori, Y. & Yugami, H. Spectral and angular shaping of infrared radiation in a polymer resonator with molecular vibrational modes. *Opt. Express* **26**, 6899–6915 (2018).

94. Chen, J. & Lu, L. Development of radiative cooling and its integration with buildings: A comprehensive review. *Sol. Energy* **212**, 125–151 (2020).

95. Li, W., Li, Y. & Shah, K. W. A materials perspective on radiative cooling structures for buildings. *Sol. Energy* **207**, 247–269 (2020).

96. Zhao, B., Hu, M., Ao, X., Chen, N. & Pei, G. Radiative cooling: A review of fundamentals, materials, applications, and prospects. *Appl. Energy* **236**, 489–513 (2019).

97. Zhou, K., Miljkovic, N. & Cai, L. Performance analysis on system-level integration and operation of daytime radiative cooling technology for air-conditioning in buildings. *Energy Build.* **235**, 110749 (2021).

98. Zhao, D., Aili, A., Yin, X., Tan, G. & Yang, R. Roof-integrated radiative air-cooling system to achieve cooler attic for building energy saving. *Energy Build.* **203**, 109453 (2019).

99. Yoon, S. *et al.* Performance analysis of a hybrid HVAC system consisting of a solar thermal collector and a radiative cooling panel. *Energy Build.* **241**, 110921 (2021).

100. Li, X., Xie, W., Sui, C. & Hsu, P. C. Multispectral Thermal Management Designs for Net-Zero Energy Buildings. *ACS Mater. Lett.* **2**, 1624–1643 (2020).

101. Levinson, R., Akbari, H., Konopacki, S. & Bretz, S. Inclusion of cool roofs in nonresidential Title 24 prescriptive requirements. *Energy Policy* **33**, 151–170 (2005).

102. Lu, X., Xu, P., Wang, H., Yang, T. & Hou, J. Cooling potential and applications prospects of passive radiative cooling in buildings: The current state-of-the-art. *Renew. Sustain. Energy Rev.* **65**, 1079–1097 (2016).

103. Akbari, H., Levinson, R. & Rainer, L. Monitoring the energy-use effects of cool roofs on California commercial buildings. *Energy Build.* **37**, 1007–1016 (2005).

104. Parker, D. S. *et al.* Measured and simulated performance of reflective roofing systems in residential buildings. *ASHRAE Trans.* **104**, 963–975 (1998).

105. Akbari, H., Bretz, S., Kurn, D. M. & Hanford, J. Peak power and cooling energy savings of high-albedo roofs. *Energy Build.* **25**, 117–126 (1997).

106. Cool Roof Rating Council. Find rated products - Cool Roof Rating Council.

107. Kolokotsa, D., Diakaki, C., Papantoniou, S. & Vlissidis, A. Numerical and experimental analysis of cool roofs application on a laboratory building in Iraklion, Crete, Greece. *Energy Build.* **55**, 85–93 (2012).

108. Romeo, C. & Zinzi, M. Impact of a cool roof application on the energy and comfort performance in an existing non-residential building. A Sicilian case study. *Energy Build.* **67**, 647–657 (2013).

109. Synnefa, A., Saliari, M. & Santamouris, M. Experimental and numerical assessment of the impact of increased roof reflectance on a school building in Athens. *Energy Build.* **55**, 7–15 (2012).

110. Touchaei, A. G., Hosseini, M. & Akbari, H. Energy savings potentials of commercial buildings by urban heat island reduction strategies in Montreal (Canada). *Energy Build.* **110**, 41–48 (2016).

111. Gao, Y. *et al.* Cool roofs in China: Policy review, building simulations, and proof-of-concept experiments. *Energy Policy* **74**, 190–214 (2014).

112. Kolokotroni, M., Gowreesunker, B. L. & Giridharan, R. Cool roof technology in London: An experimental and modelling study. *Energy Build.* **67**, 658–667 (2013).

113. Hanif, M., Mahlia, T. M. I., Zare, A., Saksahdan, T. J. & Metselaar, H. S. C. Potential energy savings by radiative cooling system for a building in tropical climate. *Renew. Sustain. Energy Rev.* **32**, 642–650 (2014).

114. Berardi, U., Garai, M. & Morselli, T. Preparation and assessment of the potential energy savings of thermochromic and cool coatings considering inter-building effects. *Sol. Energy* **209**, 493–504 (2020).

115. Dabaieh, M., Wanas, O., Hegazy, M. A. & Johansson, E. Reducing cooling demands in a hot dry climate: A simulation study for non-insulated passive cool roof thermal performance

in residential buildings. *Energy Build.* **89**, 142–152 (2015).

116. Yazdani, H. & Baneshi, M. Building energy comparison for dynamic cool roofs and green roofs under various climates. *Sol. Energy* **230**, 764–778 (2021).

117. Chi, F., Liu, Y. & Yan, J. Integration of Radiative-based air temperature regulating system into residential building for energy saving. *Appl. Energy* **301**, 117426 (2021).

118. Chen, J. & Lu, L. Comprehensive evaluation of thermal and energy performance of radiative roof cooling in buildings. *J. Build. Eng.* **33**, 101631 (2021).

119. Crawley, D. B. *et al.* EnergyPlus: Creating a new-generation building energy simulation program. *Energy Build.* **33**, 319–331 (2001).

120. Brown, M. A., Soni, A., Lapsa, M. V, Southworth, K. & Cox, M. High energy burden and low-income energy affordability: conclusions from a literature review. *Prog. Energy* **2**, 042003 (2020).

121. Chen, C. fei, Feng, J., Luke, N., Kuo, C. P. & Fu, J. S. Localized energy burden, concentrated disadvantage, and the feminization of energy poverty. *iScience* **25**, 104139 (2022).

122. Sun, K. *et al.* Passive cooling designs to improve heat resilience of homes in underserved and vulnerable communities. *Energy Build.* **252**, 111383 (2021).

123. Mechri, H. E., Capozzoli, A. & Corrado, V. USE of the ANOVA approach for sensitive building energy design. *Appl. Energy* **87**, 3073–3083 (2010).

124. Olofsson, T., Andersson, S. & Sjögren, J. U. Building energy parameter investigations based on multivariate analysis. *Energy Build.* **41**, 71–80 (2009).

125. Kusiak, A., Li, M. & Tang, F. Modeling and optimization of HVAC energy consumption. *Appl. Energy* **87**, 3092–3102 (2010).

126. Elbreki, A. M. *et al.* Experimental and economic analysis of passive cooling PV module using fins and planar reflector. *Case Stud. Therm. Eng.* **23**, 100801 (2021).

127. New, J., Miller, W. A., Huang, Y. & Levinson, R. Comparison of software models for energy savings from cool roofs. *Energy Build.* **114**, 130–135 (2016).

128. Wei, M. *et al.* Approaches to cost-effective near-net zero energy new homes with time-of-use value of energy and battery storage. *Adv. Appl. Energy* **2**, 100018 (2021).

129. Company, P. G. and E. Guide to California Climate Zones. (2006). Available at: https://www.pge.com/myhome/edusafety/workshopstraining/pec/toolbox/arch/climate/index.shtml. (Accessed: 27th May 2022)

130. Average Natural Gas Price in US. Available at: https://www.eia.gov/energyexplained/natural-gas/prices.php. (Accessed: 26th May 2022)

131. Average Retail Price for Electricity. Available at: https://www.eia.gov/electricity/state/. (Accessed: 26th May 2022)

132. Huetteman, Justine, Travis Johnson, and J. S. Using eGRID for Environmental Footprinting of Electricity Purchases. *U.S. Environmental Protection Agency* (2020). Available at: https://www.epa.gov/egrid/egrid-technical-documents. (Accessed: 27th May 2022)

133. Agency, U. S. E. P. Greenhouse Gases Equivalencies Calculator - Calculations and References. (2021). Available at: https://www.epa.gov/energy/greenhouse-gases-equivalencies-calculator-calculations-and-references. (Accessed: 27th May 2022)

134. Shaw, R. G. & Mitchell-Olds, T. ANOVA for unbalanced data: an overview. *Ecology* **74**, 1638–1645 (1993).

135. Stat-Ease, I. Stat-Ease » v12 » Design-Expert.